Institut
für
Mechanik

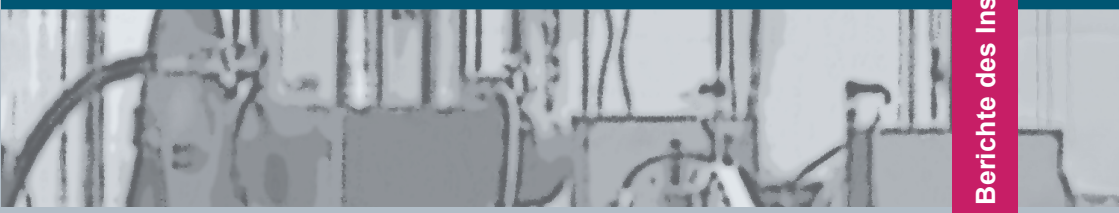

Berichte des Instituts für Mechanik (Bericht 3/2021)

Zhibin Wang

Fracture mechanics analysis and simulations in piezoelectric quasicrystals and electromechanical crack growth experiments

kassel university press

Berichte des Instituts für Mechanik

Bericht 3/2021

Zhibin Wang

Fracture mechanics analysis and simulations in piezoelectric quasicrystals and electromechanical crack growth experiments

kassel
university
press

This work has been accepted by Faculty of Mechanical Engineering of the University of Kassel as a thesis for acquiring the academic degree of Doktor der Ingenieurwissenschaften (Dr.-Ing.).

Supervisor: Prof. Dr.-Ing. habil. Andreas Ricoeur
Co-Supervisor: Prof. Dr.-Ing. habil. Chuanzeng Zhang

Defense day: 18. August 2021

https://orcid.org/0000-0001-7662-6032 (Zhibin Wang)

Bibliographic information published by Deutsche Nationalbibliothek
The Deutsche Nationalbibliothek lists this publication in the Deutsche Nationalbibliografie; detailed bibliographic data is available in the Internet at http://dnb.dnb.de.

Zugl.: Kassel, Univ., Diss. 2021
ISBN 978-3-7376-0989-0
https://doi.org/doi:10.17170/kobra-202109294824

Printing Shop: Print Management Logistik Service, Kassel
Printed in Germany

Acknowledgment

First of all, I want to thank Prof. Dr.-Ing. Andreas Ricoeur for gaving me the chance to work in his research group. Over the past years, he has always guided me in my research, paper writing, presentations, and other aspects, provided me the time for academic discussions and gave me many useful tips that I will benefit in my future life.

My thanks also go to Prof. Dr.-Ing. Chuanzeng Zhang for reviewing my dissertation and Prof. Dr.-Ing. Thomas Niendorf, Prof. Dr. Felix Lindner and Prof. Dr.-Ing. Hartmut Hetzler for taking the positions in the doctoral committee.

Many people helped me during the work. I wish to express my appreciation to Prof. Faxin Li from Peking University, who helped me to order ferroelectric specimens; my colleagues, Dr.-Ing. Matthias Oxe, Dipl.-Ing. Dirk Hagedorn and M.Sc. Philip Uckermann, who made vital contributions to the design and execution of the fracture experiments, helped me to solve the problems far beyond what I could have imagined before starting the experiment; M.Sc. Johannes Scheel, M.Sc. Alexander Schlosser and Dipl.-Ing. Marius Wingen, who revised my manuscript and gave me numerous valuable suggestions.

I would also like to thank all members of the Institute of Mechanics in the University of Kassel. I really enjoy the work and life here in- and outside of the institute with them, especially the unforgettable events, such like the academic trips with "Grand Final", the extreme sport on the Fulda, the hiking day...

Last but not least, I would like to thank my family for their devoted support. My daughter, Linge 琳格, also did her part by lying in my arm and quietly watching me to revise my thesis, which calmed me down and gave me enormous satisfaction in the final phase of doctorate.

Kassel, August 2021 Zhibin Wang

王志斌

Kurzfassung

Piezoelektrische Werkstoffe, eine wichtige Klasse kristalliner Materialien, sind grundlegender Bestandenteil von intelligenten Systemen mit gekoppelten elektrischen und mechanischen Feldern. Quasikristalle stellen im Gegensatz zu den Piezoelektrika eine neue Materialklasse dar, die in gewisser Weise die Lücke zwischen kristallinen und amorphen Materialien schließt und im Rahmen der Kontinuumsmechanik durch zwei Typen von Feldern, Phonon- und Phasonfelder, beschrieben werden kann. Mittlerweile ist bekannt, dass Quasikristalle auch piezoelektrische Eigenschaften haben können und somit drei gekoppelte Feldtypen in diesen Materialien vorhanden sind. Aus technischer Sicht sind Quasikristalle und Piezoelektrika aufgrund ihrer vorteilhaften Eigenschaften interessant, was vielfältiges Anwendungspotential ermöglicht und Anlass zu intensiver Forschung gibt. Der Fokus dieser Arbeit liegt auf dem Einfluss von Kopplungseffekten der verschiedenen Felder und der elektrischen Belastung auf das bruchmechanische Verhalten. Im Zentrum der Betrachtung stehen Risspfade, anhand derer die Plausibilität von materialspezifischen Modellen, Simulationsverfahren und bruchmechanische Kriterien bewertet werden. Zu diesem Zweck werden theoretische Grundlagen im Sinne der Kontinuumsmechanik umfassend entwickelt, die Phonon-, Phason- und elektrische Felder in piezoelektrischen Quasikristallen einschließen. Die bruchmechanischen Beanspruchungsgrößen werden für die Materialien verallgemeinert und auf der Grundlage analytischer Lösungen in numerischen Methoden umgesetzt. Zur Simulation des Risswachstums mit einem Neuvernetzungalgorithmus, der auf einer adaptiven Vernetzungsstrategie in Verbindung mit Finite-Elemente-Software beruht, werden die klassischen und neu vorgeschlagenen Rissablenkungskriterien implementiert. Anhand der Simulationsergebnisse werden Einflüsse der Kopplungskoeffizienten und der Konfiguration der Proben sowie der elektrischen Belastung auf die Risspfade untersucht. Darüber hinaus werden Drei-Punkt-Biegeversuche an ferroelektrischen Proben unter verschiedenen Belastungskombinationen durchgeführt. Die experimentellen Ergebnisse und Aufnahmen des Risswachstumsprozesses mit einer Hochgeschwindigkeitskamera enthüllen bemerkenswerte Details.

Abstract

Piezoelectric materials, as an important class of crystalline materials, are fundamental components of smart systems with coupled electric and mechanical fields. Quasicrystals, in contrast to the piezoelectrics, represent a relatively new class of materials which, in a sense, fills the gap between crystalline and amorphous materials and can be described in the framework of continuum mechanics by two types of fields, phonon and phason fields. Meanwhile, it is already known that quasicrystals can also have piezoelectric properties and consequently three coupled field types are present in these materials. From the technical point of view, quasicrystals and piezoelectrics are interesting due to advantageous properties, which allow diverse potential applications and give rise to intensive research. The focus of this thesis is on the influence of coupling effects of the different fields and the electrical loading on the fracture mechanical behavior. The major objective is crack paths, based on which the plausibility of material-specific models, simulation methods and crack deflection criteria are evaluated. For this purpose, a comprehensive framework in terms of continuum mechanics is developed, including phonon, phason, and electric fields in piezoelectric QCs. The fracture mechanics quantities are generalized for the materials and based on the closed-form solutions they are implemented into numerical methods. To simulate the crack growth by using a re-meshing algorithm, which relies on an adaptive meshing strategy in conjunction with finite element software, the classical and new proposed crack deflection criteria are implemented. The influence of the coupling coefficients and the configuration of specimens as well as the electrical loading on crack paths is investigated based on the simulation results. In addition, three-point bending tests are performed on ferroelectric specimens under different loading combinations. The experimental results and the recording of the crack growth process with a high-speed camera show remarkable details.

Contents

Nomenclature

Roman alphabet

A_{IJ}, B_{IJ}	characteristic matrices of the solution in Stroh formalism
$\underline{B}$	differentiated shape functions
B	thickness, normally assumed unit thickness $B = 1$
C_{ijkl}	elastic moduli [Pa]
D_i	electric displacement $[\mathrm{C/m^2}]$
e_{ijk}	piezoelectric coefficients $[\mathrm{C/m^2}]$
$\vec{e}_i$	basis vectors
E_i	electric field $[\mathrm{V/m}]$
E_c	coercive field $[\mathrm{V/m}]$
E^{tot}	total energy of a system
F_k	configurational force
G	energy release rate $[\mathrm{N/m}]$
G_C	crack growth resistance $[\mathrm{N/m}]$
G_j	vector in reciprocal lattice
h^α	shape functions
h_i	phason traction
H	the second energy term analogous to G $[\mathrm{N/m}]$
H_{ij}	phason stresses
J_k	path independent J-integral
K_I, K_{II}, K_{III}	stress intensity factors $[\mathrm{MPa}\sqrt{\mathrm{m}}]$
K_{ijkl}	phason stiffness tensor
K_{IC}	fracture toughness $[\mathrm{MPa}\sqrt{\mathrm{m}}]$
K_{IC}^{app}	fracture toughness based on remote loading $[\mathrm{MPa}\sqrt{\mathrm{m}}]$
K_{IC}^{tip}	effective fracture toughness at crack tip $[\mathrm{MPa}\sqrt{\mathrm{m}}]$
K_{IV}	electric displacement intensity factor $[\mathrm{Cm^{-3/2}}]$
$\underline{K}_S$	generalized stiffness matrix
n_j	unit normal of the integration contour
$\underline{N}$	shape function matrices

p^{α}	eigenvalues of the solution in Stroh formalism
Q	electric charge [C]
r	radius of the polar coordinates
	distance to crack tip
r_i	position of an atom in crystalline structure
R_{ijkl}	phonon-phason coupling tensor
s	specific entropy [J/m^3]
S_{ij}	characteristic matrix for calculation of H
T_c	Curie temperature [K]
u_i	displacement [m]
u	specific internal energy [J/m^3]
U^a	potential energy of external forces [J]
U^i	elastic stain energy [J]
U^f	fracture surface energy [J]
U^{tot}	total potential energy [J]
V	volume, integration area
w	specific work done by external loads [J/m^3]
w_{ij}	phason strain
W	electric/mechanical work [J]
W^a	work associated to external forces [J]
W_i	phason displacement
Y_{ij}	Irwin matrix
z_k	unit vector of irreversible displacement of a defect

Greek letters

Γ	contour of an integration area
$\delta(..)$	variation symbol
δ_t	crack tip opening displacement
Δa	increment of crack advance
Δu_i	crack opening displacement
$\Delta\varphi$	electric potential jump across the crack surfaces
ε_{ij}	strain tensor
κ_0	permittivity of vacuum $(8.854 \times 10^{-12}\mathrm{C/Vm})$
κ_{ij}	dielectric constant tensor [C/Vm]
κ_r	relative electric permittivity

ω	density of electric charges [C/m^3]
ω_i	weighting factor
Ω_{ij}	transformation matrix
φ	electric potential [V]
	angle between global and local coordinate systems
ϕ_I	generalized stress function vector
ϕ_{G_j}	phase angle of $\rho(G_j)$
Φ	elastic free energy density of QCs [J/m^3]
Π	(generalized) electric enthalpy density [J/m^3]
ψ	arbitrary quantity
$\rho(r_i)$	mass density function
$\rho(G_j)$	structure factors of a reciprocal lattice
ρ_{G_j}	magnitude of $\rho(G_j)$
σ_{ij}	stress tensor [Pa]
$\sigma_{\theta\theta}$	hoop stress [Pa]
σ^Y	yield stress [Pa]
θ	angle of the polar coordinates
$\bar{\theta}$	crack deflection angle

Acronyms

1D/2D/3D QCs	one-/two-/three-phason-dimensional quasicrystals
BT	barium titanate
CT	compact tension
CTEM	crack tip element method
CTOD	crack tip opening displacement
DCB	double cantilever beam
ERR	energy release rate
FE	finite element
MCCI	modified crack closure integral
PLZT	lead lanthanum zirconate titanate
PZT	lead zirconate titanate
QA	quasiperiodic axis
QC	quasicrystal
R-curve	crack growth resistance curve
SIF	stress intensity factor

Indices

$(..)_C$	critical value
$(..)^e$	electrical part of variable
$(..)^m$	mechanical part of variable
$(..)^s$	material constants in plane stress condition
$(..)_{diss}$	dissipative part
$(..)_{rev}$	reversible part

Special symbols

$\mathfrak{R}$	real part of complex quantity in brackets
$\mathfrak{I}$	imaginary part of complex quantity in brackets
Å	Ångström, 10^{-10}m

1. Introduction

Smart materials, also known as intelligent materials, have drawn the interest of many researchers in scientific and industrial communities. Analogous to biological materials, they are able to adapt their behavior or functionality to the variation of external stimuli. One of the most well-known responses of external stimuli in smart materials is deformation, which leads to applications as actuators (in response to an electric field) and shape memory materials (in response to a magnetic field or a temperature change), where the movement of parts is caused by intrinsic physical properties rather than complex mechanisms. The study and research of smart materials is thus highly multidisciplinary, including e.g., electronics, magnetics, chemistry, etc. Multi-field problems shall be considered in these situations.

Ferroelectric materials, as one class of the most important smart materials, were discovered in single crystal materials in the early 1920s and intensively studied after that. They belong to the wider class of piezoelectrics, which have been discovered already in the 1880s for single crystals. Nowadays, ferroelectrics are widely used in our daily lives and in many advanced industrial products. Ferroelectrics often exhibit coupled electro-mechanical behavior and in some cases, even thermal and magnetic properties, which are prevalent in applications, e.g., diesel fuel-injection actuators, ultrasonic sensors, RAM/memories, energy harvesters and structural health monitoring. In single crystalline form, ferroelectrics as ultrasonic transducers offer high quality medical imaging and diagnosis. Piezoelectric actuators, often in a stacked structure of functional layers, produce a stroke length about 0.1–0.2% of the actuator length with high position accuracy and very large force compared to the actuator's size, whereas operating voltages are in the order of 10^2–10^3 V. Due to the electrical/mechanical transition as own material property and relatively simple structures without moving parts, piezoelectric actuators have the capability to operate in more complex environments without concern about friction and wear. To date, the most widely used ferroelectrics are lead zirconate titanate (PZT) due to their high Curie temperature and large piezoelectric activity among all ferroelectrics. However, lead is harmful to the environment and toxic to humans, which made the research on alternative lead-free ferroelectrics, e.g., barium titanate (BT) and $(K_xNa_{1-x})NbO_3$ (KNN) recently becoming more popular.

Another class of materials, quasicrystals (abbreviated as QC), is a relatively new type of material with structures between the conventional crystalline and amorphous solids, which was discovered four decades ago. Neither like crystals, which have a rigorous periodic atomic arrangement and a symmetric point group, nor like amorphous solids such as glass, where the atoms are totally disordered, QCs show long-range orientational order but no translational symmetry in particular directions, having the atomic structure being quasiperiodic rather than periodic. Thus, materials with such structures

are called “quasiperiodic crystals” or “quasicrystals”. In QCs, the atomic structure can be altered, where the quasiperiodic arrangement is influenced going along with atomic flips, denoted as phason displacements. With the classical displacements denoted as phonon displacements, QCs present an intrinsic coupled phonon-phason effect. Based on the deduction from crystallographic analysis, most of quasicrystalline phases belong to the class of piezoelectrics, leading to a multi-field coupling problem. The piezoelectric effect in QCs, despite not having been reported in experiment, can be determined by the quasicrystalline structure and is expected in a quasicrystalline barium titanate according to recent research.

Since the discovery of the first QC, many quasicrystalline structures have been observed in metallic alloys and also in meteorite as a natural composition. On the other hand, more and more QCs of various compounds have been successfully prepared in the laboratory, many of which are stable at room temperature. Recently, quasicrystalline structures have also been found in polymers and colloids, which are not as brittle as metallic alloys and are thus called soft matter quasicrystals. While still subject to very limited research in the physicist’s and chemist’s communities, many promising applications are considered or have already been introduced, taking advantage of the beneficial properties of QCs, e.g., low friction coefficient, high hardness, wear and corrosion resistance, low surface energy density and low thermal conductivity. Due to these outstanding properties and the fact that larger specimens or structures are still not available, QCs are often used as fine particles in reinforced materials, as coating material for non-stick pans and surgical instruments, or as hydrogen storage materials. In this context, QCs can also be used for additive manufacturing, providing an appropriated strength to the products.

Reliability and durability are two important requirements for all applications of novel materials. They are particularly critical in applications where a long life is required or where the component is difficult to replace once damage or failure is sustained. Ferroelectrics and QCs, as ceramics and metallic alloys in the most cases, are predominantly brittle at room temperature, where failure may start from damage or micro cracks and transit to unstable crack propagation or fatigue crack growth. In the case of ferroelectrics, depending on their specific usage the units are usually exposed to mechanical loading in combination with e.g., cyclic electric loading or other mixed loading conditions, making lifetime and structural reliability more difficult to assess. The fracture behavior of ferroelectrics thus cannot be described within the framework of fracture theory of conventional non-functional materials. Rather, it must be generalized, taking into account many factors, e.g., the elastic and inelastic strain induced by electric field, the electric permittivity of the crack or the local state of polarization. Due to the manufacturing constraints, the majority of QCs are in the form of fine particles and some large samples can reach a size of up to a few centimeters. As a result, monolithic QCs are scarcely available for mechanical tests, however, pores and cracks can be found in bulk QC alloys. Similar to ferroelectrics, QCs have a coupled effect between the phonon and phason fields, indicating the classical mechanical field and the quasiperiodic order, respectively. Although no phason type of load can be applied, the coupling effect influences the conventional stress and displacement. QCs thus exhibit different fracture behavior from classical materials, which should be investigated.

The focus of this work is on macroscopic cracks, in particular crack deflection and crack paths in coupled materials with phonon, phason and electric fields, in which the coupling effect and additional electric loading affect crack paths. The generalized linear elastic framework with piezoelectric and quasicrystalline properties is described in Chapter 2. In Chapter 3 various fracture parameters and deflection criteria are derived and modified for the application in piezoelectrics and QCs. Fracture boundary value problems are solved in a finite element framework, providing outputs for computing the fracture parameters in post processing. The crack propagation process is efficiently simulated by applying a smart adaptive re-meshing algorithm, see Chapter 4. Simulation results for different specimens are given in Chapter 5, where QCs, piezoelectrics and piezoelectric QCs are considered separately. For QCs, several computed crack deflections with different phonon-phason coupling constants and loading regimes are presented and crack deflection criteria are discussed. For piezoelectrics, the classical deflection criteria are proved to be invalid and therefore a modified criterion is introduced based on the pure mechanical energy release rate. A series of three-point bending tests on ferroelectric specimens is carried out in Chapter 6 and provides statistically evaluated results, investigating the influence of both positive and negative electric fields on crack deflection. One of the experiments without electric loading was recorded with a high-speed camera, providing remarkable details of the onset and propagation of the crack.

2. Theoretical framework

2.1. Some basics of continuum mechanics of elasticity

2.1.1. Index notation

The index notation is used throughout this work for the sake of a succinct formulation of equations [9]. The indices, as lower case alphabetic subscripts, take all values of a variable indicated, e.g., the force vector F_i represents the three components F_1, F_2 and F_3. The number of the non-repeated indices indicates the order of the tensor, e.g., the electric potential requires no index, classified as a scalar, the Cauchy stress is a second-order tensor and thus has two indices. Despite a coordinate system not being intrinsic to a mechanical problem, the Cartesian coordinate system is set as default choice, where the index runs from one to two for a planar problem or three for a spatial problem. A repeated index in equations implies the summation over the range of the index.

In the case of multi-field problems, indices in terms of multi-fields are presented by upper case letters, indicating omnibus variables, e.g., the field intensity factors in piezoelectrics reads

$$K_P = (K_{II}, K_I, K_{III}, K_{IV}), \tag{2.1}$$

where the first three entities are the stress intensity factors of a crack in a three-dimensional problem and $P = 4$ denotes the electric displacement intensity factor [114].

In some context, a second-order tensor ψ_{ij} is written in the vector form ψ_p for the sake of simplicity, which is called Voigt notation. The index relations between ij and p are shown in Tab. 2.1. It has to be noted that the sequence of this mapping relationship may be different in some numerical softwares, a unified assignment in advance is thus necessary.

p	1	2	3	4	5	6
ij	11	22	33	23	31	12

Table 2.1.: Representation of Voigt notation.

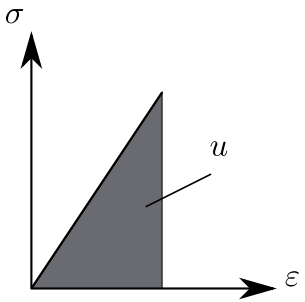

Figure 2.1.: The linear elastic stress-strain diagram with shadowed area under the line indicating the stored specific elastic energy.

Differentiation with respect to a coordinate in the index notation is expressed by a comma in the subscript, e.g., the displacement gradient

$$u_{i,j} = \frac{\partial u_i}{\partial x_j}. \tag{2.2}$$

2.1.2. Linear elasticity

The linear relation between loading and deformation in a solid object is generally known as Hooke's law [79]. In a very simple way, if only a tensile stress is applied and causes elongation of the considered element, referring to the stress–strain curve as shown in Fig. 2.1, the modulus of elasticity E is given by

$$E = \frac{\sigma}{\varepsilon}, \tag{2.3}$$

where σ and ε are stress and strain, respectively. This relationship presumes that the stress is smaller than the yield stress σ^Y, thus only the simple linear behavior is considered.

For a three dimensional state of stress and strain, the generalized Hooke's law for a homogeneous material is

$$\sigma_{ij} = C_{ijkl}\varepsilon_{kl}, \tag{2.4}$$

where C_{ijkl} is the fourth-order stiffness tensor. In the stress tensor there are six independent components due to the symmetric property of the Cauchy stress σ_{ij} according to the balance of angular momentum. Since many materials used in engineering structures have large elastic constants, an infinitely small deformation is assumed, which lets

$$\varepsilon_{ij} = \frac{1}{2}(u_{i,j} + u_{j,i}) \tag{2.5}$$

and apparently

$$\varepsilon_{ij} = \varepsilon_{ji}, \tag{2.6}$$

leading to six independent components in the strain tensor.

The specific internal energy is expressed as the specific reversible work done by the stresses in all directions, if no dissipation of energy takes place. The reversible work is stored within the body in the form of strain energy, which is illustrated in Fig. 2.1 as the gray area for a uniaxial case. Comprising all the components of the stress and strain tensors in a general case, the specific elastic internal energy u is given by

$$u = \frac{1}{2}\sigma_{ij}\varepsilon_{ij}. \tag{2.7}$$

Based on Eqs. (2.4) and (2.7), the elastic tensor can be rewritten according to

$$C_{ijkl} = \frac{\partial^2 u}{\partial\varepsilon_{ij}\partial\varepsilon_{kl}}. \tag{2.8}$$

Taking account of Schwarz's theorem in Eq. (2.8) and the symmetries of the stress and strain tensors, the elastic tensor has the following symmetric properties

$$C_{ijkl} = C_{ijlk} = C_{klij} = C_{jikl}, \tag{2.9}$$

which leads to the number of the independent constants in C_{ijkl} being reduced from 81 to 21 in the most general case of anisotropy and strain coupling. Since the internal energy density u must be positive due to an arbitrary deformation, the condition

$$C_{ijkl}\varepsilon_{ij}\varepsilon_{kl} > 0 \tag{2.10}$$

must be satisfied, which indicates that the elastic tensor is positive definite.

2.1.3. Transformation of coordinates

In many mechanical problems, different coordinate systems are used in order to describe quantities in an appropriate way. The analysis of the quantities based on different coordinate systems only make sense if all the quantities involved are given in the same frame. Therefore, a general operation has to be introduced for transforming the quantities from one coordinate system x_i to another $\hat{x}_i$. The transformation matrix of a two-dimensional case, see Fig. 2.2, is defined as

$$\begin{aligned}\Omega_{ij} &= \hat{\vec{e}}_i \cdot \vec{e}_j = |\hat{\vec{e}}_i||\vec{e}_j|\cos(\hat{\vec{e}}_i, \vec{e}_j) \\ &= \begin{pmatrix} \cos\varphi & \sin\varphi \\ -\sin\varphi & \cos\varphi \end{pmatrix},\end{aligned} \tag{2.11}$$

where φ is the angle between the coordinate systems, and $\vec{e}_i$ and $\hat{\vec{e}}_i$ are the basis unit vectors of the x_i- and $\hat{x}_i$-axis, respectively. The transformation matrix thus presents an

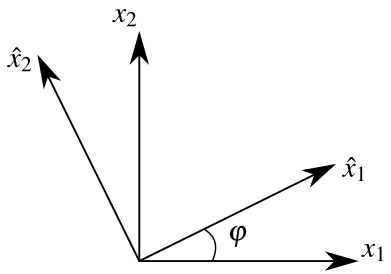

Figure 2.2.: Two orthonormal coordinate systems with a relative angle φ.

orthogonal matrix and holds the orthogonality condition

$$\Omega_{ij} = \Omega_{ji}^{-1} \quad \text{and thus} \quad \Omega_{ij}\Omega_{kj} = \delta_{ik}, \tag{2.12}$$

where δ_{ik} is the Kronecker delta, which is equal to 1 if $i = j$ and zero if $i \neq j$. Hence, the tensors of different order referring to the $\hat{x}_i$-coordinate are obtained as

$$\begin{aligned} \hat{\psi} &= \psi, \\ \hat{\psi}_i &= \Omega_{ij}\psi_j, \\ \hat{\psi}_{ij} &= \Omega_{ik}\Omega_{jl}\psi_{kl}, \\ \hat{\psi}_{ijkl} &= \Omega_{im}\Omega_{jn}\Omega_{kp}\Omega_{lq}\psi_{mnpq}. \end{aligned} \tag{2.13}$$

There is another widely used coordinate system, the polar coordinate system, denoted by the radial coordinate r and the angular coordinate φ [167]. Polar coordinates are especially appropriate and practical if the required field variables are tied to the direction and length from a center point, e.g., a crack tip. The transformation of a stress state from a Cartesian coordinate system into a polar coordinate system is illustrated in Fig. 2.3 and yields the expressions as follows

$$\begin{aligned} \sigma_{rr} &= \sigma_{11}\cos^2\varphi + \sigma_{22}\sin^2\varphi + \sigma_{12}\sin 2\varphi, \\ \sigma_{\varphi\varphi} &= \sigma_{11}\sin^2\varphi + \sigma_{22}\cos^2\varphi - \sigma_{12}\sin 2\varphi, \\ \sigma_{r\varphi} &= \sin\varphi\cos\varphi(\sigma_{22} - \sigma_{11}) + \sigma_{12}\cos 2\varphi. \end{aligned} \tag{2.14}$$

The derivatives can also be transformed from one coordinate to another, e.g., the gradient of a field, given as function in the polar coordinate system, is differentiated by the x_1 and x_2 as follows:

$$\begin{aligned} \frac{\partial f(r,\varphi)}{\partial x_1} &= \frac{\partial f}{\partial r}\frac{\partial r}{\partial x_1} + \frac{\partial f}{\partial \varphi}\frac{\partial \varphi}{\partial x_1} = \cos\varphi\frac{\partial f}{\partial r} - \frac{\sin\varphi}{r}\frac{\partial f}{\partial \varphi}, \\ \frac{\partial f(r,\varphi)}{\partial x_2} &= \frac{\partial f}{\partial r}\frac{\partial r}{\partial x_2} + \frac{\partial f}{\partial \varphi}\frac{\partial \varphi}{\partial x_2} = \sin\varphi\frac{\partial f}{\partial r} + \frac{\cos\varphi}{r}\frac{\partial f}{\partial \varphi}. \end{aligned} \tag{2.15}$$

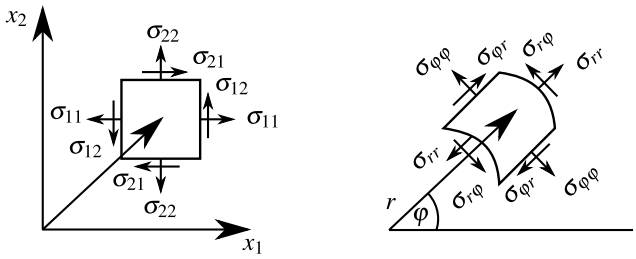

Figure 2.3.: Illustration of a stress state in orthonormal Cartesian and polar coordinate systems.

2.1.4. Isotropy and transverse isotropy

As previously introduced, the stiffness tensor C_{ijkl} has not more than 21 independent constants due to the symmetric properties. If a material has an intrinsic plane of symmetry, which implies that the stress–strain relations are identical in some directions, the number of the independent constants in C_{ijkl} can further be reduced. Many engineering materials show very limited elastic anisotropy and thus can be treated as isotropic materials. The elastic tensor of an isotropic material reads

$$C_{ijkl} = \lambda\,\delta_{ij}\delta_{kl} + \mu(\delta_{ik}\delta_{jl} + \delta_{il}\delta_{jk}), \tag{2.16}$$

where λ and μ are the Lamé constants and have the relation with the elastic modulus E and the Poisson's ratio ν as follows

$$\lambda = \frac{E\nu}{(1+\nu)(1-2\nu)} \quad \text{and} \quad \mu = \frac{E}{2(1+\nu)}. \tag{2.17}$$

Since any plane in isotropic materials is a plane of symmetry, the elastic constants in C_{ijkl} are independent of the coordinate system.

Unlike the isotropic materials, a transversely isotropic material has one axis of symmetry and any plane containing this axis is a symmetry plane, while planes perpendicular to this axis exhibit isotropic behavior. Setting the x_2-axis as the symmetry axis, the Hooke's law thus is given by

$$\begin{pmatrix}\sigma_{11}\\ \sigma_{22}\\ \sigma_{33}\\ \sigma_{23}\\ \sigma_{13}\\ \sigma_{12}\end{pmatrix} = \begin{pmatrix} C_{1111} & C_{1122} & C_{1133} & 0 & 0 & 0\\ C_{1122} & C_{2222} & C_{1122} & 0 & 0 & 0\\ C_{1133} & C_{1122} & C_{1111} & 0 & 0 & 0\\ 0 & 0 & 0 & C_{2323} & 0 & 0\\ 0 & 0 & 0 & 0 & C_{1313} & 0\\ 0 & 0 & 0 & 0 & 0 & C_{2323}\end{pmatrix} \begin{pmatrix}\varepsilon_{11}\\ \varepsilon_{22}\\ \varepsilon_{33}\\ 2\varepsilon_{23}\\ 2\varepsilon_{13}\\ 2\varepsilon_{12}\end{pmatrix} \tag{2.18}$$

with $C_{1313} = (C_{1111} - C_{1133})/2$, whereupon five independent constants are required. It

is noted that the material behavior of a transversely isotropic material in plane problems is related to the coordinate system, unless the symmetry axis is perpendicular to the considered plane constituting the isotropic exception. Hence, if another coordinate system is taken into account, the material constants must be transformed into the new coordinate system by using Eq. (2.13).

2.1.5. State of plane stress and plane strain

A widespread simplification of a three-dimensional problem, reduced to the one only involving two dimensions, is often of special importance for less complexity and lower computational cost. With regard to the stress or strain state being neglected in the third dimension, there are two possible descriptions, i.e., plane stress and plane strain [79]. Considering a thin plate in the x_1-x_2 plane loaded by forces in the plane, all stress components in x_3-direction are assumed to be zero, namely $\sigma_{i3} = 0$. This description is called plane stress and the simplified constitutive equations are

$$\begin{pmatrix} \sigma_{11} \\ \sigma_{22} \\ \sigma_{12} \end{pmatrix} = \frac{E'}{1-\nu'^2} \begin{pmatrix} 1 & \nu' & 0 \\ \nu' & 1 & 0 \\ 0 & 0 & (1-\nu')/2 \end{pmatrix} \begin{pmatrix} \varepsilon_{11} \\ \varepsilon_{22} \\ 2\varepsilon_{12} \end{pmatrix} \tag{2.19}$$

for isotropic materials, where $E' = E$ and $\nu' = \nu$, and

$$\begin{pmatrix} \sigma_{11} \\ \sigma_{22} \\ \sigma_{12} \end{pmatrix} = \begin{pmatrix} C_{1111} - \frac{C_{1133}C_{1133}}{C_{1111}} & C_{1122} - \frac{C_{1122}C_{1133}}{C_{1111}} & 0 \\ C_{1122} - \frac{C_{1122}C_{1133}}{C_{1111}} & C_{2222} - \frac{C_{1122}C_{1122}}{C_{1111}} & 0 \\ 0 & 0 & C_{2323} \end{pmatrix} \begin{pmatrix} \varepsilon_{11} \\ \varepsilon_{22} \\ 2\varepsilon_{12} \end{pmatrix} \tag{2.20}$$

for transversely isotropic (x_2-axis as symmetry axis) materials.

Plane strain is a similar simplification just on the contrary side of a plane stress condition, where the dimension of the body in x_3-direction is assumed extremely large and all cross sections along the x_3-direction are expected to experience the same in-plane deformation and stress state. For the case described, the components of the strain tensor related to x_3 is considered as zero and the constitutive equations for transverse isotropy are the same as Eq. (2.18) only with $\varepsilon_{i3} = 0$. For isotropic materials, Eq. (2.19) can be easily converted into the equations for plane strain by inserting $E' = E/(1-\nu^2)$ and $\nu' = \nu/(1-\nu)$.

Another commonly used set of material coefficients for planar problems is κ and μ. κ is defined as $3-4\nu$ for plane strain and $(3-\nu)/(1+\nu)$ for plane stress, respectively, and μ is the shear modulus of elasticity. Thus, E' for plane strain and plane stress are unified and expressed by κ and μ as:

$$E' = \frac{8\mu}{1+\kappa}. \tag{2.21}$$

2.2. Fundamentals of piezo- and ferroelectrics

2.2.1. Piezoelectricity

Piezoelectricity is a property of some classes of i.a. crystalline materials being able to generate electric charge in response to a mechanical load or, conversely, being deformed if an electric field is applied. This linear reversible electromechanical interaction, called (inverse) piezoelectric effect, was discovered by the Curie brothers about one and a half centuries ago and is only possible in dielectric materials, where the electric charges cannot freely move [141]. The precondition of a crystalline material performing piezoelectricity is that its unit cell structure lacks a center of symmetry. Among 32 existing classes of crystals, there are 21 noncentrosymmetric crystallographic classes and 20 of them show piezoelectricity [20]. A piezoelectric procedure in a noncentrosymmetric unit cell is schematically shown in Fig. 2.4, where the ions of the unit cell leave their equilibrium positions due to the deformation. Consequently, an electric dipole moment is induced since the centers of the positive and negative charges are no longer at the same position, leading to a polarized state in the unit cell.

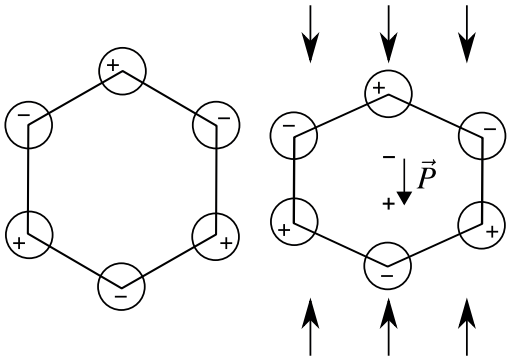

Figure 2.4.: A unit cell of a piezoelectric crystal. The unit cell is in neutral state and has no polarization (left) until e.g. a compressive stress is exerted (right), where $\vec{P}$ denotes the induced electric dipole moment density known as (specific) polarization.

In a piezoelectric material, the polarization P_i is proportional to the electric field E_i

$$P_i = \kappa_0(\kappa_r - 1)E_i, \tag{2.22}$$

where $\kappa_0 \approx 8.854 \times 10^{-12}$ As/Vm is the permittivity of vacuum and κ_r is the relative permittivity of the material [140]. Based on the constitutive relations of dielectrics, an

electric displacement is introduced as follows

$$D_i = \kappa_0 E_i + P_i = \kappa_0 \kappa_r E_i, \tag{2.23}$$

if no additional polarization is present.

Similar to the Cauchy stress on a surface, the electric displacement on the electric boundary characterizes the balance of charges

$$D_i n_i = -\omega_A, \tag{2.24}$$

where ω in general is the density of electric charges, the subscript A indicates surface area and n_i is the normal vector of the surface [162].

2.2.2. Ferroelectricity

Among the piezoelectric crystal classes, there is a subgroup of materials, which have a natural electric polarization in the absence of an external electric field or mechanical loading [54]. The natural polarization is called spontaneous polarization. This spontaneous polarization state can be changed into different directions due to an external loading and this effect is termed ferroelectricity in analogy to ferromagnetism. Most of the applied ferroelectrics, e.g., BT, PZT and KNN, have a similar crystalline, so called perovskite, structure with the chemical formula ABX_3, where A and B are two cations and X is oxygen. Fig. 2.5 shows one unit cell of BT in the tetragonal phase, where the Ba^{2+} take the corner positions and O^{2-} sit at the face centers. The Ti^{4+} ion deviates from the body center position and thus induces a spontaneous polarization. Heating the ferroelectrics to a certain temperature, the tetragonal phase transits to a cubic phase and the Ti^{4+} atom moves to the body center, whereupon the spontaneous polarization vanishes and the material loses its ferroelectricity. The critical temperature, called Curie temperature (T_c), is a material parameter and varies greatly for different material classes. In the case of BT it is around 120°C, while for PZT ceramics T_c is between 200°C and 450°C [6]. In applications of ferroelectricity, the Curie temperature should not be surpassed to avoid losing a poling state.

The state of the spontaneous polarization in BT can be altered if the material is subjected to an electric field or a mechanical loading, making both the Ti^{4+} ion and the oxygen octahedron leave their stable positions. Once the energy fluctuation induced by external loads overcomes the energy barrier, where another equilibrium state is available, the polarization turns into a new direction and keeps the state. All possible reorientations for polarizations in a tetragonal phase are shown in Fig. 2.6. If a reorientation is driven by an electric loading, it is termed ferroelectric effect and on the other side, it is a ferroelastic effect if the polarization change is induced by mechanical loadings. During the 90° direction switching process, the unit cell is deformed, retaining the length of c parallel to the polarization. The mechanical strain due to the deformation is inelastic and termed spontaneous strain. Assuming infinitesimal strain while

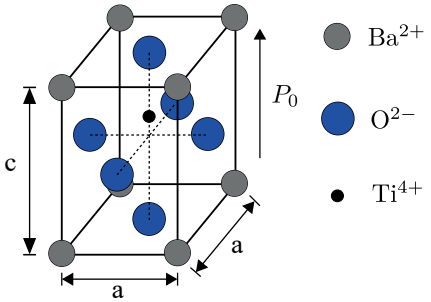

Figure 2.5.: A tetragonal unit cell of $BaTiO_3$ shows the spontaneous polarization denoted as P_0.

$c/a \approx 1$[1], the spontaneous strain of a tetragonal unit cell induced by a 90° switching is approximated by

$$\varepsilon_D = \frac{c-a}{a_0}, \tag{2.25}$$

where a_0 denotes the edge length of a cubic cell above T_c [118]. Compared to the spontaneous strain of magnitude between 1% to 5% [25], the electrostrictive strain is much lower, e.g., maximum 0.4% for PIC-151 material [162]. Apparently, a 180° switching is not accompanied by unit cell deformation and thus cannot take place as a result of mechanical stresses but only of an electric field against the poling direction. The required electric field is called coercive field E_c.

Industrial ferroelectric devices are commonly polycrystals and have domain structures, in which the polarization states of the domains are initially not aligned. High resolution pictures and schematic illustrations of domain structures can be found in [141]. Although every domain in polycrystals has its own polarization, the materials may not show any polarization on the macroscopic level, since the randomly distributed polarization states are neutralized. Applying a sufficiently large electric field, normally much higher than E_c, the domains switch their polarization directions predominantly along the electric field and the polycrystals thus manifest a macroscopic polarization. This process is called poling and the macroscopic polarization state of the polycrystals is designated as poling direction.

Since the 90° domain switching changes the shape of unit cells, structural mismatch is induced between the adjacent domains. Driven by the mismatch, damage and cracks tend to be initiated and emanated [57, 75, 119]. The ferroelectric nonlinear behavior with the additional electric field singularity at the crack tip makes the fracture mechanical understanding and the calculation of loading quantities in a crack assessment more complex.

[1] for example, $a = 3.9932 \pm 0.0002$Å and $c = 4.0341 \pm 0.0003$Å for BT [120]

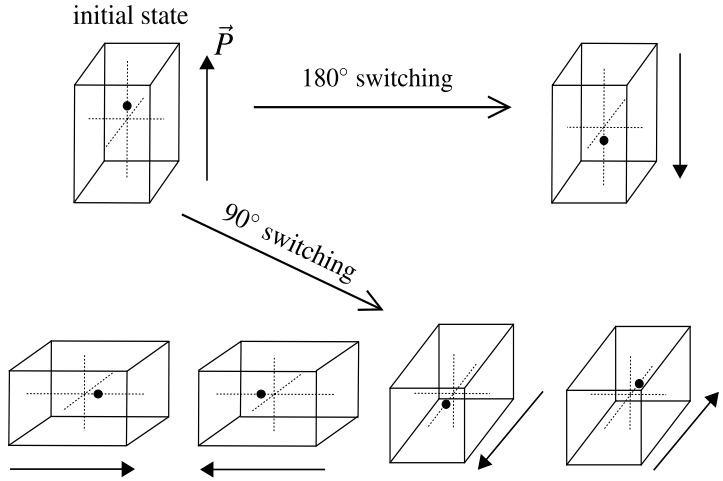

Figure 2.6.: The spontaneous polarization $\vec{P}$ (arrow) switches in a BT unit cell. The ions of the unit cell are omitted here except for the Ti^{4+} as a solid black dot near the body center position. Two types of domain switching, 180° and 90°, are illustrated. While a 90° switching can be induced by applying a mechanical load or an electric load, a 180° switching is only caused by an electric field.

2.2.3. Constitutive equations of piezoelectrics

The first law of thermodynamics for a closed system written in differential form is given as

$$\mathrm{d}u = \mathrm{d}w + \mathrm{d}q, \tag{2.26}$$

where w and q are the specific work done by e.g. stress and electric field and the specific heat exchange, respectively. Confining the system as isentropic ($\mathrm{d}s = 0$), it yields

$$\mathrm{d}w = \mathrm{d}w_{rev} \quad \text{and} \quad \mathrm{d}q = 0, \tag{2.27}$$

which means that the system is adiabatic and without dissipative specific work. Thus,

$$\mathrm{d}u = \mathrm{d}w_{rev}. \tag{2.28}$$

w_{rev} is the specific reversible work and consists of two parts in piezoelectrics, i.e.

$$\mathrm{d}w_{rev} = \mathrm{d}w^m + \mathrm{d}w^e, \tag{2.29}$$

where the superscripts m and e denote the mechanical and electrical parts, respectively. Considering a driving force on the electric charges in an electric field E_i and introducing the electric displacement (electric flux density) D_i, which describes the charge per

unit area and constitutes the work associated quantity, the electric work $\mathrm{d}w^e$ reads

$$\mathrm{d}w^e = \omega E_i \mathrm{d}l_i = E_i \mathrm{d}D_i \tag{2.30}$$

with $\mathrm{d}l_i$ as an incremental length along the electric field and ω as the surface density of electric charge. Substituting the differential form of Eq. (2.7) and Eq. (2.30) into Eqs. (2.29) and (2.28), the specific internal energy in a reversible process is obtained:

$$\mathrm{d}u = \sigma_{ij}\mathrm{d}\varepsilon_{ij} + E_i \mathrm{d}D_i. \tag{2.31}$$

Besides $u(\varepsilon_{ij}, D_i)$, another important thermodynamic potential in piezoelectric mechanics, the specific electric enthalpy Π, depending on the conjugate variable E_i, is derived applying the Legendre transformation to the internal energy density:

$$\Pi(\varepsilon_{ij}, E_i) = u - E_i D_i = \frac{1}{2}\sigma_{ij}\varepsilon_{ij} - \frac{1}{2}E_i D_i \tag{2.32}$$

and in differential form:

$$\mathrm{d}\Pi = \mathrm{d}u - E_i \mathrm{d}D_i - D_i \mathrm{d}E_i = \sigma_{ij}\mathrm{d}\varepsilon_{ij} - D_i \mathrm{d}E_i. \tag{2.33}$$

The total differential of the electric enthalpy density with respect to the associated variables is

$$\mathrm{d}\Pi = \left(\frac{\partial \Pi}{\partial \varepsilon_{ij}}\right)_{E_i} \mathrm{d}\varepsilon_{ij} + \left(\frac{\partial \Pi}{\partial E_i}\right)_{\varepsilon_{ij}} \mathrm{d}E_i \tag{2.34}$$

and comparing to Eq. (2.33), the stress and electric displacement are expressed as

$$\begin{aligned} \sigma_{ij} &= \left(\frac{\partial \Pi}{\partial \varepsilon_{ij}}\right)_{E_i}, \\ D_i &= -\left(\frac{\partial \Pi}{\partial E_i}\right)_{\varepsilon_{ij}}. \end{aligned} \tag{2.35}$$

The state variables as subscripts outside the parentheses imply that the terms hold by constant electric field or strain. The stress σ_{ij} and the electric displacement D_i are further differentiated by the variables ε_{ij} and E_i, considering their total differentials:

$$\begin{aligned} \mathrm{d}\sigma_{ij}(\varepsilon_{kl}, E_k) &= \left(\frac{\partial \sigma_{ij}}{\partial \varepsilon_{kl}}\right)_{E_k} \mathrm{d}\varepsilon_{kl} + \left(\frac{\partial \sigma_{ij}}{\partial E_k}\right)_{\varepsilon_{kl}} \mathrm{d}E_k, \\ \mathrm{d}D_i(\varepsilon_{kl}, E_k) &= \left(\frac{\partial D_i}{\partial \varepsilon_{kl}}\right)_{E_k} \mathrm{d}\varepsilon_{kl} + \left(\frac{\partial D_i}{\partial E_k}\right)_{\varepsilon_{kl}} \mathrm{d}E_k. \end{aligned} \tag{2.36}$$

Substituting Eq. (2.35) into the right sides of Eq. (2.36), the following material constants are derived from the electric enthalpy density:

$$\begin{aligned} C_{ijkl} &= \left(\frac{\partial \sigma_{ij}}{\partial \varepsilon_{kl}}\right)_{E_k} = \left(\frac{\partial^2 \Pi}{\partial \varepsilon_{ij} \partial \varepsilon_{kl}}\right)_{E_k}, \\ e_{ijk} &= -\left(\frac{\partial \sigma_{ij}}{\partial E_k}\right)_{\varepsilon_{kl}} = -\left(\frac{\partial^2 \Pi}{\partial \varepsilon_{ij} \partial E_k}\right) = \left(\frac{\partial D_k}{\partial \varepsilon_{ij}}\right)_{E_i}, \\ \kappa_{ik} &= \left(\frac{\partial D_i}{\partial E_k}\right)_{\varepsilon_{kl}} = -\left(\frac{\partial^2 \Pi}{\partial E_i \partial E_k}\right)_{\varepsilon_{kl}}, \end{aligned} \tag{2.37}$$

where κ_{ik} represent the dielectric constants and e_{ijk} the piezoelectric coefficients, respectively. Similar to the elastic moduli by considering Schwarz's theorem in Eq. (2.9), the tensors of dielectric constants and piezoelectric coefficients have symmetric properties as follows:

$$\begin{aligned} e_{ijk} &= e_{jik} = e_{kij} = e_{kji}, \\ \kappa_{ik} &= \kappa_{ki}. \end{aligned} \tag{2.38}$$

Combining Eqs. (2.36) and (2.37) and integrating finite changes of state, where the material coefficients remain constant, the linear constitutive equations of piezoelectric materials are obtained as

$$\begin{aligned} \sigma_{ij} &= C_{ijkl}\varepsilon_{kl} - e_{ijk}E_k, \\ D_i &= e_{kli}\varepsilon_{kl} + \kappa_{ik}E_k. \end{aligned} \tag{2.39}$$

The electric enthalpy density according to Eq. (2.32) thus reads

$$\Pi(\varepsilon_{ij}, E_i) = \frac{1}{2} C_{ijkl}\varepsilon_{ij}\varepsilon_{kl} - e_{ijk}E_k\varepsilon_{ij} - \frac{1}{2}\kappa_{ik}E_iE_k. \tag{2.40}$$

Nonlinear ferroelectric constitutive behavior is readily obtained from Eq. (2.39), introducing inelastic strain ε_{ij}^{irr} and change of spontaneous polarization P_i^{irr} due to domain switching yielding

$$\begin{aligned} \sigma_{ij} &= C_{ijkl}(\varepsilon_{kl} - \varepsilon_{kl}^{irr}) - e_{ijk}E_k, \\ D_i &= e_{kli}(\varepsilon_{kl} - \varepsilon_{kl}^{irr}) + \kappa_{ik}E_k + P_i^{irr}, \end{aligned} \tag{2.41}$$

where ε_{kl} now denotes the total strain.

Due to the transversally isotropic behavior in piezoelectric materials in tetragonal phase, only three piezoelectric and two dielectric constants are required. If the x_1-x_3 plane is the isotropic plane and the x_2-axis is parallel to the poling direction, the

material tensors read

$$e_{kli} = \begin{pmatrix} 0 & 0 & 0 & 0 & 0 & e_{121} \\ e_{112} & e_{222} & e_{332} & 0 & 0 & 0 \\ 0 & 0 & 0 & e_{233} & 0 & 0 \end{pmatrix}, \quad e_{112} = e_{332}, \quad e_{121} = e_{233}, \tag{2.42}$$

$$\kappa_{ik} = \begin{pmatrix} \kappa_{11} & 0 & 0 \\ 0 & \kappa_{22} & 0 \\ 0 & 0 & \kappa_{33} \end{pmatrix}, \quad \kappa_{11} = \kappa_{33}, \tag{2.43}$$

where the compressed Voigt notation is applied in Eq. (2.42)

2.3. Framework of linear elasticity in quasicrystals

2.3.1. Introduction to quasicrystals

Prior to the discovery of the first quasicrystal in 1982 and the universal acceptation of the definition in academia, the conceptions of order and periodicity were synonymous in crystallography, meaning that a crystal is made up of a pattern perfectly repeating itself and the structure is gapless if no defect is considered [194]. Thus, a crystalline structure has both rotational and translational symmetry. Due to these restrictions, the structures or the patterns can only show certain symmetries (2-, 3-, 4- and 6-fold), which are called crystallographic restrictions [21]. The number of the fold indicates the ways that the pattern can be rotated to reproduce an identical pattern as the original. The periodic constructions of crystals were confirmed with the development of X-ray crystallography and other experimental techniques. However, the confirmation by such experiments is mostly implicit. The standard methods, i.e., X-ray and electron diffraction techniques, shooting X-ray or electrons from different directions towards specimens, provide diffraction pictures with sharp peaks (Bragg peaks), which can intuitively indicate the symmetry property of crystals but not the real crystalline structure. Dealing with the diffraction patterns, some mathematical treatment is required to finally determinate the crystalline structure. The detailed procedure can be found in [185].

The understanding of crystals has been challenged by an experimental finding, which was obtained in 1982 and published two years later [176]. The diffraction pictures of a rapidly cooled Al alloy with Mn, Fe or Cr, see Fig. 2.7(a), have clear sharp peaks, which indicate the order of the structure, however, it shows a fivefold symmetry impossible for crystals. Almost at the same time, a feasible structure with icosahedral lattice based on two unit cells was proposed and the diffraction pattern of this aperiodic packing was computed [124], see Fig. 2.7(b). The agreement between the diffraction patterns from the experiment and the calculation points out that the fivefold symmetric diffraction is not a mistake of crystal twinning, as some crystallographers

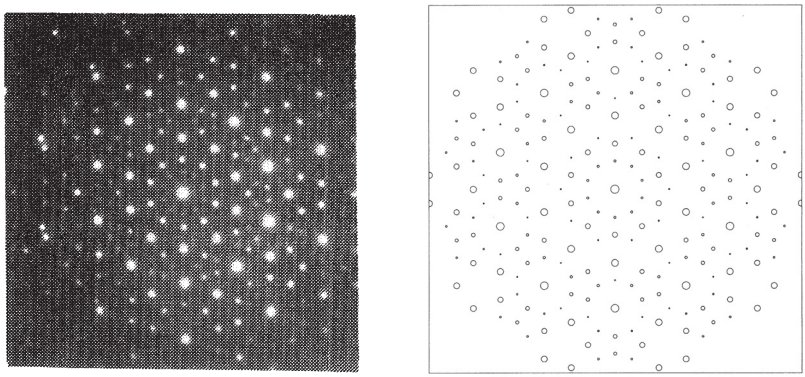

(a) (b)

Figure 2.7.: Diffraction patterns (a) taken experimentally from a single grain Al-Mn alloy [176] and (b) computed based on an ideal icosahedral model, where the circles are at the location of Bragg peaks and the sizes are proportional to their intensity [124].

believed, but that the well-ordered material really exists, although its structure violates the crystalline symmetry rules. Not like classical crystals with rigorous periodic atomic/molecular structures, this kind of materials shows long-range orientational order, however, lacks i-dimensional (i=1,2,3) translational periodicity in its spatial structure. The distribution of atoms/molecules is quasiperiodic and still has crystalline features in short order. Hence, the materials with such structures are termed quasiperiodic crystals, or quasicrystals (QCs) for short [124] and have been officially accepted by the International Union of Crystallography [3].

The concept of quasiperiodicity is young in crystallography, however, has been familiar to mathematicians for a long time. Quasiperiodic functions, being functions with a certain similarity to periodic functions but without a strict periodicity, have been extensively studied in mathematics and provide useful tools for describing the lattice structure of QCs [96]. Regarding to classical crystals, three independent basis vectors of the function of periodicity span a reciprocal lattice, which can describe the arrangement of the unit cells and indicate the intensity of the sharp Bragg peaks [194], whereas the rank of the quasiperiodic functions for QCs is higher than three, leading to more than three basis vectors. The excessive basis vectors can be considered, in a simple way, as additional dimensions for representing the quasiperiodicity. One example of this is a bulk material having many stacked crystalline layers, where the layers are ordered quasiperiodically in the third direction. It requires four basis vectors for the corresponding quasiperiodic function, two in the crystalline layer and the other two in the quasiperiodic direction. The basis vectors can be determined by the diffraction pattern, being of great importance for the understanding of the quasicrystalline structure. The details of the mathematic and crystallographic theory in QCs can be found in [190, 200].

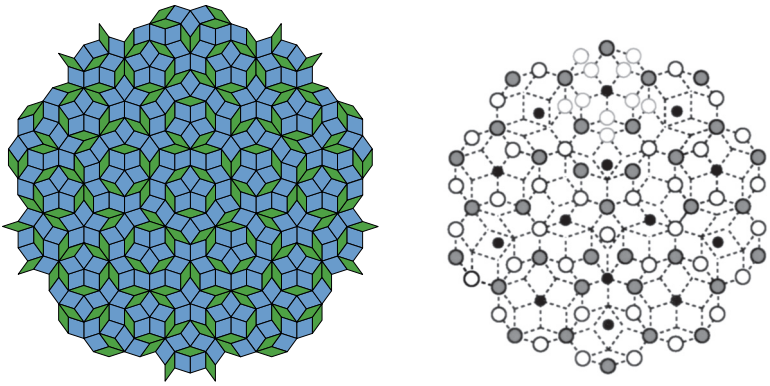

(a) (b)

Figure 2.8.: (a) A Penrose tiling shows fivefold symmetry [1] and (b) the model of ZnMgRE is consistent with the Penrose tiling [4]

One of the most famous quasiperiodic structures is the Penrose rhomb tiling [155], which was constructed by Sir Roger Penrose for purely mathematical purpose and shows fivefold symmetry, see Fig. 2.8(a). The rhomb tiling consists of two unit parts, a "skinny" type (36° and 144°) and a "fat" type (72° and 108°). Locally, the tiling is simply arranged without any gap and the single tile is not just neatly repeated. The rhombs seem to be constructed randomly, in fact, the structure is predictable based on a so-called matching rule, which arranges the joint of tiles and ensures the quasiperiodicity of the structure [100]. There are also many other types of tilings, e.g., planar tilings similar to the illustrated rhomb tiling and spatial tilings being generalized from a two-dimensional tiling [43, 187]. The tilings are not only jigsaw puzzles but correspond to the atomic structures of real QCs. Fig. 2.8(b) shows a structure model of a decagonal quasicrystal ZnMgRE (RE= rare earth), which exhibits exactly the Penrose rhomb tiling. This structure was confirmed by using the high-resolution transmission electron microscopy (HRTEM), which directly observed the arrangement of atoms on its two-dimensional quasiperiodic lattice plane [4]. More observations of QCs and the related tilings have been reported, e.g., [86] and [62]. It has to be noted that showing a forbidden point symmetry in the diffraction pattern is not a rigid judging criterion of quasiperiodic structures. One of the simple examples is a square Fibonacci tiling with two-dimensional quasiperiodic arrangement, which has the 4mm crystallographic point symmetry [127]. Generally, the quasiperiodic structural materials with crystallographic point symmetry are dealt with in the theme of incommensurately modulated crystals instead of QCs [187].

Since the discovery of the very first QC, which was unstable at room temperature, a lot of works have been done to find new quasicrystalline materials with useful physical properties and to prepare stable QCs. The first stable icosahedral QC was discovered in the system Al-Cu-Li [41]. The first stable decagonal Al-Cu-Co QC was reported in 1988 [82] and the first dodecagonal phase QC in 1994 [29]. All kinds of stable QCs

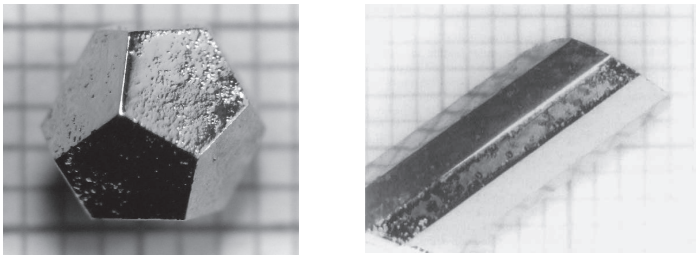

(a) (b)

Figure 2.9.: Photographs of single-grain (a) icosahedral Ho-Mg-Zn QC [58] and (b) decagonal Al-Ni-Co QC [60], grown from the ternary melt (edges of grid indicate 1 mm).

were deemed in ternary compounds until the first stable binary icosahedral QCs were found in Ca-Cd and Yb-Cd [18]. Up to date, QCs are known to be formed in more than 100 systems with Al, Ga, Cu, Ca, Ni, Ti, Ta and many other elements [197]. About 50 types of QCs that have been found are stable at room temperature and the number is still growing [186]. Fig. 2.9 shows two single-grain quasicrystalline samples made by the researchers of Ames Laboratory (United States Department of Energy National Laboratory), USA, reported in 1999. These single-grain samples, grown from the ternary melt, have the size of several millimeters. Especially, the pentagonal facets and the dodecahedral morphology in Fig. 2.9(a), without any machining process, reflects its basic symmetry property of the quasicrystalline structure. In order to measure the physical properties of QCs, many research groups have made an effort for producing large size single-grain QCs or single crystal approximants of QCs. Approximants are conventional crystals which have the same type of chemical formula and similar local structure (atomic cluster) of the related QCs, normally being employed for studies of the physical properties of QCs [187]. Fig. 2.10 and Fig. 2.11 show several examples of approximants and the Al-Ni-Co QC with two quasiperiodic directions grown by using the Czochralski method.

Although QCs are still subject to very basic research in the physicist's and chemist's communities, they manifest many useful properties and promising applications due to their peculiar structure. Generally, QCs have high hardness and strength and thus are ideal reinforcement materials in metal or polymer composites [207]. One industrial example has been developed with icosahedral nanoparticles, called maraging stainless steel, exhibiting outstanding mechanical properties [129]. Another typical application in reinforced materials is the rapid prototyping of parts with complex structures made by selective laser sintering, where icosahedral quasicrystalline powders are used instead of the traditional glass fiber. Fig. 2.12(a) shows an example produced by the patented rapid prototyping technique, which can be used directly in a real test environment due to its sufficient strength. Beyond that, the wetting behavior, namely anti-adhesion and low friction, enable QCs to be prominent surface coating materials or thin films [40, 66, 108]. Combining other outstanding properties, such as wear and

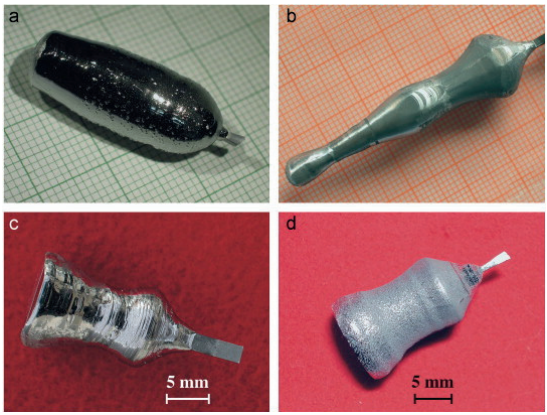

Figure 2.10.: Four examples of Czochralski-grown single crystals of the approximants of Al-Co-Ni [76]. The grid size in a and b is 1 mm.

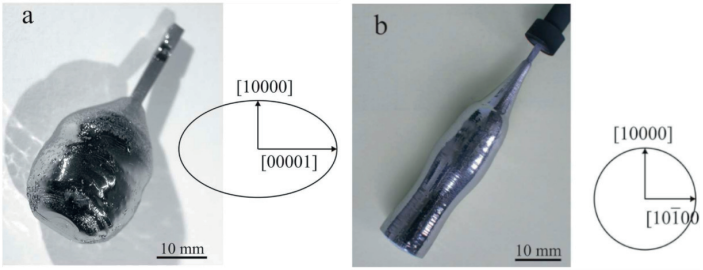

Figure 2.11.: Examples of single-grain Al-Co-Ni QC grown along (a) the quasiperiodic direction and (b) the periodic direction and the corresponding cross-sections [135].

corrosion resistance, the quasicrystalline coating can be used in many demanding applications, e.g., surgical scalpels, razor blades or frying pans, see Fig. 2.12(b). Many other properties of QCs are also in the focus of research and show great potential in applications, e.g., as optical materials for manipulating color or visibility and as hydrogen storage materials [39, 109]. More physical properties and possible applications are summarized in [24, 38].

2.3.2. Phonon and phason fields in QCs

According to Landau's theory [117], the atoms in crystals, and QCs as well, do not stay precisely in fixed places of the body. Due to the effect of thermal energy they oscillate around their equilibrium positions. For an exact statistical description of the

(a) (b)

Figure 2.12.: (a) A selective laser sintering composite part consisting of a polymer matrix reinforced by quasicrystalline Al-Cu-Fe particles [110] and (b) frying pans with quasicrystalline coating, patented as Cybernox, which is 10 times harder than stainless steel and extremely durable [2].

atomic arrangement and position, a mass density function of an atom at position r_i is introduced [93]. For a periodic structure, the averaged mass density function ρ can be expressed as a discrete Fourier sum

$$\rho(r_i) = \sum_{G_j} \rho(G_j) \exp\{i G_j r_j\}, \tag{2.44}$$

where G_j are the basis vectors of the reciprocal lattice and i is the imaginary unit. The reciprocal lattice represents the Fourier transformation of the real lattice and is fundamental for crystallographic analysis. The periodicity of crystalline structures is satisfied by $\rho(r_i) = \rho(r_i + R_i)$ for every basis vector R_i in the real lattice. Each Fourier coefficient $\rho(G_j)$ is a complex order parameter, consisting of a magnitude ρ_{G_j} and a phase angle ϕ_{G_j}:

$$\rho(G_j) = \rho_{G_j} \exp\{i \phi_{G_j}\}. \tag{2.45}$$

The magnitude ρ_{G_j} is a state parameter, being dependent on the structure of the reciprocal lattice and independent of the position r_i if the solid is in an unloaded equilibrium state. The phase ϕ_{G_j} has a basic value $\phi^0_{G_j}$, indicating that the atoms are at their equilibrium positions. If the atoms are displaced from their equilibrium positions by u_j due to mechanical loading or thermal motion, the phase angle is modified as follows:

$$\phi_{G_j} = \phi^0_{G_j} + G_j u_j. \tag{2.46}$$

The same mathematic description as for "perfect" crystals is adopted for QCs, however, in a hyperspace due to the additional basis vectors. The corresponding reciprocal lattice in QCs remains periodic in the hyperspace, being indicated as G_J [12]. The dimensions of the hyperspace can be divided into two parts, the physical reciprocal space identified by a superscript $\parallel$ and the mathematical or complementary space by

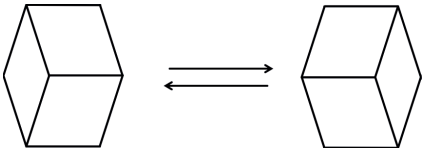

Figure 2.13.: A schematic illustration of the phason flip in a planar unit pattern. Each vertex represents the position of an atom. The unit pattern has two stable states, where the center atom can be switched between two different equilibrium positions.

$\perp$. So Eq. (2.46) is extended in the hyperspace as

$$\phi_{G_J} = \phi^0_{G_J} + G^{\parallel}_j u^{\parallel}_j + G^{\perp}_j u^{\perp}_j. \tag{2.47}$$

Here, the index in the physical space runs from 1 to 3 and in the complementary space from 1 to d, indicating a general $(3+d)$-dimensional hyperspace or reciprocal lattice with d being the number of the additional basis vectors. However, the mass density function describes the distribution of mass only in the physical space, i.e.

$$\rho(r^{\parallel}_i) = \sum_{G_J} \rho(G_J) \exp\{i G^{\parallel}_j r^{\parallel}_j\}. \tag{2.48}$$

Therefore, inserting the magnitude and the phase angle according to Eqs. (2.45) and (2.47) into Eq. (2.48), the mass density function for QCs is obtained as

$$\rho(r^{\parallel}_i) = \sum_{G_J} \rho_{G_J} \exp\{i G^{\parallel}_j r^{\parallel}_j + i\phi^0_{G_J} + i G^{\parallel}_j u^{\parallel}_j + i G^{\perp}_j u^{\perp}_j\}. \tag{2.49}$$

The total displacement $u_J = (u^{\parallel}_j, u^{\perp}_j)$ in the hyperspace indicates a shift with respect to an equilibrium position. In the physical space $u^{\parallel}$ corresponds to the real atomic displacement and is called phonon displacement. The term phonon is borrowed from quantum mechanics, which is a collective excitation in a periodic, elastic arrangement, describing the motion in a lattice [174]. Its counterpart $u^{\perp}$ in the complementary space is a motion in the hyperspace, eventually influencing the mass density function $\rho(r^{\parallel}_i)$ by changing the phase ϕ_{G_J}. It introduces a new degree of freedom in the elasticity of QCs, denoted as phason displacement. While a phonon displacement is related to translation of atoms, a phason displacement is associated with rearrangement of atomic sequences, locally manifested as a flip, where an atom shifts from one position to another one as the result of thermodynamic equilibrium, see Fig. 2.13. The phason flip can be observed by using high resolution transmission electron microscopy, e.g., a single atom flip by heating and cooling processes [46] and rearrangement of the sequence during growth [142]. Details about the phason field and its physical interpretation can be found in diverse review papers [32, 182].

A simple paradigm of a hyperspace with quasiperiodic structure in the physical dimen-

sion is illustrated in Fig. 2.14, intuitively demonstrating the phason displacement as a special elementary excitation in the higher dimensional space. The two-dimensional hyperspace consists of one physical dimension $\vec{e}^{\parallel}$ and one complementary dimension $\vec{e}^{\perp}$. A so-called cut method or projection method applied to the hyperspace is introduced as a common tool for obtaining a quasicrystalline structure in the physical dimension [12]. This method is not a straightforward structural analysis, however, many mathematical researches show that the hyperspace approach works well for QCs [186]. The periodic pattern, represented by the dots and projected onto the physical dimension $\vec{e}^{\parallel}$, builds a quasiperiodic arrangement with different distances conforming to the Fibonacci series, if the angle between $\vec{e}^{\parallel}$ and the periodic direction is irrational. The projected sequence, in which the segments are labeled by "S" for short distance and "L" for long distance, is a typical arrangement in QCs and has been proven by observations in [59, 142]. The projection in black describes the initial state of a quasiperiodic sequence and the red projection sequence is the result when a phason strain w is applied, which is defined as

$$w = \frac{\partial u^{\perp}}{\partial x^{\parallel}}, \tag{2.50}$$

where $x^{\parallel}$ is the coordinate of the physical dimension and $u^{\perp}$ is the phason displacement in the direction $\vec{e}^{\perp}$. The applied phason strain in the model of Fig. 2.14 is constant and interpreted as a rotation φ of the sampling stripe from the initial state. Comparing to the initial black sequence, the distances (S and L) in the red sequence keep their lengths, however, the arrangement is changed. Accordingly, the phason flips take place by the exchange of local combinations like SL$\longleftrightarrow$LS.

From the point of view of dynamics in QCs, different models have been introduced distinguished by the explanation of the motion in the phason field. One argument, called elastodynamics, is that the phason mode represents structural disorder. Thus, the equation of the phason motion is of wave type like the phonon field and both fields have the same mass density [12, 87]. In another assumption termed hydrodynamics [130], the dynamics of phason represents a type of diffusion with large diffusion time. In combination of the elastodynamics and hydrodynamics of QCs, two midway models have been proposed. The elasto-hydrodynamic model takes a wave type phonon field and a diffusive phason field [53]. In the other model, the elastodynamic model is of wave-telegraph type, whereas the phason field is represented by waves damped in time and propagating with finite velocity [7]. However, the physical meaning of the phason field in QCs is conclusive and there is no difference between the arguments in static problems.

2.3.3. State variables and linear constitutive relations

Since the phonon and phason are two kinds of elastic degrees of freedom in QCs, a generalized theory of elasticity is formulated [31, 123]. The phason strain, introduced

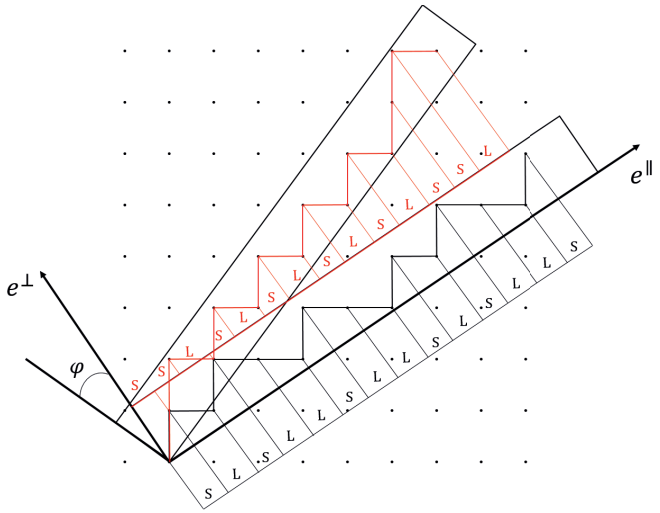

Figure 2.14.: Cut method to construct a quasiperiodic arrangement in the physical space from a periodic arrangement in a two-dimensional hyperspace. The phason strain in this case is interpreted as a rotation φ of the sampling stripe from its initial state and the phason flips of SL sequences are induced.

in Eq. (2.50), is given as a second-order tensor

$$w_{ij} = \frac{\partial W_i}{\partial x_j} \tag{2.51}$$

for a general three-dimensional problem, where W_i, as a generalization of $u_i^{\perp}$, is the displacement vector in the phason field and x_j are the coordinates in the physical space. Since the indices of W_i and x_j are allocated to different spaces, the phason strain isn't symmetric by nature:

$$w_{ij} \neq w_{ji}. \tag{2.52}$$

The elastic free energy density of QCs, given as a function of the phonon and phason strains [35], can be expanded into a Taylor series. Assuming infinitesimal displacement and neglecting higher order terms, the energy density $\Phi(\varepsilon_{ij}, w_{ij})$ consists of three terms:

$$\begin{aligned} \Phi(\varepsilon_{ij}, w_{ij}) &= \Phi_{uu} + \Phi_{ww} + \Phi_{uw} \\ &= \frac{1}{2} C_{ijkl}\varepsilon_{ij}\varepsilon_{kl} + \frac{1}{2} K_{ijkl} w_{ij} w_{kl} + R_{ijkl}\varepsilon_{ij} w_{kl}, \end{aligned} \tag{2.53}$$

with Φ_{uu}, Φ_{ww} and Φ_{uw} being pure phonon, pure phason and coupling energies, respectively. C_{ijkl} is the phonon elastic stiffness tensor, K_{ijkl} is the stiffness tensor in

phason space and R_{ijkl} denotes the phonon–phason coupling tensor. Furthermore, the stiffness and coupling tensors can be expressed by means of partial derivatives, just as outlined in Eq. (2.37) for piezoelectric problems, i.e.,

$$\begin{aligned} C_{ijkl} &= \frac{\partial^2 \Phi}{\partial \varepsilon_{ij} \partial \varepsilon_{kl}}, \qquad & C_{ijkl} &= C_{klij} = C_{ijlk} = C_{jikl}, \\ K_{ijkl} &= \frac{\partial^2 \Phi}{\partial w_{ij} \partial w_{kl}}, \qquad & K_{ijkl} &= K_{klij}, \\ R_{ijkl} &= \frac{\partial^2 \Phi}{\partial \varepsilon_{ij} \partial w_{kl}}, \qquad & R_{ijkl} &= R_{jikl}. \end{aligned} \tag{2.54}$$

Eqs. (2.54) comprise all symmetry conditions of the constitutive tensors. In particular, K_{ijkl} and R_{ijkl} exhibit just one symmetric property each. Unlike C_{ijkl}, their indices are not completely exchangeable due to the absence of the symmetry property in the phason strain, see Eq. (2.52), and the affiliation of ε_{ij} and W_{ij} to dissimilar types of spaces, Schwarz's theorem thus not being applicable. Throughout this work, the first two indices of the coupling tensor R_{ijkl} will always be attributed to the phonon field and the last two to the phason field.

According to Eq. (2.53), the linear governing constitutive equations of QCs are obtained as

$$\begin{aligned} \sigma_{ij} &= \frac{\partial \Phi}{\partial \varepsilon_{ij}} = C_{ijkl}\varepsilon_{kl} + R_{ijkl} w_{kl}, \\ H_{ij} &= \frac{\partial \Phi}{\partial w_{ij}} = R_{klij}\varepsilon_{kl} + K_{ijkl} w_{kl}, \end{aligned} \tag{2.55}$$

where the stresses, following the order of Voigt's notation, can be expressed as follows:

$$\begin{aligned} \sigma_{ij} &= (\sigma_{11}\ \sigma_{22}\ \sigma_{33}\ \sigma_{23}\ \sigma_{31}\ \sigma_{12})^T, \\ H_{ij} &= (H_{11}\ H_{22}\ H_{33}\ H_{23}\ H_{31}\ H_{12}\ H_{32}\ H_{13}\ H_{21})^T. \end{aligned} \tag{2.56}$$

Similar to the phonon stress σ_{ij} and its traction $t_i = \sigma_{ji} n_j$, the corresponding phason terms, a second-order non-symmetric phason stress tensor H_{ij} and the phason traction $h_i = H_{ij} n_j$, are introduced in [35]. It has to be noted that the index i of the phason stresses H_{ij} and h_i is attributed to the complementary space, while the index j represents the directions in the physical space, corresponding to the respective indices of the phason strain in Eq. (2.51). Since the phason stress and traction do not have any physical interpretation within the classical mechanical sense, a boundary value problem can only be formulated in terms of pure phonon loading and traction-free phason boundaries. The local form of the angular momentum theorem provides the symmetry of the phonon stress tensor

$$\sigma_{ij} = \sigma_{ji}, \tag{2.57}$$

however, there is not a similar momentum equation in the complementary space. Thus, it is not possible to obtain the symmetry of the phason stress tensor.

2.3.4. 1D, 2D and 3D QCs

The QCs are categorized according to their basic structures into several subclasses, i.e., pentagonal (p-), octagonal (o-), decagonal (d-), dodecagonal (dd-) and icosahedral (i-) phases. Among of them, the structures in the p-, o-, d- and dd-phase QCs are quasiperiodic in two dimensions and periodic in the third one. Due to the two quasiperiodic directions the complementary space has two dimensions with regard to the hyperspace consideration, whereupon this class of QCs is called two-dimensional (2D) QC. The icosahedral phase QCs have three quasiperiodic directions and thus belong to three-dimensional (3D) QCs. The cubic phase, considered as a quasicrystalline system in some works, however, is mostly dealt with in the framework of incommensurately modulated structure, since it shows a crystalline point symmetry [187]. To date, no other phases than icosahedron and cube were found in 3D QCs. Most of the already discovered QCs are icosahedral three-dimensional and decagonal two-dimensional QCs, which have about 100 and 70 kinds of stable compounds, respectively.

Apparently, 1D QCs are the ones that have a periodic plane and only one quasicrystalline axis (QA) being perpendicular to the periodic plane. Based on the points group theory, the 1D QCs have different phases, i.e., triclinic, monoclinic, orthorhombic, tetragonal, rhombohedra and hexagonal phases. However, they present the conventional crystalline symmetry in diffraction patterns [202]. In crystallographic analysis, 1D QCs with such phases can be theoretically deduced and explained by the hyperspace method, whereas in reality, 1D quasicrystalline samples cannot be distinguished from decagonal 2D QCs due to the limited resolution of observation techniques and thus have not been experimentally confirmed. Nevertheless, many stable QCs, believed with one-dimensional quasicrystalline structures, have been reported [198, 214] and observed [107]. They are transformed from 2D d-QCs after prolonged annealing.

Assuming the x_2-axis is the QA, 1D hexagonal QCs are transversely isotropic where the x_2-axis is also the axis of symmetry. Since there is only one phason degree of freedom, designated as W_2, the corresponding phason stresses and strains are

$$\begin{aligned} H_{ij} &= H_{2j} = (H_{22}\, H_{23}\, H_{21})^T, \\ w_{ij} &= w_{2j} = (w_{22}\, w_{23}\, w_{21})^T. \end{aligned} \tag{2.58}$$

According to Eq. (2.55), the material coefficient tensors written in compact general-

ized Voigt notation and matrix form, respectively, are given as follows:

$$\begin{pmatrix} \underline{C} & \underline{R} \\ \underline{R}^T & \underline{K} \end{pmatrix} = \begin{pmatrix} C_{1111} & C_{1122} & C_{1133} & 0 & 0 & 0 & R_1 & 0 & 0 \\ C_{1122} & C_{2222} & C_{1122} & 0 & 0 & 0 & R_2 & 0 & 0 \\ C_{1133} & C_{1122} & C_{1111} & 0 & 0 & 0 & R_1 & 0 & 0 \\ 0 & 0 & 0 & C_{1212} & 0 & 0 & 0 & R_3 & 0 \\ 0 & 0 & 0 & 0 & C_{1313} & 0 & 0 & 0 & 0 \\ 0 & 0 & 0 & 0 & 0 & C_{1212} & 0 & 0 & R_3 \\ R_1 & R_2 & R_1 & 0 & 0 & 0 & K_1 & 0 & 0 \\ 0 & 0 & 0 & R_3 & 0 & 0 & 0 & K_2 & 0 \\ 0 & 0 & 0 & 0 & 0 & R_3 & 0 & 0 & K_2 \end{pmatrix}, \quad (2.59)$$

where

$$\begin{aligned} C_{1313} &= \frac{C_{1111} - C_{1133}}{2}, \\ R_1 &= R_{1122} = R_{3322}, \quad R_2 = R_{2222}, \quad R_3 = R_{2323} = R_{1221}, \\ K_1 &= K_{2222}, \quad K_2 = K_{2323} = K_{2121}. \end{aligned}$$

Accordingly, there are five independent constants in the phonon elastic stiffness tensor, two in the phason stiffness tensor and three in the phonon–phason coupling tensor, respectively.

If a planar problem is taken into account and the x_1-x_2 plane is considered in the plane stress condition, as introduced in Section 2.1.5, some of the material constants have to be transformed as follows

$$\begin{aligned} &C^s_{1111} = C_{1111} - \frac{C_{1133}C_{1133}}{C_{1111}}, \quad C^s_{1122} = C_{1122} - \frac{C_{1122}C_{1133}}{C_{1111}}, \quad C^s_{2222} = C_{2222} - \frac{C_{1122}C_{1122}}{C_{1111}}, \\ &C^s_{1212} = C_{1212}, \\ &R^s_1 = R_1 - \frac{C_{1133}R_1}{C_{1111}}, \quad R^s_2 = R_2 - \frac{C_{1122}R_1}{C_{1111}}, \quad R^s_3 = R_3, \\ &K^s_1 = K_1 - \frac{R_1R_1}{C_{1111}}, \quad K^s_2 = K_2. \end{aligned} \quad (2.60)$$

The major class of 2D QCs, decagonal QCs, were considered as isotropic materials in the phonon field [35]. However, they exhibit transverse isotropy in experiments [27]. Taking the phason strain in the order as follows

$$w_{ij} = (w_{1j}\, w_{2j})^T = (w_{11}\, w_{12}\, w_{13}\, w_{21}\, w_{22}\, w_{23})^T \quad (2.61)$$

with the x_3-axis as the symmetry axis and the x_1-x_2-plane as the quasiperiodic plane,

the phason elastic tensor and the phonon–phason coupling tensor are represented by

$$\underline{K} = \begin{pmatrix} K_1 & 0 & 0 & 0 & K_2 & 0 \\ 0 & K_1 & 0 & -K_2 & 0 & 0 \\ 0 & 0 & 0 & 0 & 0 & 0 \\ 0 & -K_2 & 0 & K_1 & 0 & 0 \\ K_2 & 0 & 0 & 0 & K_1 & 0 \\ 0 & 0 & 0 & 0 & 0 & 0 \end{pmatrix} \tag{2.62}$$

and

$$\underline{R} = \begin{pmatrix} R_1 & R_2 & 0 & -R_2 & R_1 & 0 \\ -R_1 & -R_2 & 0 & R_2 & -R_1 & 0 \\ 0 & 0 & 0 & 0 & 0 & 0 \\ 0 & 0 & 0 & 0 & 0 & 0 \\ 0 & 0 & 0 & 0 & 0 & 0 \\ R_2 & -R_1 & 0 & R_1 & R_2 & 0 \end{pmatrix}. \tag{2.63}$$

There are two independent constants in K_{ijkl} and R_{ijkl}. The phonon elastic tensor takes the same form as shown in Eq. (2.18).

The phase of the most discovered stable/metastable QCs in all quasicrystalline categories is icosahedron. Because of the asymmetric property of w_{ij} and three quasiperiodic directions in i-QCs, there are nine coordinates in the phason field vectors. If the strain coordinates in w_{ij} are arranged in Voigt's notation as follows

$$w_{ij} = (w_{11}\ w_{22}\ w_{33}\ w_{23}\ w_{31}\ w_{12}\ w_{32}\ w_{13}\ w_{21})^T, \tag{2.64}$$

the phason and phonon–phason coupling elastic coefficient tensors are expressed as

$$\underline{K} = \begin{pmatrix} K_1 & 0 & 0 & 0 & K_2 & 0 & 0 & K_2 & 0 \\ 0 & K_1 & 0 & 0 & -K_2 & 0 & 0 & K_2 & 0 \\ 0 & 0 & K_1+K_2 & 0 & 0 & 0 & 0 & 0 & 0 \\ 0 & 0 & 0 & K_1-K_2 & 0 & K_2 & 0 & 0 & -K_2 \\ K_2 & -K_2 & 0 & 0 & K_1-K_2 & 0 & 0 & 0 & 0 \\ 0 & 0 & 0 & K_2 & 0 & K_1 & -K_2 & 0 & 0 \\ 0 & 0 & 0 & 0 & 0 & -K_2 & K_1-K_2 & 0 & -K_2 \\ K_2 & K_2 & 0 & 0 & 0 & 0 & 0 & K_1-K_2 & 0 \\ 0 & 0 & 0 & -K_2 & 0 & 0 & -K_2 & 0 & K_1 \end{pmatrix} \tag{2.65}$$

and

$$\underline{R} = R \begin{pmatrix} 1 & 1 & 1 & 0 & 0 & 0 & 0 & 1 & 0 \\ -1 & -1 & 1 & 0 & 0 & 0 & 0 & -1 & 0 \\ 0 & 0 & -2 & 0 & 0 & 0 & 0 & 0 & 0 \\ 0 & 0 & 0 & 0 & 0 & -1 & 1 & 0 & -1 \\ 1 & -1 & 0 & 0 & 1 & 0 & 0 & 0 & 0 \\ 0 & 0 & 0 & -1 & 0 & -1 & 0 & 0 & 1 \end{pmatrix} \tag{2.66}$$

with two independent coefficients in K_{ijkl} and only one in R_{ijkl}. The phonon elastic field of an i-QC is generally accepted as isotropic in crystallographic analyses and can thus be obtained from Eq. (2.16). The isotropic behavior has been derived from the quasicrystalline structure and further confirmed by experiments [173]. Nevertheless, some other experimental results indicate anisotropy in i-QCs, e.g., [44].

Due to the different phases in QCs, the occupancy of the material coefficients in K_{ijkl} and R_{ijkl} shows different forms. In this work, Eqs. (2.59), (2.62), (2.63), (2.65) and (2.66) are introduced and only hold for 1D hexagonal QCs, 2D decagonal QCs and 3D icosahedral QCs, respectively. More data for other possible phases can be found in [35] and [50].

2.3.5. Constitutive equations of piezoelectric QCs

As introduced previously, QCs have various physical properties in addition to the intrinsic phonon–phason coupling effect. Generally, the constitutive behavior of QCs and the material constants including physical properties have been theoretically derived from thermodynamic equilibrium, e.g., QCs with piezoelectricity. Based on the point group symmetry of QCs, the piezoelectricity and the electric permittivity in different phases of QCs can be determined [78, 87]. Independently, the piezoelectricity was also predicted by the hyperspace theory [97]. In these analyses, the piezoelectric tensor e_{ijk} and the dielectric tensor κ_{kl} take the same forms as those in Eqs. (2.42) and (2.43). However, the piezoelectric effect is absent in 3D i-QCs.

Although the piezoelectric effect in QCs has been deduced from the point of view of crystallography, no measurement has been reported. The reason is that QCs have been found only in some kinds of material systems, e.g., Al-base alloys. None of them exhibits the piezoelectric effect. A few years ago, a series of experiments suggested that barium titanate deposited on a platinum substrate can form a quasicrystalline structure under high temperature conditions, being the first quasicrystalline structure in oxide [62]. Such oxidic QC based on the classic ferroelectric material BT has been investigated and observed by using scanning tunneling microscopy and other experimental techniques, showing a dodecagonal phase [28,219]. However, it still remains an open question whether the quasicrystalline film of BT has the same electromechanical behavior as the ordinary BT ceramic. Further experiments to investigate piezoelectric/ferroelectric properties in QCs are still expected.

If the BT QC is considered taking the piezoelectric properties of crystalline BT into account, the generalized electric enthalpy density, containing the terms from the phonon, phason and electric fields, can be expressed by

$$\begin{aligned}\Pi(\varepsilon_{ij}, w_{ij}, E_i) &= \frac{1}{2}\sigma_{ij}\varepsilon_{ij} + \frac{1}{2}H_{ij}w_{ij} - \frac{1}{2}E_iD_i \\ &= \frac{1}{2}C_{ijkl}\varepsilon_{ij}\varepsilon_{kl} + R_{ijkl}\varepsilon_{ij}w_{kl} + \frac{1}{2}K_{ijkl}w_{ij}w_{kl} - e_{ijk}E_k\varepsilon_{ij} - \frac{1}{2}\kappa_{ik}E_iE_k,\end{aligned} \tag{2.67}$$

fusing Eqs. (2.32) and (2.53). The extended constitutive system of equations is thus obtained as

$$\begin{aligned}\sigma_{ij} &= C_{ijkl}\varepsilon_{kl} + R_{ijkl}w_{kl} - e_{ijk}E_k, \\ H_{ij} &= R_{klij}\varepsilon_{kl} + K_{ijkl}w_{kl}, \\ D_i &= e_{kli}\varepsilon_{kl} + \kappa_{ik}E_k,\end{aligned} \tag{2.68}$$

where the material coefficient tensors have been introduced in Eqs. (2.37) and (2.54). The direct coupling between the electric field and the phason field has not been reported yet, therefore, it is absent in the constitutive equations.

3. Linear elastic fracture mechanics in piezoelectric QCs

Material or structure failure is in the focus of interest, especially in the fields of structural design and manufacturing. A failure can be caused by preexistent flaws, damage/crack initiation due to overloading, fatigue, or other factors. Classical fracture mechanics has been studied in these aspects since it was established in the 1920s by Griffith, who investigated the propagation of brittle cracks in glass [77, 95]. Motivated by industrial applications of structural materials, numerous assessments in classical fracture mechanics have been developed since, e.g., crack growth and deflection criteria.

Due to electro–elastic and phonon–phason coupling effects, fracture mechanical theories are modified for piezoelectrics and QCs, however, incorporating their inherent characteristics. Fracture mechanics research in piezoelectrics started in the late 1970s. In the pioneering works, the integral transformation method was used to solve the crack problem with pure mechanical loading [154]. A distributed dislocations method was described [33] for the study of piezoelectric media with cracks based on an extended Stroh-formalism proposed by Barnett [14]. Later, the solutions in the near tip field were reported in [147, 152, 192]. Another approach, using a complex potential method, was suggested specifically for anisotropic materials in [122] and extended to piezoelectrics for offering a solution of field quantities [146, 183]. A comprehensive introduction of the mathematical fundamentals of these analysis methods can be found in [195]. Based on the analytical solutions, the fracture loading quantities and the corresponding fracture criteria for piezoelectric materials have been studied and discussed [55, 114]. For example, the classical intensity factors concept is extended to piezoelectrics based on the $1/\sqrt{r}$-singularity of the electric displacement at the crack tip [184] and the factors were modified due to the boundary conditions of crack faces [73], the J-integral was generalized for piezoelectrics [5, 164] and the mechanical energy release rate criterion as a fracture parameter was proposed [153].

There are also a lot of references, dealing with different problems in the extended theory of elasticity and fracture mechanics in QCs. Various boundary value problems have been investigated by applying the methods that are often used in piezoelectrics, providing solutions for, e.g., inclusions [69, 177], interfaces [203] and Green's functions [68, 149]. Some papers address crack problems in QCs, providing fracture mechanical loading quantities and the closed-form solutions in the crack tip near field by using the complex analysis method with conformal mapping [70, 125] or the Fourier transformation [218]. One of the first rigorous derivations of the J-integral of QC is found in [206], where also the energy release rate and the crack closure integral are

introduced. The nonlinearity of QCs and dynamic fracture were investigated in [52]. The crack growth problem and the deflection in QCs were handled within a continuum mechanical framework, investigating the influence of the phonon–phason coupling effect on crack growth behavior [206]. A classical FEM for QC crack problems has been developed in [213], a meshless local Petrov-Galerkin approach is applied to dynamic crack problems in QCs in [179]. A first numerical work on crack growth simulation in QC based on the FEM is published in [204]. Another interesting work, focusing on crack propagation mechanism in QCs, was carried out at the atomic/molecular level [137].

In the following sections, discussions and solutions are restricted to crack problems in the context of fracture mechanics. Since piezoelectric ceramics and quasicrystalline materials are predominantly brittle at room temperature, the plastic deformation is sufficiently small compared to the crack size and can be limited to a small inelastic zone in front of a crack tip, the fracture process zone. Under this assumption, crack problems in piezoelectric QCs are mathematically analyzed within the framework of generalized linear elasticity.

3.1. Stroh formalism and near-tip field solutions

If a single narrow crack in a planar problem is taken into account, where the crack length is much greater than the crack opening, stress and displacement fields can be obtained by considering an elliptical hole with an infinitesimal height. Although the constitutive behavior in anisotropic materials is more complex than in isotropic materials, leading to difficulties in this solution scheme applied in piezoelectric QCs, the elegant closed-form solution of an elliptical hole in anisotropic materials is provided in two formalisms. The Stroh formalism begins with the displacement field and is stated in terms of elastic stiffness [188, 189], while the Lekhnitskii formalism begins with stresses and is based on compliance [122]. The solutions in these two formalisms are essentially equivalent. Thus, in this work only the solution in the generalized Stroh formalism is implemented for piezoelectric QCs.

For the sake of compactness, generalized vectors and tensors with uppercase indices,

$$u_I = \begin{cases} u_I, & I = 1,2,3 \\ W_{(I-3)}, & I = 4,5,6\,, \\ \varphi, & I = 7 \end{cases} \qquad \sigma_{Ij} = \begin{cases} \sigma_{Ij}, & I = 1,2,3 \\ H_{(I-3)j}, & I = 4,5,6 \\ D_j, & I = 7 \end{cases} \tag{3.1}$$

and

$$C_{IjKl} = \begin{pmatrix} C_{ijkl} & R_{ijkl} & e_{ijl} \\ R_{klij} & K_{ijkl} & 0 \\ e_{lij} & 0 & -\kappa_{jl} \end{pmatrix}, \quad C_{IjKl} = \begin{cases} C_{IjKl}, & I,K = 1,2,3 \\ R_{Ij(K-3)l}, & I = 1,2,3; K = 4,5,6 \\ R_{Kl(I-3)j}, & I = 4,5,6; K = 1,2,3 \\ K_{(I-3)j(K-3)l}, & I,K = 4,5,6 \\ e_{Ijl} \text{ or } e_{lIj}, & I = 1,2,3; K = 7 \\ \kappa_{jl}, & I,K = 7 \end{cases}, \tag{3.2}$$

are introduced, which contain the independent and associated variables as well as the material coefficients of a general 3D piezoelectric QC problem. The uppercase indices range from 1 to 7, where $I = 1,2,3$ indicate the phonon field, $I = 4,5,6$ the phason field and $I = 7$ the electric field, respectively. In the following, a 1D QC planar problem is considered in the derivation of a general solution, thus, the uppercase index runs from 1 to 4, having two degrees of freedom in the phonon field, one in the phason and one in the electric field. The phason displacement and stress in this case are degenerated into scalar and vector quantities, respectively.

In comparison to the strain and the displacement gradient, the electric field E_i is the negative electric potential gradient

$$E_i = -\frac{\partial \varphi}{\partial x_i}, \tag{3.3}$$

thus changing the signs of e_{ijk} and κ_{kl} in C_{IjKl} compared to Eq. (2.68).

If a piezoelectric QC is considered without body forces and free electric charges, the constitutive equations and the static balance equations of momentum and charge are given as follows

$$\sigma_{Ij} = C_{IjKl}\, u_{K,l}, \tag{3.4}$$

$$C_{IjKl}\, u_{K,lj} = 0. \tag{3.5}$$

Hence, the state variables are only related to the coordinates (x_1, x_2) and the solution of Eq. (3.5) is assumed to have the form

$$u_K = a_K f(z), \qquad z = x_1 + p x_2, \tag{3.6}$$

where f is an arbitrary holomorphic function of z and p and a_K are unknown quantities to be determined subsequently. The origin of the x_i coordinate system is at the center of the crack/elliptical hole, see Fig. 3.1. Differentiating Eq. (3.6)

$$\begin{aligned} u_{K,1} &= a_K \frac{\partial f(z)}{\partial x_1} = a_K f'(z) \\ u_{K,2} &= a_K \frac{\partial f(z)}{\partial x_2} = a_K p f'(z) \end{aligned} \tag{3.7}$$

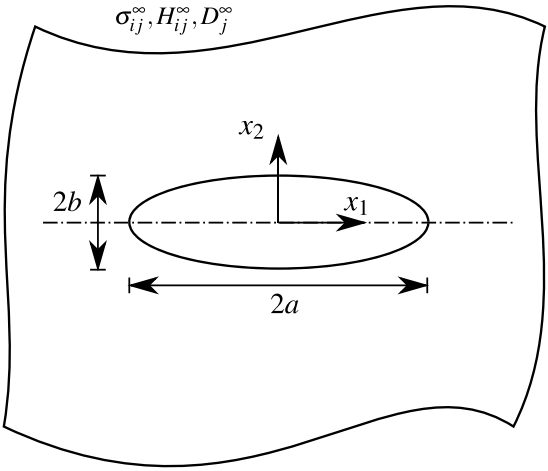

Figure 3.1.: Elliptical hole or crack $(b \to 0)$ in an infinite domain with the remote uniform loads σ_{Ij}^{∞}.

and substituting into Eq. (3.5) yields

$$C_{IjKl}(\delta_{l1} + p\,\delta_{l2})(\delta_{j1} + p\,\delta_{j2})a_K f''(z) = 0, \tag{3.8}$$

where the prime denotes the derivative with respect to z. Since f is an arbitrary function, $f''(z)$ is in general nonzero and can be eliminated, leading to

$$\{C_{I1K1} + (C_{I1K2} + C_{I2K1})p + C_{I2K2}p^2\}a_K = 0, \tag{3.9}$$

where the three coefficients of the polynomial, $C_{I1K2} + C_{I2K1}$, C_{I1K1} and C_{I2K2} are three 4×4 matrices. The latter two coefficients are symmetric and positive definite for classic materials and QCs. In the case of materials with piezoelectric property, they are not positive definite because the dielectric constants in C_{IjKl} have a negative sign. Physically, the nonexistent positive definiteness of piezoelectric problem provides the option of a negative stored potential energy.

Inherently, Eq. (3.9) is a quadratic eigenvalue problem for a non-trivial solution of a_K. The determinant of the term in braces is an eighth-power polynomial in p, therefore four pairs of conjugate complex eigenvalues are obtained and the same holds for the eigenvectors a_K. Introducing complex conjugates with a bar, the eigenvalues and -vectors have the following relations

$$\Im\{p^\alpha\} > 0, \qquad p^{\alpha+4} = \bar{p}^\alpha, \qquad a_K^{\alpha+4} = \bar{a}_K^\alpha \qquad (\alpha = 1,2,3,4), \tag{3.10}$$

where $\Im$ indicates the imaginary part of the term in the curly braces. Each eigenvalue p^α provides an associated solution $a_K^\alpha f^\alpha(z^\alpha)$. The superscript index α is temporarily used here, since the subscript place is occupied. Assuming that the eigenvalues are

distinct, the general solution of displacements u_K according to Eq. (3.6) is obtained by superposing eight independent solutions

$$u_K = \sum_{\alpha=1}^{4} \{a_K^\alpha f^\alpha(z^\alpha) + \bar{a}_K^\alpha \bar{f}^\alpha(\bar{z}^\alpha)\}. \tag{3.11}$$

Introducing a matrix and a vector according to

$$A_{IJ} = a_I^{\alpha=J} \quad \text{and} \quad f_J = f^{\alpha=J}(x_1 + p^{\alpha=J} x_2) \tag{3.12}$$

to formally replace the summation in Eq. (3.11), the generalized displacements in a plane problem are obtained as

$$u_I = A_{IJ} f_J + \overline{A}_{IJ} \bar{f}_J. \tag{3.13}$$

Substituting Eq. (3.6) into Eq. (3.4), the generalized stresses are obtained as

$$\sigma_{Ij} = (C_{IjK1} + p\, C_{IjK2}) a_K f'(z), \tag{3.14}$$

and the stress tensor coordinates are given as

$$\begin{aligned} \sigma_{I1} &= (C_{I1K1} + p\, C_{I1K2})\, a_K f'(z), \\ \sigma_{I2} &= (C_{I2K1} + p\, C_{I2K2})\, a_K f'(z). \end{aligned} \tag{3.15}$$

Another vector b_I is introduced as

$$b_I = (C_{I2K1} + p\, C_{I2K2})\, a_K = -\frac{1}{p}(C_{I1K1} + p\, C_{I1K2})\, a_K, \tag{3.16}$$

whereat the second identity is derived from Eq. (3.9). Thus, the stress tensor coordinates in Eq. (3.15) can be represented as partial differentials of $f(z)$ as follows

$$\begin{aligned} \sigma_{I1} &= -b_I \frac{\partial f(z)}{\partial x_2} = -\frac{\partial \phi_I}{\partial x_2}, \\ \sigma_{I2} &= b_I \frac{\partial f(z)}{\partial x_1} = \frac{\partial \phi_I}{\partial x_1}, \end{aligned} \tag{3.17}$$

where $\phi_I = b_I f(z)$ is the stress function vector. Analogous to A_{IJ} for the displacements, a matrix B_{IJ} is constructed as

$$B_{IJ} = b_I^{\alpha=J}, \tag{3.18}$$

and the stress function vector is finally given as

$$\phi_I = B_{IJ} f_J + \bar{B}_{IJ} \bar{f}_J. \tag{3.19}$$

In most applications, the unknown functions f_J for different eigenvalues, see Eq. (3.12),

exhibit the same structure [195], leading to

$$f_J = f(x_1 + p^{\alpha=J} x_2). \tag{3.20}$$

They are determined adapting Eqs. (3.13) and (3.19) to individual boundary conditions. It should be noted that the eigenvalues p^α and the matrices A_{IJ} and B_{IJ} depend exclusively on the properties of the material and are thus denoted as characteristic eigenvalues and matrices in this work. In transversally isotropic materials with the x_3-axis as symmetry axis, which is perpendicular to the isotropic plane and represents the poling direction and the QA in piezoelectric QCs, the solution of Eq. (3.9) has a multiple eigenvalue $p^\alpha = \sqrt{-1} = i$ and the depicted solutions are therefore invalid. Such problems are referred to as degenerate problems and a solution in terms of the Stroh formalism can also be achieved, however, requiring a special mathematical treatment [162, 195].

Since the phason stress is introduced for completing the thermodynamic description, having no physical interpretation in a structural mechanics sense, it cannot be applied like a mechanical or electric loading. The phason load H_j^∞ is thus always zero, considering e.g. a crack in an infinitely large anisotropic plate with the remote uniform loads σ_{Ij}^∞. The boundary conditions are

$$\begin{cases} \sigma_{Ij}(z) = \sigma_{Ij}^\infty, \quad |z| \to \infty, \\ \phi_I(z) = \text{constant}, \quad z \text{ at the ellipse boundary}, \end{cases} \tag{3.21}$$

where the stress potentials ϕ_I at the ellipse boundary are usually set to zero without loss in generality.

The boundary conditions hold for cracks and holes likewise. In [89] an elliptical hole with semiaxes a and b ($a > b$), see Fig. 3.1, is considered to obtain a general solution for this specific boundary value problem. Applying the conformal mapping method, the infinite plane described by $z_K = x_1 + p_K x_2$ and exhibiting distinct eigenvalues p_K, is mapped onto a complex plane, yielding

$$f_I(\zeta_I) = -\frac{1}{2} \zeta_{IJ}^* B_{JK}^{-1} (a\sigma_{K2}^\infty - ib\sigma_{K1}^\infty) \tag{3.22}$$

with

$$\begin{aligned} \zeta_{IJ}^* &= \begin{cases} 1/\zeta_I, & \text{if } I = J \\ 0, & \text{if } I \neq J \end{cases}, \\ \frac{1}{\zeta_I} &= \frac{z_I - \sqrt{z_I^2 - a^2 - p_I^2 b}}{a + i p_I b}. \end{aligned} \tag{3.23}$$

The detailed derivation of the general solution Eq. (3.22) and the conformal mapping method can be found in [89]. Setting the height of the elliptical hole b to zero, Eq. (3.22) then holds for a crack problem with remote loadings. The final formulations of the generalized stress and strain fields are obtained by substituting Eq. (3.22) into Eqs.

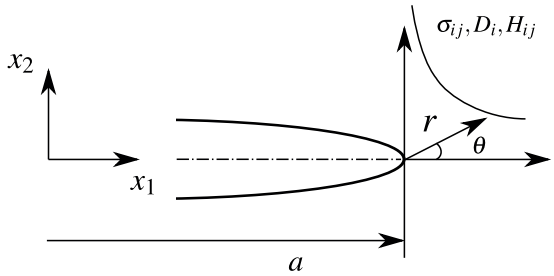

Figure 3.2.: Polar coordinates (r,θ) in the vicinity of a crack tip and the singular field quantities σ_{ij}, D_i, H_{ij} on the ligament.

(3.6) and (3.19) and using Eq. (3.17):

$$\begin{aligned}
\sigma_{I1} &= \Re\left\{B_{IM}\, P^{\mathrm{S1}}_{MN}\, B^{-1}_{NJ}\right\}\sigma^{\infty}_{J2} + \sigma^{\infty}_{I1},\\
\sigma_{I2} &= \Re\left\{B_{IM}\, P^{\mathrm{S2}}_{MN}\, B^{-1}_{NJ}\right\}\sigma^{\infty}_{J2},\\
u_I &= \Re\left\{A_{IM}\, P^{\mathrm{u}}_{MN}\, B^{-1}_{NJ}\right\}\sigma^{\infty}_{J2},
\end{aligned} \tag{3.24}$$

where $\Re$ denotes the real part of a complex quantity in curly braces. P^{S1}_{MN}, P^{S2}_{MN} and P^{u}_{MN} are 4×4 diagonal matrices given as follows

$$\begin{aligned}
P^{\mathrm{S1}}_{MN} &= \mathrm{diag}\left(p_K - \frac{z_K p_K}{\sqrt{z_K^2 - a^2}}\right),\\
P^{\mathrm{S2}}_{MN} &= \mathrm{diag}\left(\frac{z_K}{\sqrt{z_K^2 - a^2}}\right),\\
P^{\mathrm{u}}_{MN} &= \mathrm{diag}\left(\sqrt{z_K^2 - a^2} - z_K\right).
\end{aligned} \tag{3.25}$$

The same boundary value problem can also be solved by applying the Fourier transformation, yielding the same solutions as those provided in Eq. (3.24). This basic solution scheme was introduced for anisotropic materials [188] and extended for piezoelectrics [152] and QCs [68].

Since the field quantities near the crack tip are of interest in fracture analysis, it is necessary to modify the formulations of the solutions. Within a polar coordinate system with the origin at the right crack tip, introduced in Fig. 3.2, the coordinate z in Eq. (3.6) is transformed into the polar coordinate system

$$z_K = a + r(\cos\theta + p_K \sin\theta). \tag{3.26}$$

In the vicinity of the crack tip, where r is much smaller than the crack length, the approximation $r/a \to 0$ is established. Inserting the approximation and Eq. (3.26) into Eqs. (3.24) and (3.25), the near-tip field solutions of the generalized stresses and

displacements for a crack are obtained as

$$\begin{aligned}
\sigma_{I1} &= -\sqrt{\frac{a}{2r}}\Re\left\{B_{IM}\,P^{\mathrm{S1}}_{MN}\,B^{-1}_{NJ}\right\}\sigma^{\infty}_{J2},\\
\sigma_{I2} &= \sqrt{\frac{a}{2r}}\Re\left\{B_{IM}\,P^{\mathrm{S2}}_{MN}\,B^{-1}_{NJ}\right\}\sigma^{\infty}_{J2},\\
u_I &= \sqrt{2ar}\,\Re\left\{A_{IM}\,P^{\mathrm{u}}_{MN}\,B^{-1}_{NJ}\right\}\sigma^{\infty}_{J2} - a\Re\left\{A_{IM}\,B^{-1}_{MJ}\right\}\sigma^{\infty}_{J2},
\end{aligned} \tag{3.27}$$

where P^{S1}_{MN}, P^{S2}_{MN} and P^{u}_{MN} are simplified from Eq. (3.25) as the functions of the eigenvalues and the polar coordinate angle θ:

$$\begin{aligned}
P^{\mathrm{S1}}_{MN} &= \mathrm{diag}\left(\frac{p_K}{\sqrt{\cos(\theta)+p_K\sin(\theta)}}\right),\\
P^{\mathrm{S2}}_{MN} &= \mathrm{diag}\left(\frac{1}{\sqrt{\cos(\theta)+p_K\sin(\theta)}}\right),\\
P^{\mathrm{u}}_{MN} &= \mathrm{diag}\left(\sqrt{\cos(\theta)+p_K\sin(\theta)}\right).
\end{aligned} \tag{3.28}$$

Eq. (3.27) indicates that the stresses σ_{I1} and σ_{I2} exhibit a $r^{-1/2}$-singularity near the crack tip at $z=\pm a$. Thus, the constant term σ^{∞}_{I1} in Eq. (3.24) disappears in the near-tip solution. The latter term of u_I in Eq. (3.27) represents the solutions of the displacement and electric potential fields in an infinite plane without any defect being subjected to the remote loading σ^{∞}_{J2}. It is therefore ignored in the near-field solutions, where only crack tip opening displacement is of concern.

3.2. Transformation of the characteristic matrices and the eigenvalues

The near-field solutions depend on the characteristic matrices and the eigenvalues, which are direction-dependent in piezoelectric QCs due to anisotropic behavior in the plane. If a crack propagates, the crack tip might deflect and thus has a different local coordinate system compared to the global one. As a consequence, the near-tip solutions are changed and should be derived from the original solutions via the transformation process basically introduced in Section 2.1.3, where the referred coordinate system rotates as shown in Fig. 2.2. Within the given multifield context, however, the transformations have to be extended towards the complementary space and the electric degree of freedom. Furthermore, the matrices of the Stroh formalism must not be handled within the context of a dyadic tensor transformation.

See Fig. 3.3 for a 1D piezoelectric QC with the QA in the x_1-x_2-plane and the coordinates x_i rotating around the x_3-axis with an angle φ relative to $\hat{x}_i$. The 4×4 transfor-

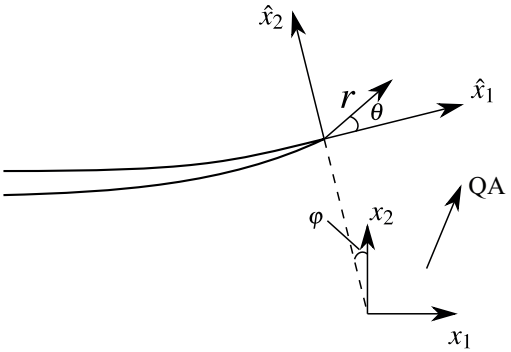

Figure 3.3.: Local coordinate system $\hat{x}_i$ at the tip of a deflected crack with an angle φ relative to the global coordinate system x_i.

mation matrix is defined as

$$\Omega_{IJ} = \begin{pmatrix} \Omega_{ij} & 0 \\ 0 & \delta_{ij} \end{pmatrix} \qquad \text{and} \qquad \Omega_{ij} = \begin{pmatrix} \cos\varphi & \sin\varphi \\ -\sin\varphi & \cos\varphi \end{pmatrix}, \tag{3.29}$$

considering two phonon, one phason and one electric degree of freedom. The diagonal components in Ω_{IJ} in terms of the electric and phason fields are 1 because the magnitudes of the electric potential and the phason displacements are not affected by the rotation of the coordinate system. The scalar product of unit vectors, similar to Eq. (2.11), from different fields, e.g., $\vec{e}_1$ in x_1 and $\vec{e}_4$ in the electric field, has no physical significance. Thus, the corresponding components in Ω_{IJ} are zero.

The generalized stress and elastic tensors in terms of phonon, phason and electric fields are transformed into the new reference coordinate system by

$$\hat{\sigma}_{Ij} = \Omega_{IM}\Omega_{jn}\sigma_{Mn} \tag{3.30}$$

and

$$\hat{C}_{IjKl} = \Omega_{IM}\Omega_{jn}\Omega_{KP}\Omega_{lq}C_{MnPq}. \tag{3.31}$$

Furthermore, the eigenvalues and the material-dependent characteristic matrices of the Stroh formalism in local coordinates $\hat{x}_i$ read

$$\begin{aligned} \hat{p}_K &= \frac{p_K\cos\varphi - \sin\varphi}{p_K\sin\varphi + \cos\varphi}, \\ \hat{A}_{IK} &= \Omega_{IJ}A_{JK}, \\ \hat{B}_{IK} &= \Omega_{IJ}B_{JK}, \end{aligned} \tag{3.32}$$

which enable the application of the general near-tip solutions in Eq. (3.27) to cracks in arbitrary directions. The extensive derivation of Eqs. (3.32) is given in Appendix B.

3.3. Fundamental concepts of multiphysical fracture mechanics

In the case of failure analyses, where only crack-induced failure is considered, assessments referring to various approaches have been developed. The first successful analysis was that of Griffith in the 1920s, who proposed an energy balance approach [77]. He claimed that crack propagation reduces the elastic strain energy of the system, which is required for creating new crack surfaces. Later, Irwin developed the energy release rate in the well-known form [90]. On the other hand, a stress intensity factor (SIF or K-factor) concept was proposed based on the singular stress fields in front of the crack tip and the relation between the K-factors and the energy release rate was derived [91]. In these analyses, a small-scale yielding assumption is introduced, which implies that the theoretical stress singularity generates a sufficiently small yield zone in a real material, thus having no effect on elastic solutions. Hence, the K-factors and the energy release rate are restricted to linear elastic fracture mechanics. In order to describe the movement of a singularity in an elastic body, such as defects and inhomogeneities, a driving force concept was developed in configurational space, either formulated locally or in terms of an integral of the energy momentum tensor along a closed contour [49]. If the path of integration contains a crack tip, the driving force coincides with the J-integral, which is defined as a dissipation rate with infinitesimal crack advance [157, 158]. The relation between the J-integral and the K-factors in linear elastic fracture mechanics was presented in the referenced work. Extensions of this relationship were elaborated towards piezoelectric fracture mechanics [5,146,148,192] and quasicrystals [50, 181, 206].

3.3.1. Generalized stress intensity factors

Characterization of near crack-tip stress fields or loading conditions is the basis of fracture mechanics. Nevertheless, according to Eq. (3.27) the near-tip field stresses exhibit an inverse square root singularity and thus the stresses are not appropriate for quantifying the loading condition at the crack tip. The asymptotic behavior of the generalized stress on the ligament approaching the crack tip, however, can be characterized by the K-factors, which are defined in linear elastic piezoelectric fracture mechanics of QCs for a general case with all possible degrees of freedom as

$$(K_{II}^{\parallel}, K_{I}^{\parallel}, K_{III}^{\parallel}, K_{II}^{\perp}, K_{I}^{\perp}, K_{III}^{\perp}, K_{IV})^T = \lim_{r\to 0} \sqrt{2\pi r}(\sigma_{12}, \sigma_{22}, \sigma_{32}, H_{12}, H_{22}, H_{32}, D_2)^T(\theta = 0). \tag{3.33}$$

The K-factors with the superscript $\parallel$ are conventional K-factors for classical structural materials describing three basic crack opening modes introduced by Irwin [91]. Each of the basic crack modes is primarily associated with single local crack face displacement as shown in Fig. 3.4 and any fracture condition in a cracked elastic body is identified by one of the three basic modes or their combinations. The superscript $\perp$ indicates that the $K^{\perp}$-factors are related to the phason field in QC. Compared to the $K^{\parallel}$-factors in the phonon field, the $K^{\perp}$-factors are not associated with any displacement in

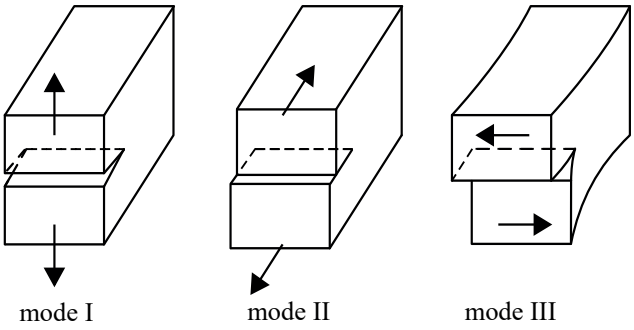

Figure 3.4.: Illustration of the three basic opening modes of a crack: the normal opening mode (mode I), the in-plane sliding mode (mode II) and the tearing mode (mode III).

the geometrical/Euclidean space, thus the subscripts of $K^{\perp}$ do not refer to any basic crack mode and are just arranged similar to the $K^{\parallel}$-factors. K_{IV} is an additional electric displacement intensity factor defined in accordance with the classical mechanical K-factors, representing the singular behavior of the electric displacement D_2 in front of the crack tip [192].

The K-factors are universal fracture parameters for arbitrary crack geometries and loading conditions, characterizing specifically the stress state at a crack tip. Thus, they are widely used in analyses of fracture mechanics. In general, the K-factors can be determined by various empirical formulae depending on the loading and the geometries of cracked structures, see [193].

For a Griffith crack, where a crack with a length of $2a$ is embedded in an infinite elastic plate subjected to remote tensile loading σ^{∞}_{I2}, the analytical solutions of the intensity factors are given as

$$(K^{\parallel}_{II}, K^{\parallel}_{I}, K^{\parallel}_{III}, K^{\perp}_{II}, K^{\perp}_{I}, K^{\perp}_{III}, K_{IV})^T = \sqrt{\pi a}(\sigma^{\infty}_{12}, \sigma^{\infty}_{22}, \sigma^{\infty}_{32}, H^{\infty}_{12}, H^{\infty}_{22}, H^{\infty}_{32}, D^{\infty}_{2})^T. \quad (3.34)$$

In a planar 1D quasicrystalline case, Eq. (3.34) is degenerated by neglecting $K^{\parallel}_{III}$ and two phason $K^{\perp}$-factors:

$$K_J = (K^{\parallel}_{II}, K^{\parallel}_{I}, K^{\perp}, K_{IV})^T. \quad (3.35)$$

Substituting Eq. (3.34) with the reduction of Eq. (3.35) into the general solutions Eq. (3.27), the near-tip field solutions are obtained as functions of the K-factors:

$$\begin{aligned} \sigma_{I1} &= -\frac{1}{\sqrt{2\pi r}}\Re\{B_{IM} P^{\mathrm{s1}}_{MN} B^{-1}_{NJ}\}K_J, \\ \sigma_{I2} &= \frac{1}{\sqrt{2\pi r}}\Re\{B_{IM} P^{\mathrm{s2}}_{MN} B^{-1}_{NJ}\}K_J, \\ u_I &= \sqrt{\frac{2r}{\pi}}\Re\{A_{IM} P^{\mathrm{u}}_{MN} B^{-1}_{NJ}\}K_J. \end{aligned} \quad (3.36)$$

Specifically, the stresses and displacements according to Eqs. (3.36) are represented by the K-factors, introducing loading and geometry, and angular functions, being uniquely defined for a class of materials, not depending on geometry or loading. In detail, the equations of near-tip multiphysical fields read

$$\begin{aligned} \sigma_{Ij} &= \frac{1}{\sqrt{2\pi r}} \left(\sum_{N=1}^{2} K_N^{\parallel} f_{Ij}^{\parallel N}(\theta) + K^{\perp} f_{Ij}^{\perp}(\theta) + K_{IV} f_{Ij}^{e}(\theta) \right), \\ u_I &= \sqrt{\frac{2r}{\pi}} \left(\sum_{N=1}^{2} K_N^{\parallel} d_I^{\parallel N}(\theta) + K^{\perp} d_I^{\perp}(\theta) + K_{IV} d_I^{e}(\theta) \right), \end{aligned} \tag{3.37}$$

where f_{Ij} are the angular functions of stresses and d_I those of the displacements, respectively. Comparing Eqs. (3.36) and (3.37), the generalized angular functions of piezoelectric QCs are given explicitly with the characteristic matrices as follows

$$\begin{aligned} f_{I1}^{J} &= -\Re\{B_{IM} P_{MN}^{\mathrm{s1}} B_{NJ}^{-1}\}, \\ f_{I2}^{J} &= \Re\{B_{IM} P_{MN}^{\mathrm{s2}} B_{NJ}^{-1}\}, \\ d_{I}^{J} &= \Re\{A_{IM} P_{MN}^{\mathrm{u}} B_{NJ}^{-1}\}. \end{aligned} \tag{3.38}$$

3.3.2. Generalized energy release rate and crack closure integral

The energy balance approach basically developed by Griffith [77], evolves from the postulate that the total energy E^{tot} of a dissipative system seeks a minimum. Within the framework of variational calculus, the condition of stationarity in terms of

$$\delta E^{tot} = 0 \tag{3.39}$$

has to be satisfied, where δ denotes the first variation with regard to the crack length or surface in a more general context.

The energy balance approach claims that the increased surface energy of crack growth is provided by the external potential energy associated with the applied forces and the strain energy stored in the deformed body. The total energy consists of the total potential energy U^{tot} and the fracture surface energy U^{f}:

$$E^{tot} = U^{tot} + U^{f}. \tag{3.40}$$

The total potential energy is given as

$$U^{tot} = U^{i} + U^{a} = U^{i} - W^{a} \tag{3.41}$$

with W^{a} as the work done by the external forces, U^{i} and U^{a} as the internal and external potential works. The surface energy for each crack face is $\gamma_s B \Delta a$, where γ_s is the required energy per unit area to create a new crack surface, B and Δa are the thickness and the length of the newly-formed crack surface, respectively. Thus the total energy

is

$$E^{tot} = U^{tot} + 2\gamma_s B\Delta a. \tag{3.42}$$

Accounting for Eq. (3.39), equilibrium in the dissipative system of an elastic medium with a crack, exposed to external loads, finally satisfies

$$\frac{\partial E^{tot}}{\partial a}\delta a = \frac{\partial U^{tot}}{\partial a}\delta a + 2\gamma_s B\delta a = 0, \tag{3.43}$$

whereat $\Delta a = a - a_0$. For perfectly elastic materials, the crack hence propagates if the critical condition

$$\frac{\partial E^{tot}}{\partial a} = 0 \tag{3.44}$$

is met, giving rise to the crack growth criterion

$$-\frac{\partial U^{tot}}{\partial a} \geq 2\gamma_s \tag{3.45}$$

for unit thickness $B = 1$.

The left hand side of the inequality (3.45) is called (strain) energy release rate G, defined by Irwin [91]:

$$G = -\frac{\partial U^{tot}}{\partial a}. \tag{3.46}$$

The right hand side is accordingly denoted as critical energy release rate or crack (growth) resistance

$$G_C = 2\gamma_s, \tag{3.47}$$

and is an important material parameter which is commonly used in fracture mechanical analysis. As, in case of a purely mechanical problem, the total potential energy decreases during the irreversible crack growth process, the energy release rate G is always positive in this case. The definitions of the potential energies U^i and U^a, however, are completely open, allowing for including e.g. electrical and phason fields.

The energy release rate can be obtained by considering a virtual crack closure process, where the crack shape is retained. The work ΔW^s needed to close the crack along a segment $\Delta a \to 0$, in case of a reversal of the quasi-static crack growth process, is equal to the negative reduced potential energy of the system, i.e.

$$\Delta W^s = -\Delta U^{tot}. \tag{3.48}$$

In the case of piezoelectric QCs, not only the phonon part but also the phason and electrical parts are involved in the work W^s. The local work at a point on the closed crack face ($\theta = 0$ in the local polar coordinate system), see the dashed line in Fig. 3.5,

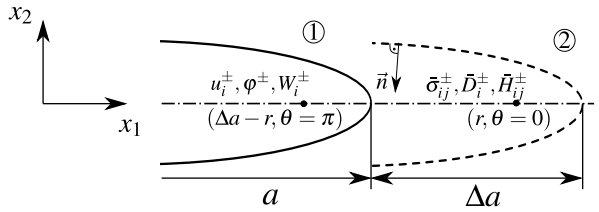

Figure 3.5.: Derivation of the crack closure integral in self-similar crack growth: the solid line represents the current crack faces ① and the dashed line the state after crack growth ②. The superscripts, $+$ and $-$, indicate the upper and lower crack faces, respectively.

is required for crack closure and is calculated as

$$\begin{aligned} dW^s(r,0) = &\int_{u_i^+}^{0} F_i^{\parallel +}\mathrm{d}x_i^{\parallel} + \int_{W_i^+}^{0} F_i^{\perp +}\mathrm{d}x_i^{\perp} - \int_{\varphi^+}^{0} Q^+\mathrm{d}\varphi \\ &+ \int_{u_i^-}^{0} F_i^{\parallel -}\mathrm{d}x_i^{\parallel} + \int_{W_i^-}^{0} F_i^{\perp -}\mathrm{d}x_i^{\perp} - \int_{\varphi^-}^{0} Q^-\mathrm{d}\varphi \\ = &-\frac{\bar{F}_i^{\parallel +}u_i^+}{2} - \frac{\bar{F}_i^{\perp +}W_i^+}{2} + \frac{\bar{Q}^+\varphi^+}{2} \\ &- \frac{\bar{F}_i^{\parallel -}u_i^-}{2} - \frac{\bar{F}_i^{\perp -}W_i^-}{2} + \frac{\bar{Q}^-\varphi^-}{2}, \end{aligned} \tag{3.49}$$

where the phonon forces $F_i^{\parallel}$, the phason forces $F_i^{\perp}$ and the electric charge Q effectuate respective displacements and electric potentials on the positive and negative crack faces $x_i^{\parallel} \in [u_i^{\pm}, 0]$, $x_i^{\perp} \in [W_i^{\pm}, 0]$ and $\varphi \in [\varphi^{\pm}, 0]$. When the crack is completely closed from state ② to state ①, the forces $\bar{F}_i^{\parallel}$, $\bar{F}_i^{\perp}$ and the electric charges $\bar{Q}$ denote the values on the ligament at positions $(r, \theta = 0)$.

Taking the outward unit normal vectors of the crack faces

$$n_i = (0, \mp 1)^T \tag{3.50}$$

for the positive and the negative crack face, the forces and the electric charges are then related to the stresses and the electric displacement as

$$\begin{aligned} \bar{F}_i^{\parallel} &= \bar{\sigma}_{i2} n_2 \mathrm{d}A = \mp \bar{\sigma}_{i2}\mathrm{d}A, \\ \bar{F}_i^{\perp} &= \bar{H}_{i2} n_2 \mathrm{d}A = \mp \bar{H}_{i2}\mathrm{d}A, \\ \bar{Q} &= -\bar{D}_2 n_2 \mathrm{d}A = \pm \bar{D}_2 \mathrm{d}A, \end{aligned} \tag{3.51}$$

where the upper sign stands for the positive and the lower sign for the negative crack surface.

Inserting Eq. (3.51) into Eq. (3.49), the local crack closure work is obtained:

$$\begin{aligned} dW^s &= \frac{1}{2}\bar{\sigma}_{i2}(u_i^+ - u_i^-)\mathrm{d}A + \frac{1}{2}\bar{H}_{i2}(W_i^+ - W_i^-)\mathrm{d}A + \frac{1}{2}\bar{D}_2(\varphi^+ - \varphi^-)\mathrm{d}A \\ &= \frac{1}{2}\bar{\sigma}_{I2}(u_I^+ - u_I^-)\mathrm{d}A. \end{aligned} \tag{3.52}$$

Exploiting the asymptotic crack tip solutions, the generalized displacements are always symmetric with respect to the positive and negative crack faces[1], i.e., $u_I^+ = -u_I^-$, and the crack closure work for a finite crack face ΔA is thus determined by the integration

$$\Delta W^s = -\Delta U^{tot} = \int_{\Delta A} \bar{\sigma}_{I2} u_I^+ \mathrm{d}A = B \int_{\Delta a} \bar{\sigma}_{I2} u_I^+ \mathrm{d}r, \tag{3.53}$$

where $\mathrm{d}A = B\mathrm{d}x_1 = B\mathrm{d}r$ in a plane crack problem with B as constant thickness. Referring to Fig. 3.5, where the displacements u_I are taken from the crack faces at $(\Delta a - r, \theta = \pi)$ and the tractions are taken from the ligament at $(r, \theta = 0)$ [115], where the bars above the variables can be omitted, the energy release rate G for a plane multiphysical problem is obtained by substituting Eq. (3.53) into Eq. (3.46):

$$\begin{aligned} G = \lim_{\Delta a \to 0} \frac{1}{\Delta a} \int_0^{\Delta a} &(\sigma_{i2}(r,0) u_i^+(\Delta a - r, \pi) + H_{i2}(r,0) W_i^+(\Delta a - r, \pi) \\ &+ D_2(r,0)\varphi^+(\Delta a - r, \pi))\mathrm{d}r. \end{aligned} \tag{3.54}$$

Taking displacements and stresses from two crack lengths, i.e., a and $a + \Delta a$, as shown in Fig. 3.5, the limit $\Delta a \to 0$ is essential for the application of the crack tip solutions in Eqs. (3.36) to just one crack length a. Eq. (3.54) providing an exact approach, two different crack lengths are likewise avoided for small, but finite Δa within a numerical context, which is the idea of the modified crack closure integral (MCCI) [115].

As one result, the energy release rate G is associated with the K-factors employing Eqs. (3.36). In compact notation, the relation reads

$$G = \lim_{\Delta a \to 0} \frac{1}{\Delta a} \int_0^{\Delta a} \sqrt{\frac{\Delta a - r}{\pi^2 r}} \mathrm{d}r K_P Y_{PQ} K_Q = \frac{1}{2} K_P Y_{PQ} K_Q, \tag{3.55}$$

where

$$Y_{PQ} = \Re\{i A_{PN} B_{NQ}^{-1}\} \tag{3.56}$$

is the generalized Irwin matrix for piezoelectric QCs. Substituting Eq. (3.56) into u_P according to Eqs. (3.36) with $\theta = \pm\pi$, indicating the generalized displacements on the

[1] An asymmetric crack opening, observed for arbitrary loading, is taken into account considering at least two terms of William's series [115].

crack faces, the displacement jump can be expressed as

$$\Delta u_P = (\Delta u_i, \Delta W_i, \Delta\varphi)^T = 2\sqrt{\frac{2r}{\pi}} Y_{PQ} K_Q. \tag{3.57}$$

Considering the energy associated terms in Eq. (3.54), where the different fields in piezoelectric QCs contribute to the energy for the assumed crack closure, the energy release rate is divided into the mechanical part G^m and the electrical part G^e:

$$\begin{aligned} G^m &= \lim_{\Delta a\to 0} \frac{1}{2\Delta a} \int_0^{\Delta a} (\sigma_{i2}(r,0)\Delta u_i(\Delta a - r,\pi) + H_{i2}(r,0)\Delta W_i(\Delta a - r,\pi))\,\mathrm{d}r, \\ G^e &= \lim_{\Delta a\to 0} \frac{1}{2\Delta a} \int_0^{\Delta a} (D_2(r,0)\Delta\varphi(\Delta a - r,\pi))\,\mathrm{d}r. \end{aligned} \tag{3.58}$$

According to the definition in classical fracture mechanics, the energy release rate G should be positive in a fracture process, while the theoretical results of the electromechanical and electrical energy release rates G and G^e can be negative, e.g., under pure or dominating electric loading conditions. Mathematically, negative potential energies are feasible due to the fact that the generalized stiffness tensor C_{IjKl} of piezoelectric isn't positive definite. From the energy point of view, the negative energy release rate indicates that the structure gains energy from the crack growth process, which contradicts Eq. (3.45), thus not permitting crack growth for the given loading. One physical interpretation of negative values of G requires considering the induced charges along the crack faces. Positive and negative charges appear on the crack faces and produce an attractive Coulomb force, which tends to close the crack [73, 163, 166]. If the mechanical energy release rate is negative, the analytical solution of the displacement field will show that the crack faces penetrate each other. Requiring the crack faces to be separate, G^m should have a positive magnitude [153].

Following the concept of conventional fracture mechanics [132], the second energy term H is defined by formally replacing σ_{i2}, H_{i2} and D_2 by σ_{i1}, H_{i1} and D_1 in Eq. (3.54):

$$\begin{aligned} H = &\underbrace{\lim_{\Delta a\to 0} \frac{1}{2\Delta a} \int_0^{\Delta a} (\sigma_{i1}(r,0)\Delta u_i(\Delta a - r,\pi) + H_{i1}(r,0)\Delta W_i(\Delta a - r,\pi))\,dr}_{H^m} \\ &+ \underbrace{\lim_{\Delta a\to 0} \frac{1}{2\Delta a} \int_0^{\Delta a} (D_1(r,0)\Delta\varphi(\Delta a - r,\pi))\,dr}_{H^e}, \end{aligned} \tag{3.59}$$

again including a mechanical part H^m and an electrical part H^e. Similar to Eq. (3.55),

H can be expressed in terms of field intensity factors as follows [206]:

$$H = -\frac{1}{2} K_P S_{PJ} Y_{JQ} K_Q \tag{3.60}$$

with

$$S_{PJ} = \Re\{B_{JN} P^{\mathrm{S1}}_{NM}(\theta = 0) B^{-1}_{MP}\} \tag{3.61}$$

and

$$P^{\mathrm{S1}}_{NM}(\theta = 0) = \mathrm{diag}(p_K). \tag{3.62}$$

While G is introduced as the energy release rate and has a specific physical meaning, interpretation of H with respect to crack closure is not known. It is considered to be an auxiliary quantity, which can be used, e.g., in numerical fracture analysis, particularly in connection with the J-integral [105].

Referring to cracks in anisotropic materials, the material constants related matrices Y_{IJ} and S_{IJ} are modified by rotating the local coordinate system at the crack tip as the crack deflects. In this regard, the local Y_{IJ} and S_{IJ} have to be calculated repeatedly based on the local general elastic tensor $\hat{C}_{IjKl}$ or, for saving computational cost, transformed from the initial state by substituting Eq. (3.32) into Eqs. (3.56), (3.61) and (3.62), respectively:

$$\begin{aligned} \hat{Y}_{IJ} &= \Omega_{IK}\Omega_{JL} Y_{KL}, \\ \hat{S}_{IJ} &= \Omega_{IK}\Omega_{JL}\Re\{B_{LN}\hat{P}^{\mathrm{S1}}_{NM}(\theta = 0) B^{-1}_{MK}\}, \end{aligned} \tag{3.63}$$

with

$$\hat{P}^{\mathrm{S1}}_{NM}(\theta = 0) = \mathrm{diag}(\hat{p}_Q). \tag{3.64}$$

3.3.3. The generalized J-integral

In the following, a rigorous derivation of the J-integral, as an interpretation of the concept of configurational forces is given in detail, starting from the first law of thermodynamics with the specific quantities

$$\mathrm{d}u = \mathrm{d}w_{rev} + \mathrm{d}q + \mathrm{d}\chi, \tag{3.65}$$

where the kinetic energy in this quasi-static process is neglected. u and q are the internal energy and the heat flux densities, respectively. The work of external loads is separated into the reversible part w_{rev} and the dissipative part χ. Since the specific electric enthalpy Π according to Eq. (2.32) is taken into account in piezoelectrics as thermodynamic potential, u is replaced by Π in the following derivation. Inserting $\mathrm{d}w_{rev} = \sigma_{Ij}\mathrm{d}\varepsilon_{Ij}$ and $\mathrm{d}q = T\mathrm{d}s^a$ into Eq. (3.65), where T is the absolute temperature and s^a is specific exchange entropy, the specific enthalpy of piezoelectric QCs in Eq. (2.67) is thus given as

$$\mathrm{d}\Pi = \sigma_{ij}\mathrm{d}\varepsilon_{ij} + H_{ij}\mathrm{d}w_{ij} - D_j\mathrm{d}E_j + T\mathrm{d}s^a + \mathrm{d}\chi. \tag{3.66}$$

Assuming an adiabatic system without heat flux, i.e., $\mathrm{d}s^a = 0$, the specific dissipative work is obtained as

$$\mathrm{d}\chi = \mathrm{d}\Pi - \sigma_{ij}\mathrm{d}\varepsilon_{ij} - H_{ij}\mathrm{d}w_{ij} + D_j\mathrm{d}E_j. \tag{3.67}$$

A continuum is considered, including a point defect with a virtual displacement δz_k in a control volume V. According to Eq. (3.67), the associated dissipative virtual work in the control volume is

$$F_k\delta z_k = \int_V \delta\chi \mathrm{d}V = \int_V \left(\delta\Pi - \sigma_{ij}\delta\varepsilon_{ij} - H_{ij}\delta w_{ij} + D_j\mathrm{d}E_j\right)\mathrm{d}V, \tag{3.68}$$

where F_k is a material or configurational force acting at the defect, which raises the dissipative work. Neglecting inertia and other volumetric forces, the balance equations $\sigma_{Ij,j} = 0$ are satisfied. With the virtual works

$$\begin{aligned} \sigma_{ij}\delta\varepsilon_{ij} &= (\sigma_{ij}u_{i,k})_{,j}\delta z_k \\ H_{ij}\delta w_{ij} &= (H_{ij}W_{i,k})_{,j}\delta z_k \\ D_j\delta E_j &= -(D_j\varphi_{,k})_{,j}\delta z_k \end{aligned} \tag{3.69}$$

and the relation

$$\delta\Pi = \Pi_{,k}\delta z_k = (\Pi\delta_{kj})_{,j}\delta z_k, \tag{3.70}$$

where $\delta\Pi$ denotes the change of the potential energy due to a virtual defect displacement δz_k, the configurational force of piezoelectric QCs is determined according to Eq. (3.68) by eliminating δz_k:

$$F_k = \int_V (\Pi\delta_{kj} - \sigma_{ij}u_{i,k} - H_{ij}W_{i,k} - D_j\varphi_{,k})_{,j}dV. \tag{3.71}$$

The energy-momentum tensor, originally introduced for classical materials [49], is generalized in this case for piezoelectric QCs as

$$Q_{kj} = \Pi\delta_{kj} - \sigma_{ij}u_{i,k} - H_{ij}W_{i,k} - D_j\varphi_{,k}. \tag{3.72}$$

The configurational force in a plane problem is transformed into a contour integral applying the divergence theorem to Eq. (3.71), obtaining

$$F_k = \oint_\Gamma Q_{kj}n_j d\Gamma, \tag{3.73}$$

where n_j is the outward unit normal and the contour Γ is a path enclosing the defect. It has been proved that the path integral yields the same value as long as the contour surrounds the same singularity and is zero if the enclosed area is free of any kind of defect [158]. Hence, the integral is path-independent. Applying Eq. (3.73) to a crack-like defect, the configurational force is denoted as the J-integral, i.e., $F_k = J_k$.

Similar to the consideration of Eq. (3.58), dividing the reversible work w_{rev} and the specific enthalpy $\Pi = \Pi^m + \Pi^e$ into the mechanical ($\Pi^m = \sigma_{ij}\varepsilon_{ij}/2 + H_{ij}w_{ij}/2$) and

electrical ($\Pi^e = -D_i E_i/2$) parts, the configurational force and the J-integral, respectively, are thus expressed as separate contributions [205]:

$$F_k = J_k = \underbrace{\oint_\Gamma \left(\Pi^m \delta_{kj} - \sigma_{ij} u_{i,k} - H_{ij} W_{i,k}\right) n_j \mathrm{d}\Gamma}_{F_k^m, J_k^m} + \underbrace{\oint_\Gamma \left(\Pi^e \delta_{kj} - D_j \varphi_{,k}\right) n_j \mathrm{d}\Gamma}_{F_k^e, J_k^e}. \tag{3.74}$$

The J-integral is related to the energy release rate via the reduction of total potential energy δU^{tot} due to virtual crack growth δa, in a plane structure of unit thickness ($B = 1$) reading

$$\delta U^{tot} = -J_k \delta z_k = -(J_k^m + J_k^e)\delta z_k = -G\delta a = -(G^m + G^e)\delta a, \tag{3.75}$$

where $\delta z_k = z_k \delta a$ with $z_k z_k = 1$. Taking into account Eq. (3.68), the mechanical contribution of the J-integral and configurational force, respectively, give rise to one part of entropy production, which is attributed to the mechanical process of crack growth.

If the crack propagates in x_1-direction, i.e., $\vec{z} = \vec{e}_1$ the energy release rate corresponds to the projection of the $\vec{J}$-vector on the $\vec{e}_1$ basis vector:

$$G = J_1. \tag{3.76}$$

For isotropic materials, Eq. (3.76) can be analytically verified by comparing J_1, incorporating the asymptotic near-tip solutions and integrating along a small contour, to G calculated from the crack closure integral [157]. Applying the Irwin relationship Eq. (3.55), J_1 is thus readily expressed in terms of intensity factors K_N. J_2, which is non-zero in any case of mixed-mode loading, is known to be related to H of Eq. (3.59), however for a classical K_I/K_{II}-problem [132]:

$$H = -J_2. \tag{3.77}$$

This relation is confirmed just as Eq. (3.76) by introducing K-factors on both sides. It could further be shown that Eq. (3.77) holds as well for piezoelectrics [205] and QCs [206]. This gives the opportunity to calculate the J_k-vector of a multiphysical problem from K-factors, applying Eqs. (3.55) and (3.60), thus sparing the implementation of a contour integral. Appendix C provides a proof of Eq. (3.77).

Despite Eqs. (3.76) and (3.77) being satisfied in piezoelectric QCs, the separation of (G, H) and J_k into mechanical and electrical parts are not equivalent. The coordinates of the path-independent integral J_k^m and the driving force F_k^m, respectively, have different interpretations in comparison with G^m and H^m, leading to

$$J_1^m \neq G^m, \quad J_2^m \neq -H^m. \tag{3.78}$$

In contrast to the energy release rate and the K-factors, the J-integral can be applied to crack problems in nonlinear materials, e.g., QCs with plastic properties if they are heated to more than a few hundred degrees. A further advantage of the application

of the J_k is that the inaccurate treatment in the near-tip field, where the stress/strain gradients are extremely large, can be avoided by choosing a contour far away from the crack tip, providing an accurate result of the fracture parameter. Finally, the J_k-vector provides information not only on the crack tip loading but also on the direction of crack deflection.

3.4. Crack growth criteria

Except for fatigue issues, cracks tend to propagate when the loading at the crack tip is beyond a threshold. Stress at the crack tip as a loading quantity, however, is not an appropriate parameter to forecast this phenomenon due to stress singularity. Accounting for this limitation, the K-factors and the energy release rate are mainly used in fracture mechanics as criteria for crack assessment. In the case of a pure mode-I loading, the fracture criterion is

$$K_I = K_{IC}, \tag{3.79}$$

where K_{IC} is the critical value known as the fracture toughness. It is defined as the resistance of the material against crack growth and is considered to be independent of specimen thickness or other geometrical quantities. In a mixed-mode loading case, an equivalent stress intensity factor K_V should be introduced, considering all K-factors, e.g., for a mixed mode-I/II case, there is a hypothesis

$$K_V = \frac{K_I}{2} + \frac{1}{2}\sqrt{K_I^2 + 4(\alpha_1 + K_{II})^2} \leq K_{IC}, \tag{3.80}$$

where the material parameter $\alpha_1 = K_{IC}/K_{IIC}$ is defined as the ratio of the critical values of mode I and mode II [161].

In ferroelectric materials, the application of the K-factors as fracture parameters requires appropriate modifications based on a deeper understanding of the mechanism involved in the crack growth process. Many studies have shown that a remote electric loading, ferroelectric phenomena and loadings on the crack faces can have a major impact on fracture behavior, e.g., in [55, 196]. In specific, the modification should be based on two aspects. The first is the impact of the applied loads on the crack tip toughness

$$K_{IC}^{tip} = K_{IC}^{app} + \Delta K_I(K_I^{app}, K_{IV}^{app}), \tag{3.81}$$

where K_{IC}^{tip} is the effective toughness at the crack tip and K_{IC}^{app} is the critical value associated with K_I^{app}. K_I^{app} and K_{IV}^{app} are functions depending on the applied remote loading according to Eq. (3.33). The effective toughness at the crack tip K_{IC}^{tip} in Eq. (3.81) differs from the applied critical loading K_{IC}^{app} by ΔK_I, which is controlled by the applied mechanical and electrical loads K_I^{app} and K_{IV}^{app}, since there is the crack tip shielding effect along with the ferroelectric activities due to the domain switching and the domain wall motion on the mesoscopic scale [74, 164]. On the other hand, the applied crack tip loading K_I^{app}, which is associated with K_{IC}^{app}, also depends on the

solution of the selected boundary condition on the crack faces

$$K_I^{app} = f(\sigma_{ij}^{\infty}, D_i^{\infty}, \sigma_{ij}^{C}, D_i^{C}), \tag{3.82}$$

where ∞ denotes the remote loads and C the crack medium. The influence of the tractions on the crack faces on K_I^{app} was discussed comprehensively in [74] and the boundary conditions will be introduced in the following subsection.

From the energy point of view, inequality (3.45) has already provided a criterion of critical crack growth

$$G = G_C \tag{3.83}$$

valid in linear elastic fracture mechanics, which further evolves into

$$J_k z_k = J_C = G_C \tag{3.84}$$

due to Eq. (3.75).

This energy criterion works well for classical structural materials. However, fracture behavior in materials with electromechanically or phonon–phason coupled properties does not necessarily follow this criterion due to the effect of the electric or phason field on the energy release rate. The crack growth mechanism, which is a mechanical process, may justify the consideration of the mechanical strain energy release rate G^m in a fracture criterion for analysis in ferroelectric or quasicrystalline materials, confining the crack closure only to the mechanical state [55, 116, 153]. In this case, the electric field affects the fracture behavior solely as a result of the coupling effect. The corresponding fracture criterion

$$G^m = G_C^m \tag{3.85}$$

is thus established, where the electrical part in the total energy release rate according to Eq. (3.58) is neglected and possibly also the phason contribution.

It should be noted that the critical values of these two criteria, G_C and G_C^m, show different tendencies if a positive electric field is superimposed on mechanical loads, implying an increased resistance in crack propagation on the basis of G_C and a decrease in G_C^m due to the negative value of G^e [164]. It was also confirmed by the fracture toughness calculated from experimental data in the same work.

Looking closer at the separation displacement of the upper and lower crack surfaces near a crack tip, where the deformation blunts the initially sharp crack, offers another fracture criterion

$$\delta_t = \delta_{tc}, \tag{3.86}$$

where δ_t and δ_{tc} are the crack tip opening displacement (CTOD) and its critical value, respectively [22, 209]. Fig. 3.6(a) illustrates the crack faces, which have been calculated numerically with nonlinear mechanical behavior in a_c. The $\sqrt{r}$-dependent crack faces in red, which are in the K-factors dominated region and free of any traction, end at the physical crack tip as shown in Fig. 3.6(a). Between the physical and fictitious crack tips, the crack faces in blue are governed by a traction-separation law, where the cohesive stress $\sigma(\delta_t)$ is a function of the separation δ_t. Consequently, the stress

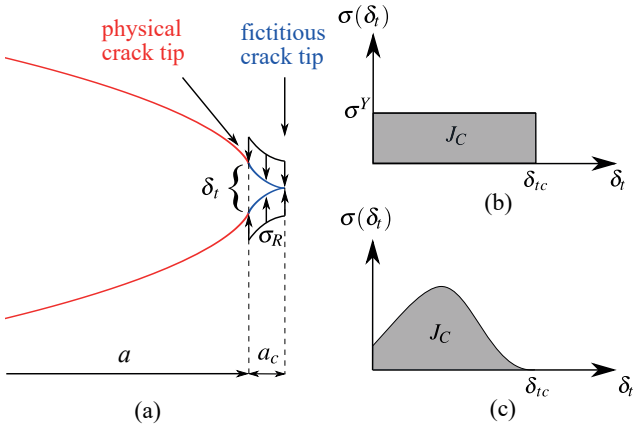

Figure 3.6.: (a) Crack faces with crack tip opening displacement at the physical crack tip. a_c is the region where the yield stress σ^Y according to (b) the Dugdale-model [42] or the interatomic stress according to (c) the Barenblatt-model [13] is applied.

singularity at the fictitious crack tip is canceled by the cohesive stress $\sigma(\delta_t)$ and the K-factors are thus zero. This criterion can also be applied to ductile materials since the plasticity is intrinsically involved.

The CTOD is mainly investigated in two models with distinct traction-separation laws governing the displacement-stress relationship on the fictitious crack faces. If the stress in a plastic zone a_c meets the yield stress σ^Y and ideal plasticity is presumed, as shown in Fig. 3.6(b), this is called Dugdale model. The size of the yield zone depends on the ratio of the applied loading and the yield stress [42]. For linear elastic materials, the fictitious part of the crack constitutes the fracture process zone given by Irwin [90]. In this model, originated in the work of Barenblatt [13], separation at the atomic level is considered, relating the nuclear force and the separation of atoms as shown in Fig. 3.6(c). Some other traction-separation laws have also been proposed [151]. This class of models is called the cohesive zone model and has been widely used for modeling cracks in composites or reinforced materials as well as for simulations of delamination.

The crack growth criteria based on J and δ_t are identical. The critical values J_C and δ_{tc} are related by the surface underneath the function $\sigma(\delta_t)$ from 0 to δ_{tc}

$$J_C = \int_0^{\delta_{tc}} \sigma(\delta_t) \mathrm{d}\delta, \tag{3.87}$$

as shown in Fig. 3.6(b) and (c), respectively.

The CTOD was also discussed in soft QCs [51] and employed to simulate crack propa-

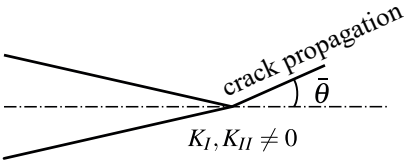

Figure 3.7.: Crack deflection under mixed-mode loading.

gation in piezoelectrics and ferroelectrics, in particular, by using the Barenblatt-model, e.g. [113]. In specific, the crack opening δ_t may be of interest at piezoelectric and ferroelectric materials if a semi-permeable crack is considered, since an additional Coulomb force related on δ_t plays an essential role in the traction-separation law due to the electric charges on crack faces. While the solution of crack opening in classical materials subjected to a remote tensile stress can be derived from different methods [150, 157], for a semi-permeable crack in coupled materials, $\delta(x)$ is obtained by superposing the displacement solution of remote loadings with the one induced by an electric load on the crack faces.

3.5. Crack deflection criteria

In classical materials with isotropic fracture behavior, the crack grows straightforward along its ligament in a single mode-I loading case, while the crack deflects under mixed-mode loading, e.g., a mode-I case is superimposed by mode-II, see Fig. 3.7. Devices with piezoelectric components mostly operate under combined electromechanical loadings and K_{II} can be induced by pure tensile stress due to the coupling effect, resulting in a mixed-mode loading case, whereupon crack deflection is a common occurrence in these materials. Thus, the electric displacement intensity factor K_{IV}, as an additional field intensity factor, may also have an indirect effect on crack deflection. However, the influence of K_{IV} on crack deflection is still a contentious issue. In anisotropic materials, the mixed-mode crack tip loading is not the only factor inducing crack deflection. The anisotropic crack growth resistance, e.g., the fracture toughness or the critical energy release rate, depending on the crack growth direction, leads to a different deflection angle in comparison with the result based on the isotropic fracture behavior. For instance, a crack may deflect significantly under pure mode-I loading in a fiber-reinforced composite, where orthotropic crack resistance prevails [106].

Several crack deflection criteria for isotropic solids have been developed in classical structural materials, estimating the angle of deflection and crack paths. The criteria and their validations are summarized in [156, 160]. Two prominent criteria and a third criterion, which is specially modified for piezoelectrics, will be introduced in the following subsections.

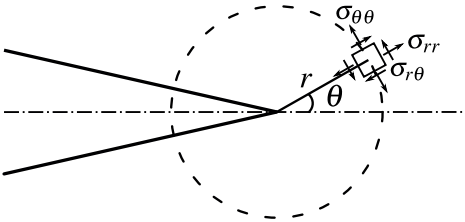

Figure 3.8.: Stress state in polar coordinates around a crack tip.

3.5.1. Maximum hoop stress criterion

One of the most applied crack deflection criteria is the maximum hoop stress criterion, which is considered to work well with brittle materials [48]. According to this criterion, the crack grows into the direction $\bar{\theta}$ where the hoop stress $\sigma_{\theta\theta}$ reaches its maximum, see Fig. 3.8. This criterion can be implemented if the hoop stress is formulated as a function of the angle θ:

$$\left.\frac{\partial \sigma_{\theta\theta}}{\partial \theta}\right|_{\theta=\bar{\theta}} = 0, \qquad \left.\frac{\partial^2 \sigma_{\theta\theta}}{\partial \theta^2}\right|_{\theta=\bar{\theta}} < 0. \tag{3.88}$$

The near-field hoop stress, related to the K-factors and the angular functions according to Eqs. (2.14) and (3.36), are inserted into Eq. (3.88). In the case of an isotropic material, the crack deflection angle $\bar{\theta}$ can be readily calculated, indicating the dependence on the ratio of K_I and K_{II}:

$$\bar{\theta} = 2\arctan\left(\frac{1}{4}\frac{K_I}{K_{II}} - \frac{1}{4}\sqrt{\left(\frac{K_I}{K_{II}}\right)^2 + 8}\right). \tag{3.89}$$

Thus, the crack under pure mode-I loading will propagate in a forward direction and the deflection angle under pure mode-II loading is $\pm 70.5°$, depending on the direction of the shear stress near the crack tip.

While the definition of the stress field is unique for conventional crystals, the crack tip in QCs is subjected to two classes of stress, the phonon and the induced phason stresses. In this work, only the phonon stresses are taken into account in the maximum hoop stress criterion, and the phason field has an influence on $\sigma_{\theta\theta}$ due to the coupling effect, see Eq. (2.68). The same holds for piezoelectrics according to Eqs. (3.36), where the stress $\sigma_{\theta\theta}$ is influenced by the electric displacement intensity factor.

3.5.2. J-integral vector criterion

The J-integral vector criterion was suggested to use path-independent integrals to study crack growth problems under mixed-mode loadings [84]. It postulates that the crack

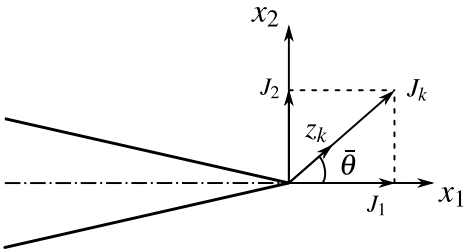

Figure 3.9.: The crack deflection angle $\bar{\theta}$ determined by the J-integral vector criterion.

propagates in the direction of the J-vector (or the configurational force), see Fig. 3.9. According to Eq. (3.75), the loss of the total potential energy $J_k z_k$ takes a maximum if z_k and J_k are linearly dependent, thus leading to a maximum energy release rate. The deflection angle is accordingly determined by

$$\bar{\theta} = \arctan\left(\frac{J_2}{J_1}\right) = \arctan\left(\frac{-H}{G}\right), \tag{3.90}$$

where the Eqs. (3.76) and (3.77) are considered. For a conventional material, the deflection angle according to Eq. (3.90) can be determined by G and H, which are related to the K-factors. The basic advantage of applying G and H in Eq. (3.90) is that by applying Eqs. (3.55) and (3.60) the J-integral vector can be calculated without any contour or equivalent domain integral. Eq. (3.90) is basically applicable to multiphysical problems, if the total potential energy stored in all degrees of freedom is considered relevant for crack deflection.

The application of the J-integral vector criterion has the advantage that the anisotropic material behavior is readily incorporated, not requiring the anisotropic eigenfunctions of the Williams series. It has been successfully validated on the basis of experimental findings in classical structural materials of various anisotropic ratios [105, 106]. However, a directional variation of crack resistance requires further modification for piezoelectric QCs.

The deflection angles versus the ratio of K_{II}/K_I based on the introduced deflection criteria are shown in Fig. 3.10. The maximum energy release rate (ERR) criterion, which has been successfully applied to crack path predictions [88], is also illustrated in the graph as a third criterion. The deflection angles based on the maximum ERR criterion in black and the maximum hoop stress criterion in blue are close to each other, showing a coincident tendency with the increased ratio of K_{II}/K_I. They are also consistent with experimental observations. However, the crack deflection angles determined by the J-integral vector criterion and illustrated in the red dashed line have a significant deviation in comparison with the other results if the ratio reaches a certain magnitude. It claims that the deflection reduces dramatically in cases governed by mode-II loading. This unrealistic result (for brittle materials) indicates that the application of the J-integral vector criterion for predicting crack deflection is only pragmatic under the $K_{II} < K_I$ condition, which is commonly satisfied for critical crack growth.

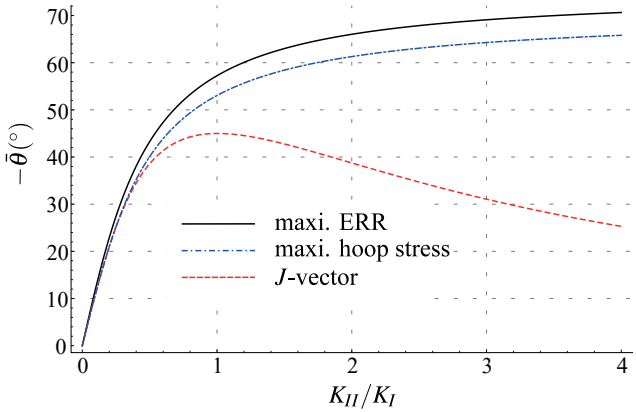

Figure 3.10.: Comparison of the crack deflection angles based on different deflection criteria.

3.5.3. Modified J-integral vector criterion

In one common approach for piezoelectric fracture problems based on the energy release rate, the electric contribution is neglected in the fracture criterion, see Eq. (3.85). The J-integral crack deflection criterion accordingly shall also be modified, considering just the mechanical part as the driving force of crack propagation. The mechanical part of the J-integral, J_k^m, is taken from Eq. (3.74). The modified J-integral vector criterion is thus formulated as follows:

$$\bar{\theta} = \arctan\left(\frac{J_2^m}{J_1^m}\right). \tag{3.91}$$

In contrast to Eq. (3.90), where J_1 and J_2 are related to G and H, there is no analogous relation here due to the inequality according to Eq. (3.78), which is why the implementation of a contour integral is unavoidable.

3.6. Mechanical and electric boundary conditions on crack faces

Generally, the crack faces in linear elasticity are free of tractions if the load is not directly applied there. Thus,

$$t_i^+ = t_i^- = \sigma_{i2}^+ = \sigma_{i2}^- = 0 \tag{3.92}$$

at any point of the upper and lower crack faces according to the normal vectors given in Eq. (3.50). However, possible electric boundary conditions on the crack faces are numerous. One simple assumption is that the crack interior is considered to possess

a similar dielectric property as the body [154]. As a result, the electric field is not disturbed by the crack and the electric potential is continuous across the crack faces:

$$\varphi^+ = \varphi^-. \tag{3.93}$$

In so-called permeable crack model, the electric displacement singularity at the crack tip and the electric displacement intensity factor are independent of the remote electric loading and are only induced by the coupling effect.

In contrast to the permeable boundary condition, a crack can be assumed to be totally circumvented by the electric field, leading to zero electric displacement D_2 on crack faces [146]:

$$D_2^+ = D_2^- = 0, \quad \text{and} \quad \varphi^+ \neq \varphi^-. \tag{3.94}$$

Similar to the mechanical boundary condition, the crack faces are free of electric charge. It implies that the dielectric property of the crack medium is totally neglected. This crack model with zero permittivity in the crack interior is called impermeable. The assumption is plausible, since the dielectric constants of piezoelectric materials are typically about 10^3 times larger compared to the atmosphere, e.g., vacuum or air. On the other hand, the crack has an extreme aspect ratio of length and crack opening, fostering its electric penetration. The singularities of the electric displacement and the stresses in front of a Griffith crack tip, represented by the K-factors, are independent of each other.

Later, the electric boundary condition has been modified by considering a limited electric permeability of the crack interior. A capacitor approach has been proposed [81], where the crack faces are modeled as a capacitor plates with intrinsic surface charges. The limited permeability of the electric field determines the relation between the local crack opening Δu_2 and the potential difference $\Delta\varphi$ across the crack faces which have to satisfy the electrostatic equilibrium, i.e.

$$D_2 \Delta u_2 = -\kappa_c \Delta\varphi, \tag{3.95}$$

where κ_c is the permittivity of the crack medium. Additionally, Maxwell stresses induced by electrostatic tractions on the crack faces have an effect on the loading of a crack. Due to the nonlinear behavior of the stress-displacement relationship in the crack interior, a solution can only be obtained from an iterative approach. Several studies have investigated this boundary condition and employed the capacitor analogy model for crack tip loading analysis, e.g., [73, 163, 166].

Some other models have been developed, taking the nonlinear electric behavior in front of the crack tip into account. Analogous to the classical Dugdale model with assumed ideal plasticity in the plastic zone in front of the crack tip, a strip saturation model has been proposed [67]. This model takes advantage of the fact that, to a certain extent, the electric displacement and the electric field phenomenologically play similar roles as stress and strain, effectuating a constant electric displacement if the electric field reaches a 'yielding' point. A similar saturation model, the strip dielectric breakdown model, was developed in [216], where the electric field strength saturates

in front of the physical crack tip, as the local electric field is much larger than the dielectric breakdown strength. Both models avoid the electric singularity at the crack tip, just as classical cohesive zone models, see Section 3.4, and consider linear elasticity since piezoelectric materials are generally extremely brittle.

The phason stress in QCs, introduced as an auxiliary quantity for complementing the constitutive equations, has no classical mechanical interpretation. Thus, a phason stress cannot be applied as a conventional load and is assumed

$$h_i = 0 \tag{3.96}$$

on all boundaries. Also, the measurement of the induced phason tractions has not been published. The homogeneous Neumann boundary condition must therefore be satisfied for the phason stress on the crack faces:

$$H_{i2}^{+} = H_{i2}^{-} = 0. \tag{3.97}$$

4. Finite element implementation

The finite element (FE) methodology, among other numerical approaches, has been developed and employed as one of the most important and widespread numerical methods for solving various boundary value problems of physical models and providing well approximated solutions [16]. It is an indispensable part, particularly in engineering analysis, e.g., in mechanics. In solid mechanics, the boundary value problems governed by balance laws and constitutive equations are presented in an integral formulation (weak formulation), while the entire body is subdivided into finite small subdomains (finite elements) according to a discretization procedure, constituting a mesh structure. The weak formulation is then applied to every single small subdomain. The governing integral equations are approximated using various weighted residual methods. The commonly used weighted residual method in solid mechanics is the Galerkin method, which takes the functional bases as the weighting functions, often a set of first variations of independent variables [201]. In order to obtain an approximate solution, the definite integral of a subdomain is replaced by a weighted sum of the function values at specified points, where weighting factors can be selected based on the Gaussian quadrature rule. The required values of variables on the subdomains are approximated by the nodal values and a set of shape functions. The finite element method on a boundary value problem finally yields a system of algebraic equations. For a given problem, the accuracy of the approximate solution can be improved by taking either higher-order shape functions or more elements in discretization. Especially for the simulation in fracture mechanical problems, an appropriately optimized element mesh structure is required, since very large and inaccurate values emerge near the crack tip. In the FE environment, various numerical techniques in post-processing can be applied based on the output of the approximate solutions. The details of the techniques and the application in fracture mechanics can be found e.g. in [115].

Many commercial software tools, e.g., Abaqus, provide a solver together with predefined pre- and post-processing tools, which cover most engineering applications. The pre-processing tools help to define a boundary value problem and discretize the body, ultimately constructing the required system of algebraic equations, which is numerically solved in the solver. There are typically several types of built-in elements, including common physical properties, which considerably facilitates the job. As far as fracture mechanics is concerned, post-processing tools can compute fracture loading quantities in classical materials, e.g., K-factors and the J-integral. Their applications, however, are typically restricted to simple problems with straight cracks, neglecting mass inertia or body forces. Unfortunately, the available FE software tools do not have any built-in element type for QCs, where the degree of freedom in the phason field and the phonon–phason coupling effect are lacking in the definition of the materials.

Furthermore, a post-processing tool for the calculation of fracture loading quantities in piezoelectric materials is missing, since the effect of an electric field on fracture behavior is still a controversial issue. Many modifications of the fracture quantities for structural materials with electric behavior have been proposed and analyzed [55, 216], however, none has been accepted as a commonly feasible approach.

In order to overcome these limitations, some studies in the framework of FE have been carried in this work to allow crack growth simulations in piezoelectric QCs. Firstly, the basic weak formulations for the FE method are derived from the variational principle of virtual work, where the multi-field materials, including phonon, phason and electric fields, are considered. Since an element type for QCs is not available, a special USER-element subroutine was developed in the commercial FE software Abaqus, containing the desired physical properties and allowing a user self-defined system of algebraic equations. Secondly, Abaqus cannot calculate fracture quantities from any simulation job with cracks, if the crack-tip elements have piezoelectric properties. Thus, in this work some modified methods for calculating fracture loading quantities are taken into account and are employed in a post-processing tool.

4.1. Numerical solution of the piezoelectric quasicrystalline boundary value problem via FEM

4.1.1. Weak formulation and discretization

The weak formulation of piezoelectric QCs, which holds for a computational domain, is required in order to solve boundary value problems by applying the FE method. While for dynamic problems it can be derived from the Hamiltonian variational principle, for static problems it is equivalent to the variational principle of virtual work, formulated as

$$\delta \int_V w \, \mathrm{d}V - \delta \int_V \Pi \, \mathrm{d}V = 0, \tag{4.1}$$

where w is the specific work done by external loading and Π is the specific generalized electric enthalpy of piezoelectric QCs referred to Eq. (2.67). δ indicates the first variation. The specific virtual work in QCs with piezoelectric property is defined as

$$\delta w = t_i \delta u_i + h_i \delta W_i - \omega \delta \varphi, \tag{4.2}$$

where the virtual work of the electric field is derived from Eq. (2.30) with

$$\delta \varphi = -E_i \delta l_i. \tag{4.3}$$

Body forces and charge are neglected here. Hence, the weak formulation is obtained

from Eq. (4.1) by inserting Eqs. (2.67) and (4.2)

$$\int_\Gamma \bar{t}_i \delta u_i \mathrm{d}\Gamma + \int_\Gamma \bar{h}_i \delta W_i \mathrm{d}\Gamma - \int_\Gamma \bar{\omega} \delta \varphi \mathrm{d}\Gamma - \frac{1}{2}\delta \int_V (\sigma_{ij}\varepsilon_{ij} + H_{ij}w_{ij} - D_i E_i)\,\mathrm{d}V = 0, \quad (4.4)$$

where the tractions with bar indicate the loading at boundaries Γ. Since the variational terms, δu_i, δW_i and $\delta\varphi$, are zero on their Dirichlet boundaries, the integration in Eq. (4.4) is formulated over the whole surface Γ instead of just their Neumann boundaries. Substituting the constitutive equations Eq. (2.68) into Eq. (4.4) yields

$$\begin{aligned}\frac{1}{2}\delta \int_V \Big((C_{ijkl}\varepsilon_{kl} + R_{ijkl}w_{kl} - e_{ijk}E_k)\varepsilon_{ij} + (R_{klij}\varepsilon_{kl} + K_{ijkl}w_{kl})w_{ij} - (e_{kli}\varepsilon_{kl} + \kappa_{ik}E_k)E_i \Big)\,\mathrm{d}V \\ - \int_\Gamma \bar{t}_i \delta u_i \mathrm{d}\Gamma - \int_\Gamma \bar{h}_i \delta W_i \mathrm{d}\Gamma + \int_\Gamma \bar{\omega}\delta\varphi \mathrm{d}\Gamma = 0.\end{aligned} \quad (4.5)$$

With the expansion of the variational derivative, the weak formulation reads

$$\begin{aligned}\int_V \Big((C_{ijkl}u_{k,l} + R_{ijkl}W_{k,l} + e_{ijk}\varphi_{,k})\delta u_{i,j} + (R_{klij}u_{k,l} + K_{ijkl}W_{k,l})\delta W_{i,j} \\ + (e_{kli}u_{k,l} - \kappa_{ik}\varphi_{,k})\delta\varphi_{,i} \Big)\,\mathrm{d}V - \int_\Gamma \bar{t}_i \delta u_i \mathrm{d}\Gamma \\ - \int_\Gamma \bar{h}_i \delta W_i \mathrm{d}\Gamma + \int_\Gamma \bar{\omega}\delta\varphi \mathrm{d}\Gamma = 0.\end{aligned} \quad (4.6)$$

This weak formulation in the FEM is applied to a computational domain and verified for test functions. The computational domain is normally a single element of mesh structures. Test functions, in this case, are solutions of the displacements and the electric potential, approximated by interpolation with a sum of shape functions h^α in each element

$$\begin{aligned} u_k(x_i) &= \sum_{\alpha=1}^{n} h^\alpha(x_i)\tilde{u}_k^\alpha, \\ W_k(x_i) &= \sum_{\alpha=1}^{n} h^\alpha(x_i)\tilde{W}_k^\alpha, \\ \varphi(x_i) &= \sum_{\alpha=1}^{n} h^\alpha(x_i)\tilde{\varphi}^\alpha, \end{aligned} \quad (4.7)$$

where the variables with a tilde are the nodal values of the element. The shape functions must satisfy certain specific conditions, which ensure the required continuous property and allow the interpolated fields u_k, W_k and φ to take the nodal values at their respective positions.

Inserting the expressions of Eq. (4.7) into Eq. (4.6) the weak formulation yields the approximation:

$$\begin{aligned}
&\sum_{\beta=1}^{n} \delta\tilde{u}_i^\beta \Bigg(\int_V C_{ijkl} \sum_{\alpha=1}^{n} \frac{\partial h^\alpha}{\partial x_l} \frac{\partial h^\beta}{\partial x_j} \mathrm{d}V \, \tilde{u}_k^\alpha + \int_V R_{ijkl} \sum_{\alpha=1}^{n} \frac{\partial h^\alpha}{\partial x_l} \frac{\partial h^\beta}{\partial x_j} \mathrm{d}V \, \tilde{W}_k^\alpha + \int_V e_{ijk} \sum_{\alpha=1}^{n} \frac{\partial h^\alpha}{\partial x_k} \frac{\partial h^\beta}{\partial x_j} \mathrm{d}V \, \tilde{\varphi}^\alpha \Bigg) \\
&\quad + \sum_{\beta=1}^{n} \delta\tilde{W}_i^\beta \Bigg(\int_V R_{klij} \sum_{\alpha=1}^{n} \frac{\partial h^\alpha}{\partial x_l} \frac{\partial h^\beta}{\partial x_j} \mathrm{d}V \, \tilde{u}_k^\alpha + \int_V K_{ijkl} \sum_{\alpha=1}^{n} \frac{\partial h^\alpha}{\partial x_l} \frac{\partial h^\beta}{\partial x_j} \mathrm{d}V \, \tilde{W}_k^\alpha \Bigg) \\
&\quad + \sum_{\beta=1}^{n} \delta\tilde{\varphi}^\beta \Bigg(\int_V e_{kli} \sum_{\alpha=1}^{n} \frac{\partial h^\alpha}{\partial x_l} \frac{\partial h^\beta}{\partial x_i} \mathrm{d}V \, \tilde{u}_k^\alpha - \int_V \kappa_{ik} \sum_{\alpha=1}^{n} \frac{\partial h^\alpha}{\partial x_k} \frac{\partial h^\beta}{\partial x_i} \mathrm{d}V \, \tilde{\varphi}^\alpha \Bigg) \\
&\quad - \sum_{\beta=1}^{n} \delta\tilde{u}_i^\beta \int_\Gamma \bar{t}_i h^\beta \, \mathrm{d}\Gamma - \sum_{\beta=1}^{n} \delta\tilde{W}_i^\beta \int_\Gamma \bar{h}_i h^\beta \, \mathrm{d}\Gamma + \sum_{\beta=1}^{n} \delta\tilde{\varphi}^\beta \int_\Gamma \bar{\omega} h^\beta \, \mathrm{d}\Gamma = 0.
\end{aligned} \tag{4.8}$$

By eliminating the virtual displacements $\delta\tilde{u}_i^\beta$ and $\delta\tilde{W}_i^\beta$ and the virtual electric potential $\delta\tilde{\varphi}^\beta$, Eq. (4.8) transforms into three balance equations. For the sake of conciseness and clarity, the index notation is temporarily replaced by the matrix notation and the equations are written as

$$\begin{aligned}
\int_V \underline{B}_u^{\mathrm{T}} \underline{C} \underline{B}_u \mathrm{d}V \{\tilde{u}\} + \int_V \underline{B}_u^{\mathrm{T}} \underline{R} \underline{B}_w \mathrm{d}V \{\tilde{W}\} + \int_V \underline{B}_u^{\mathrm{T}} \underline{e} \underline{B}_e \mathrm{d}V \{\tilde{\varphi}\} - \int_\Gamma \underline{N}_u^{\mathrm{T}} \{\bar{t}\} \, \mathrm{d}\Gamma = 0, \\
\int_V \underline{B}_w^{\mathrm{T}} \underline{R}^{\mathrm{T}} \underline{B}_u \mathrm{d}V \{\tilde{u}\} + \int_V \underline{B}_w^{\mathrm{T}} \underline{K} \underline{B}_w \mathrm{d}V \{\tilde{W}\} - \int_\Gamma \underline{N}_w^{\mathrm{T}} \{\bar{h}\} \, \mathrm{d}\Gamma = 0, \\
\int_V \underline{B}_e^{\mathrm{T}} \underline{e}^{\mathrm{T}} \underline{B}_u \mathrm{d}V \{\tilde{u}\} - \int_V \underline{B}_e^{\mathrm{T}} \underline{\kappa} \underline{B}_e \mathrm{d}V \{\tilde{\varphi}\} + \int_\Gamma \underline{N}_e^{\mathrm{T}} \{\bar{\omega}\} \, \mathrm{d}\Gamma = 0,
\end{aligned} \tag{4.9}$$

where $\underline{B}_u$, $\underline{B}_w$ and $\underline{B}_e$ are differentiated shape functions for the displacements and the electric potential of an element and $\underline{N}_u$, $\underline{N}_w$ and $\underline{N}_e$ are the shape function matrices. The variable in curly braces indicates a column matrix. $\{\tilde{u}\}$, $\{\tilde{W}\}$ and $\{\tilde{\varphi}\}$ are the nodal values of an element. The dimensions of these matrices are dependent on the selected shape functions and the number of phason degrees of freedom, which varies from one to three. The matrices of a 1D QC with piezoelectric property are given in the next subsection.

The generalized stiffness matrix $\underline{K}_S$ is then assembled by different constituents

$$\underline{K}_S = \begin{pmatrix} \underline{K}_{uu} & \underline{K}_{uw} & \underline{K}_{ue} \\ \underline{K}_{uw}^{\mathrm{T}} & \underline{K}_{ww} & 0 \\ \underline{K}_{ue}^{T} & 0 & \underline{K}_{ee} \end{pmatrix} \tag{4.10}$$

with

$$\begin{aligned}
\underline{K}_{uu} &= \int_V \underline{B}_u^{\mathrm{T}} \underline{C} \underline{B}_u \mathrm{d}V, \qquad \underline{K}_{ue} = \int_V \underline{B}_u^{\mathrm{T}} \underline{e} \underline{B}_e \mathrm{d}V, \\
\underline{K}_{ee} &= -\int_V \underline{B}_e^{\mathrm{T}} \underline{\kappa} \underline{B}_e \mathrm{d}V, \qquad \underline{K}_{uw} = \int_V \underline{B}_u^{\mathrm{T}} \underline{R} \underline{B}_w \mathrm{d}V, \\
\underline{K}_{ww} &= \int_V \underline{B}_w^{\mathrm{T}} \underline{K} \underline{B}_w \mathrm{d}V,
\end{aligned} \tag{4.11}$$

whereupon the system of algebraic equations according to Eq. (4.9) finally reads

$$\underline{K}_S \underline{\tilde{U}} = \underline{\tilde{F}}, \tag{4.12}$$

with the nodal values of the generalized displacements $\underline{\tilde{U}} = (\{\tilde{u}\} \ \{\tilde{W}\} \ \{\tilde{\varphi}\})^T$ and the generalized loads

$$\underline{\tilde{F}} = \begin{pmatrix} \int_\Gamma \underline{N}_u^{\mathrm{T}} \{\bar{t}\} \mathrm{d}\Gamma \\ \int_\Gamma \underline{N}_w^{\mathrm{T}} \{\bar{h}\} \mathrm{d}\Gamma \\ -\int_\Gamma \underline{N}_e^{\mathrm{T}} \{\bar{\omega}\} \mathrm{d}\Gamma \end{pmatrix}. \tag{4.13}$$

4.1.2. Shape functions, generalized stiffness matrices and Gaussian quadrature for second-order quadrilateral elements

A boundary value problem is transferred into a system of algebraic equations as shown in Eq. (4.12) for every element, where the shape functions h^α have to be defined. As previously introduced, the selected shape functions should be continuous over the element as well as at the element edges and represent the nodal values according to Eq. (4.7). Since the elements in the FE method often have different geometries, it is difficult to choose a set of appropriate shape functions for each element depending on its form and size due to an enormous amount of work. This problem is resolved by transforming the integrations of different elements into one simple element form, e.g., a regular triangle element or a square element. The simple element is defined in a local orthogonal coordinate system, called natural coordinate system, whereupon the shape functions depend only on the natural coordinates. A quadrilateral element with eight nodes is used in this work. Fig. 4.1 shows an arbitrary element and a unified simple quadrilateral element in the natural coordinate system (ξ, η). According to the isoparametric element concept, which is commonly employed for constructing polynomial shape functions in the FE method, all geometric nodes are simultaneously taken into account in the approximate solutions of the displacements and the electric potential. In other words, each geometric node is allocated a shape function. The second-order shape functions for an eight nodes quadrilateral element are listed in Fig.

4.1.

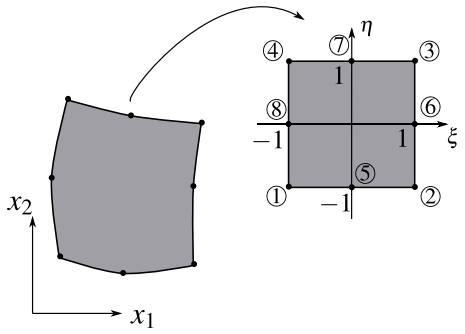

$$
\begin{aligned}
h^1 &= -\frac{1}{4}(1-\xi)(1-\eta)(1+\xi+\eta)\\
h^2 &= \frac{1}{4}(1+\xi)(1-\eta)(\xi-\eta-1)\\
h^3 &= \frac{1}{4}(1+\xi)(1+\eta)(\xi+\eta-1)\\
h^4 &= \frac{1}{4}(1-\xi)(1+\eta)(-\xi+\eta-1)\\
h^5 &= \frac{1}{2}(1-\xi^2)(1-\eta)\\
h^6 &= \frac{1}{2}(1+\xi)(1-\eta^2)\\
h^7 &= \frac{1}{2}(1-\xi^2)(1+\eta)\\
h^8 &= \frac{1}{2}(1-\xi)(1-\eta^2)
\end{aligned}
$$

Figure 4.1.: Integral on an element of arbitrary geometry is transformed in the natural coordinate system. The numbers in circles indicate the nodal index and for each node there is a shape function h^α.

Considering a piezoelectric QC with one phason degree of freedom in the quadrilateral element, the vectors in Eq. (4.9) are given as

$$
\begin{aligned}
\{\tilde{u}\} &= (u_1^1\ u_2^1\ u_1^2\ u_2^2\ u_1^3\ u_2^3\ u_1^4\ u_2^4\ u_1^5\ u_2^5\ u_1^6\ u_2^6\ u_1^7\ u_2^7\ u_1^8\ u_2^8)^T,\\
\{\tilde{W}\} &= (W^1\ W^2\ W^3\ W^4\ W^5\ W^6\ W^7\ W^8)^T,\\
\{\tilde{\varphi}\} &= (\varphi^1\ \varphi^2\ \varphi^3\ \varphi^4\ \varphi^5\ \varphi^6\ \varphi^7\ \varphi^8)^T,
\end{aligned}
\tag{4.14}
$$

where the superscripts refer to the nodes and the index of the phason displacement is neglected due to the single degree of freedom in the phason field. For the given element type, the shape function matrices and their differential matrices according to Eq. (4.9) are thus given as

$$
\begin{aligned}
\underline{N}_u &= \begin{pmatrix} h^1 & 0 & h^2 & 0 & h^3 & 0 & h^4 & 0 & h^5 & 0 & h^6 & 0 & h^7 & 0 & h^8 & 0\\ 0 & h^1 & 0 & h^2 & 0 & h^3 & 0 & h^4 & 0 & h^5 & 0 & h^6 & 0 & h^7 & 0 & h^8 \end{pmatrix},\\
\underline{N}_e &= \underline{N}_w = \begin{pmatrix} h^1 & h^2 & h^3 & h^4 & h^5 & h^6 & h^7 & h^8 \end{pmatrix},
\end{aligned}
\tag{4.15}
$$

and

$$\underline{B}_u = \begin{pmatrix} \partial h^1/\partial x_1 & 0 & \partial h^2/\partial x_1 & 0 & \cdots & \partial h^8/\partial x_1 & 0 \\ 0 & \partial h^1/\partial x_2 & 0 & \partial h^2/\partial x_2 & \cdots & 0 & \partial h^8/\partial x_2 \\ \partial h^1/\partial x_2 & \partial h^1/\partial x_1 & \partial h^2/\partial x_2 & \partial h^2/\partial x_1 & \cdots & \partial h^8/\partial x_2 & \partial h^8/\partial x_1 \end{pmatrix}, \tag{4.16}$$

$$\underline{B}_e = \underline{B}_w = \begin{pmatrix} \partial h^1/\partial x_1 & 0 & \partial h^2/\partial x_1 & 0 & \cdots & \partial h^8/\partial x_1 & 0 \\ 0 & \partial h^1/\partial x_2 & 0 & \partial h^2/\partial x_2 & \cdots & 0 & \partial h^8/\partial x_2 \end{pmatrix}.$$

According to the transformation into the natural coordinate system, the entries of $\underline{B}$ are further derived with the coordinates (ξ, η) as follows

$$\begin{pmatrix} \partial h^\alpha/\partial x_1 \\ \partial h^\alpha/\partial x_2 \end{pmatrix} = \underbrace{\begin{pmatrix} \partial \xi/\partial x_1 & \partial \eta/\partial x_1 \\ \partial \xi/\partial x_2 & \partial \eta/\partial x_2 \end{pmatrix}}_{\underline{J}^{-1}} \begin{pmatrix} \partial h^\alpha/\partial \xi \\ \partial h^\alpha/\partial \eta \end{pmatrix}, \tag{4.17}$$

where $\underline{J}^{-1}$ is the inverse Jacobian matrix. The Jacobian matrix $\underline{J}$, given by partially differentiating one coordinate system with respect to another, describes the coordinate transformation. Here, it is defined as the gradient of the global coordinates x_i with respect to the natural coordinates (ξ, η):

$$\underline{J} = \frac{\partial(x_1, x_2)}{\partial(\xi, \eta)} = \begin{pmatrix} \partial x_1/\partial \xi & \partial x_2/\partial \xi \\ \partial x_1/\partial \eta & \partial x_2/\partial \eta \end{pmatrix}. \tag{4.18}$$

Substituting the shape functions and the nodal coordinates into Eq. (4.18), the entries of the Jacobian matrix are

$$\frac{\partial x_i}{\partial \xi} = \sum_{\alpha=1}^{8} \frac{\partial h^\alpha}{\partial \xi} x_i^\alpha \qquad \text{and} \qquad \frac{\partial x_i}{\partial \eta} = \sum_{\alpha=1}^{8} \frac{\partial h^\alpha}{\partial \eta} x_i^\alpha. \tag{4.19}$$

The determinant of the Jacobian matrix $|\underline{J}|$ represents the ratio of infinitesimal areas in the global and the natural coordinate systems. Accordingly, the integral area of the element holds the relation

$$\mathrm{d}x_1 \mathrm{d}x_2 = |\underline{J}| \, \mathrm{d}\xi \, \mathrm{d}\eta. \tag{4.20}$$

Thus, the stiffness matrices in Eq. (4.11) can be rewritten for a single element in the natural coordinate system, where the general volume integral is replaced by an area

integral for a planar problem. For example, $\underline{K}_{uu}$ in (ξ,η) is

$$\underline{K}_{uu} = \int_{x_2}\int_{x_1} \underline{B}_u(x_1,x_2)^{\mathrm{T}}\,\underline{C}\,\underline{B}_u(x_1,x_2)\mathrm{d}x_1\mathrm{d}x_2 = \int_{\eta}\int_{\xi} \underline{B}_u(\xi,\eta)^{\mathrm{T}}\,\underline{C}\,\underline{B}_u(\xi,\eta)\,|\underline{J}|\,\mathrm{d}\xi\,\mathrm{d}\eta \tag{4.21}$$

and other stiffness matrices can be transformed analogously:

$$\begin{aligned}
\underline{K}_{ue} &= \int_{\eta}\int_{\xi} \underline{B}_u(\xi,\eta)^{\mathrm{T}}\,\underline{e}\,\underline{B}_e(\xi,\eta)\,|\underline{J}|\,\mathrm{d}\xi\,\mathrm{d}\eta \\
\underline{K}_{ee} &= -\int_{\eta}\int_{\xi} \underline{B}_e(\xi,\eta)^{\mathrm{T}}\,\underline{\kappa}\,\underline{B}_e(\xi,\eta)\,|\underline{J}|\,\mathrm{d}\xi\,\mathrm{d}\eta \\
\underline{K}_{uw} &= \int_{\eta}\int_{\xi} \underline{B}_u(\xi,\eta)^{\mathrm{T}}\,\underline{R}\,\underline{B}_w(\xi,\eta)\,|\underline{J}|\,\mathrm{d}\xi\,\mathrm{d}\eta \\
\underline{K}_{ww} &= \int_{\eta}\int_{\xi} \underline{B}_w(\xi,\eta)^{\mathrm{T}}\,\underline{K}\,\underline{B}_w(\xi,\eta)\,|\underline{J}|\,\mathrm{d}\xi\,\mathrm{d}\eta.
\end{aligned} \tag{4.22}$$

The domain integrals in Eqs. (4.21) and (4.22) are further approximated by using the Gaussian quadrature as a standard numerical integral procedure in the FE method. The Gaussian quadrature is an approximation of the definite integral of a function, stated as the sum of weighting factors multiplied by the function values at specified points within the interval of integration [201]. For a simple one-dimensional integral case with the most common interval $[-1,1]$, the approximation of the Gaussian quadrature is formulated as

$$\int_{-1}^{1} f(x)dx \approx \sum_{i=1}^{n} \omega_i f(x_i), \tag{4.23}$$

where ω_i are the weighting factors for the representative integration points. The choice of the latter, which are commonly also denoted as Gaussian points, and the weighting factors are outlined in many textbooks, e.g., [201]. For a quadrilateral element with eight nodes, there are nine integration points for a complete integral approximation. Fig. 4.2 illustrates the positions of integration points. The natural coordinates of the points and the corresponding weighting factors are listed in Tab. 4.1.

4.1.3. Numerical examples and verification

Since the standard elements in the FE software Abaqus lack the phason degree of freedom, a self-defined USER-element is implemented, incorporating the phonon, phason and electric fields. The required approximation procedure for stiffness matrices according to Eqs. (4.21) and (4.22) has been so far introduced and thus can be numerically calculated. The calculation is executed in a Fortran subroutine, which is compatible with Abaqus for constructing the system of algebraic equations for each

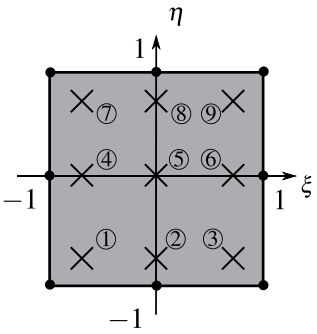

Figure 4.2.: Nine integration points of two dimensional Gaussian quadrature in a quadrilateral element.

i	ξ	η	ω_i
1	−0.7746	−0.7746	0.3086
2	0	−0.7746	0.4938
3	0.7746	−0.7746	0.3086
4	−0.7746	0	0.4938
5	0	0	0.7901
6	0.7746	0	0.4938
7	−0.7746	0.7746	0.3086
8	0	0.7746	0.4938
9	0.7746	0.7746	0.3086

Table 4.1.: The natural coordinates of the integration points and the corresponding weighting factors.

element and finally for the whole domain. The system of algebraic equations is solved by the Abaqus solver. Since user-defined elements are not supported by the Abaqus post-processing, an in-house code is applied for this purpose.

The solutions of the USER-element subroutine have to be verified before they are employed in the analysis of crack problems in piezoelectric QCs. As a basic fracture problem, the Griffith crack model is most favorable for verification, since it has a closed-form solution and the modeling in the FE environment is comparatively simple. The analytical solutions according to Eq. (3.24), which can be examined by using the so-called orthogonality relations of A_{IJ} and B_{IJ} [195], are compared with numerical results. An electric impermeable Griffith crack in a 1D piezoelectric QC, where the x_2-axis is the QA and further represents the poling direction, is taken for verification. The applied material constants are given in Appendix A.4. Due to the symmetry of the Griffith crack model and its loading condition, a quarter model with a half crack length is set up in Abaqus, where the model edge l is much larger than the half crack length ($a = 0.1l$) and a remote tensile stress $\sigma_{22}^{\infty} = 200\,\text{Pa}$ is applied. The outer boundary of the model is free of electric charge and phason loading. Thus, the electric field and the phason field are induced by the mechanical loading due to the coupling effect of the piezoelectric QCs. The nodal outputs of the phonon and phason displacements as well as the electric potential on the upper crack face near the crack tip are demonstrated in Fig. 4.3, and compared to the analytic solutions based on Eq. (3.24). As shown in Fig. 4.3, the numerical results from Abaqus, which are computed via the USER-element subroutine with the plane strain condition, are consistent with the closed-form solutions, whereupon the subroutine is considered to produce accurate results.

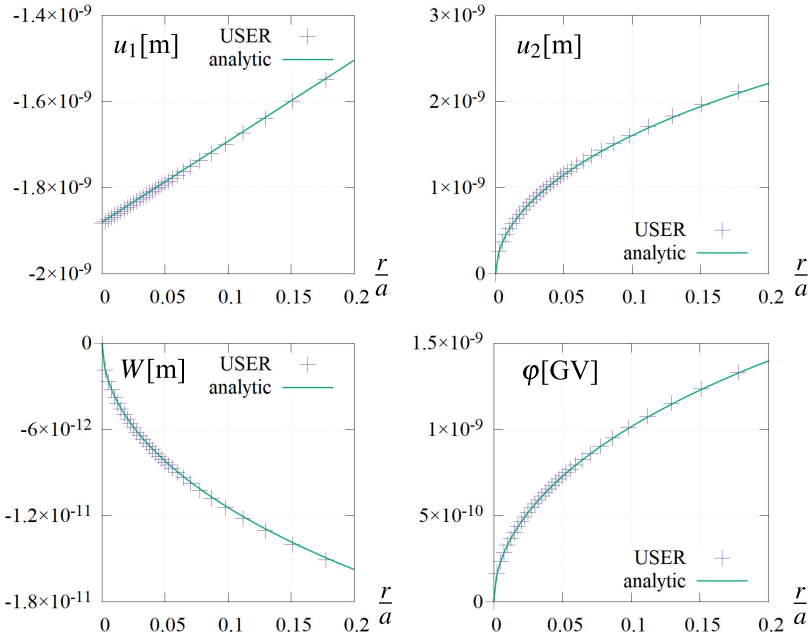

Figure 4.3.: Comparison of the analytic solutions according to Eq. (3.24) (green line) and the numerical outputs represented by the plus symbols. The horizontal axis represents the normalized distance from the crack tip ($x = r/a$).

4.2. Numerical calculation of crack tip loading quantities

The fracture mechanical loading quantities, e.g., the K-factors and the J-integral, describe the specific loading condition at a crack tip and are thus vital for crack growth simulations. In addition, many crack deflection criteria directly or indirectly depend on the loading quantities. However, an analytical expression of loading quantities is barely available for a crack problem. Although many formulae are given in [193], they are often complex and very specific, and thus cannot be applied in crack growth simulations. Based on the solutions of the FE method according to Section 4.1, numerical post-processing tools efficiently and flexibly provide fracture mechanical loading quantities. Various post-processing methods and the associated mesh structures of discretization have been developed for accurately calculating the loading quantities [101, 115]. In general, the straightforward methods, which are based on the stresses and the displacements near the crack tip, cannot avoid the influence of the singularity, leading to less accurate results. Hence, an indirect method and a modified path-independent integral are used in this work and briefly introduced in the following subsections.

4.2.1. Crack tip element method (CTEM)

The solutions according to Eq. (3.36) provide the relation between K-factors and the generalized field quantities near the crack tip, allowing the K-factors to be inversely calculated based on the FE outputs. However, there are two conflicts between the required FE outputs and the implemented near-tip solutions due to the crack tip singularity, on the one hand side, and the range of validity of the asymptotic solution on the other, giving rise to an issue of accuracy of the numerical calculation.

An improved element type, called crack tip element, avoids this conflict and thus meets the requirements of solution quality [15, 85]. This element type is originally a quadrilateral element with eight nodes, where three nodes on one side of the element are collapsed to one point, degenerating from a quadrilateral to a triangular element. The overlapping points are at the crack tip and such triangular crack tip elements are arranged circularly around the crack tip. The middle nodes at the element edges are shifted from the original positions to the quarter positions in the direction of the crack tip, so that the asymptotic $\sqrt{r}$-behavior is intrinsically included in their displacements functions [115]. Fig. 4.4 illustrates the degeneration steps of an eight-node element and Fig. 4.5 shows a mesh structure near the crack tip. It has to be noted that the shape functions of the crack tip isoparametric elements as well as the natural coordinates are still the same as in Fig. 4.1, however, with the modified positions of the nodes. Consequently, the generalized displacements of the positive crack face are given in the form of a polynomial approximation as follows

$$u_P(r) = a_P^0 + a_P^1\sqrt{\frac{r}{L}} + a_P^2\frac{r}{L}, \tag{4.24}$$

where a_P^0, a_P^1 and a_P^2 are three coefficients and the second term characterizes exactly the square root proportionality of the near-tip displacements on the crack face according to Eq. (3.27). Substituting r of the nodes A, B and C, displayed in Fig. 4.5, into Eq. (4.24), gives the nodal displacements as functions of the coefficients a_P:

$$\begin{aligned} u_P(0) &= u_P^A = a_P^0, \\ u_P(L/4) &= u_P^B = a_P^0 + \frac{1}{2}a_P^1 + \frac{1}{4}a_P^2, \\ u_P(L) &= u_P^C = a_P^0 + a_P^1 + a_P^2. \end{aligned} \tag{4.25}$$

Therefore, $a_P^{0/1/2}$ are obtained as

$$\begin{aligned} a_P^0 &= u_P^A, \\ a_P^1 &= -3u_P^A + 4u_P^B - u_P^C, \\ a_P^2 &= 2u_P^A - 4u_P^B + 2u_P^C. \end{aligned} \tag{4.26}$$

The CTEM calculates the field intensity factors based on Eq. (3.57), which states that the calculation does not require the generalized displacements of just one crack face

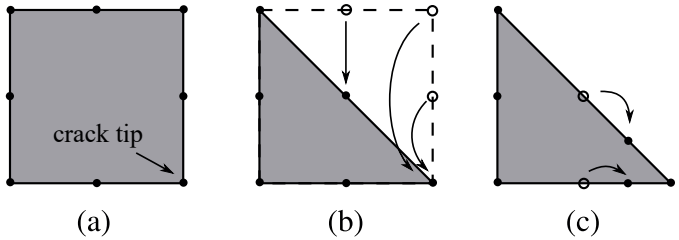

Figure 4.4.: Modification of an eight-node isoparametric element at the crack tip: (a) its original form, (b) collapsed into triangular form, (c) two middle nodes shifted to the quarter position. This type of crack-tip element exhibits a $\sqrt{r}$-proportionality of the generalized displacements.

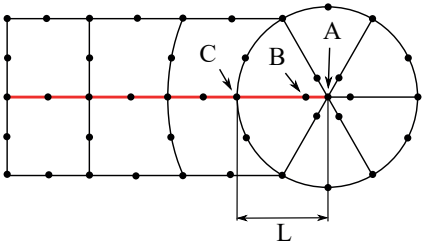

Figure 4.5.: Mesh structure near the crack tip. Node A is the crack tip, node B is at a quarter position. The nodes on the middle line in red (crack faces) are overlapping double nodes from the positive and negative crack faces.

but rather the generalized crack opening displacements Δu_P. Whereas the last term in Eq. (4.24) can be neglected for $r \to 0$, the second term with the $\sqrt{r}$-proportionality dominates in the near-tip field. Thus, the crack opening displacements read

$$\Delta u_P(r) = (-3\Delta u_P^A + 4\Delta u_P^B - \Delta u_P^C)\sqrt{\frac{r}{L}}. \tag{4.27}$$

The node A is located at the crack tip, where the crack opening displacements are zero, $\Delta u_P(r)$ is thus further given as

$$\Delta u_P(r) = (4\Delta u_P^B - \Delta u_P^C)\sqrt{\frac{r}{L}}. \tag{4.28}$$

Inserting Eq. (4.28) on the left-hand side of Eq. (3.57), the field intensity factors are obtained as

$$K_Q = \frac{1}{2}\sqrt{\frac{\pi}{2L}}Y_{QP}^{-1}(4\Delta u_P^B - \Delta u_P^C). \tag{4.29}$$

In this method, the expression of K-factors eludes the $1/\sqrt{r}$-singularity and thus has a clear and accurate result. Applying the CTE method in a Griffith crack model introduced in Section 4.1.3, where the analytic solution for the K-factors is given in Eq.

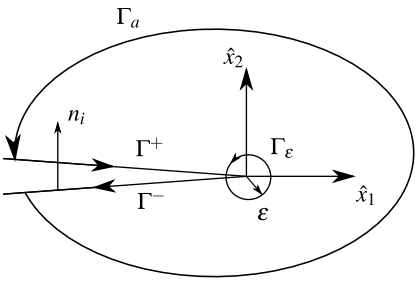

Figure 4.6.: Contours of the J-integral; arrows indicate the orientations of the integration paths.

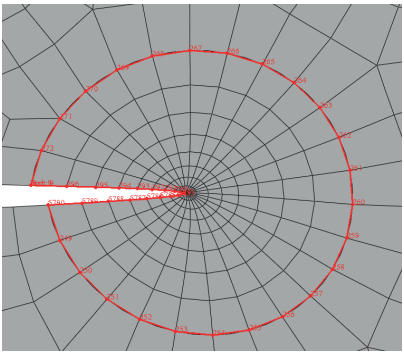

Figure 4.7.: An integral path for computing J_k in a FE model in Abaqus, highlighted in the deformed geometry.

(3.34), this post-processing tool has a deviation of about 1%, if a very fine mesh near the crack tip is allocated. Accounting for the modification factor of geometry [193], which empirically corrects the discrepancy between a bounded finite element model and the ideal infinite Griffith crack model, the deviation is further reduced to 0.4%.

4.2.2. J-integral

The J_k-vector can be numerically calculated along an integral contour by applying the path independent integral according to Eq. (3.74) to a crack problem. Generally, a closed contour can be selected including both crack faces, however, excluding the crack tip as illustrated in Fig. 4.6. The J-integral is zero without any heterogeneity or defect in the enclosed domain:

$$J_k = \oint_{\Gamma} Q_{kj} n_j \, \mathrm{d}\Gamma = \oint_{\Gamma_a + \Gamma^+ - \Gamma_\varepsilon + \Gamma^-} Q_{kj} n_j \, \mathrm{d}\Gamma = 0. \tag{4.30}$$

Nevertheless, as long as the inner contour Γ_ε is sufficiently small, the J-integral of the crack tip can be calculated based on either Γ_ε or a finite contour including both crack faces:

$$\begin{aligned} J_k &= \lim_{\varepsilon \to 0} \int_{\Gamma_\varepsilon} Q_{kj} n_j \, \mathrm{d}\Gamma \\ &= \int_{\Gamma_a} Q_{kj} n_j \, \mathrm{d}\Gamma + \lim_{\varepsilon \to 0} \int_{\Gamma^+ + \Gamma^-} (\Pi n_k - \sigma_{Ij} n_j u_{I,k}) \, \mathrm{d}\Gamma. \end{aligned} \tag{4.31}$$

Since the unloaded crack faces are traction free and the phason traction has no mechan-

ical interpretation, leading to $\sigma_{ij}n_j = 0$ and $H_{ij}n_j = 0$, and if impermeable crack face boundary conditions are further assumed, i.e. $D_j n_j = 0$, the J-integral in Eq. (4.31) is reduced to

$$J_k = \int_{\Gamma_a} Q_{kj} n_j \mathrm{d}\Gamma + \lim_{\varepsilon \to 0} \int_{\Gamma^+ + \Gamma^-} \Pi n_k \mathrm{d}\Gamma. \tag{4.32}$$

The J-integral according to Eq. (4.32) has been numerically implemented, integrating along an automatically generated contour. The integral contour, illustrated in Fig. 4.7, runs along the crack faces and element edges surrounding the crack tip at sufficiently large distance. However, the straightforward application of Eq. (4.32) in a post-processing procedure has its limitation in some special cases, e.g., if the crack tip approaches an interface or if two cracks are close to each other. Under these circumstances, the outer contour Γ_a is obliged to approach the crack tip due to the geometric constrains, whereupon the numerical integration has to use inaccurate nodal values. In order to resolve such problems, a remote contour can be chosen instead of the local contour focused on the crack tip. This approach requires some special treatment which can be found in [103, 104].

In particular, if straight crack faces with the boundary condition $\sigma_{Ij}n_j = 0$ are assumed to be in the integral contour as depicted in Fig. 4.6, the normal vector coordinate n_1 on the crack faces is zero in the crack tip coordinates $(\hat{x}_1, \hat{x}_2)$. In this case, J_1 does not require an integration along the crack faces Γ^+ and Γ^-. In the calculation of J_2, however, the crack face integral on Γ^+ and Γ^- unavoidably contains the nodal outputs near the crack tip, resulting in comparatively large errors due to the singularity. The graphs in Fig. 4.8 show the J-integral according to Eq. (4.32) from a mixed-mode loading simulation of a straight crack, integrating along the crack faces. The normalized coordinate $\tilde{x}_1$ indicates segments of the integral contour $\Gamma^{+/-}$. In detail, the circles represent results of incomplete integration paths, where Γ^+ starts at $\tilde{x}_1 = 0$ and ends right in front of the crack tip at $\tilde{x}_1 = 1$. The physical magnitudes J_1/J_2 are thus obtained at $\tilde{x}_1 = 1$. The line of J_2 in red seems to yield a feasible value, except for the last increment, which is calculated from the two nodes right in front of the crack tip, leading to a considerable error. J_1, on the other hand, is not affected since it only depends on the integration along Γ_a. A simple way to obtain a rational result of J_2 is to neglect the last few increments of the crack face integral and to determine the actual value by extrapolation, as shown in Fig. 4.8 by the black square symbol at $\tilde{x}_1 = 1$. Compared to the result based on the CTEM and Eqs. (3.60) and (3.77), the extrapolated J_2 has a 3% deviation. In light of the above issue, the common role of the J-integral, providing a reference of crack tip loading analysis, must be put into perspective, as soon as not just $J_1 = G$ of a straight crack is considered.

Details and some other advanced numerical methods to achieve an accurate J_2 are found in [47, 102]. Accounting for the T-stress, one approach employs the analytic and numerical solutions in an iterative scheme to get a result of the J_k-integral, where the inaccurate values near the crack tip are faded out in the numerical contour integral. Another method separates J_2 into symmetric and antisymmetric parts with regard to the stresses on the crack faces, which are individually extrapolated towards the crack tip. Both methods likewise satisfy the requirement of accuracy.

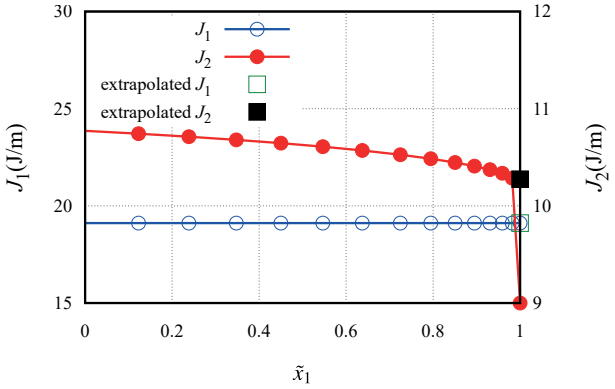

Figure 4.8.: The J-integral based on Eq. (4.32) vs. normalized coordinate along the crack face, where $\tilde{x}_1 = 0$ indicates the intersection of Γ_a and $\Gamma^{+/-}$ and $\tilde{x}_1 = 1$ is at the crack tip. The magnitudes of J_k refer to a plane structure of unit thickness.

Compared to the CTEM, the advantage of this post-processing method is that no special element is required at the crack tip. Accordingly, all element types as well as shape functions can be applied without specific modifications.

4.3. Adaptive re-meshing algorithm of crack growth

Many studies focus on the numerical calculation of crack tip loading quantities to achieve assessments of a crack, which has been well developed in terms of a static crack problem. However, with regard to the prediction of crack growth or crack paths, special numerical techniques and algorithms are required. In the context of the FEM, various numerical approaches have been developed to simulate crack growth since the pioneering work in 1967 [143]. The element splitting method and the element elimination method provide special treatments for the elements in front of a crack, which are involved in the crack advance. The crack either grows in the middle of the elements or eliminates the elements on the ligament, thus creating a propagating crack path [34, 138]. In the moving crack tip method, the crack-tip elements move with the crack tip and the local mesh is readjusted repeatedly. Since a special element type is applied, where the singularities are represented in the shape functions, the static or dynamic stress intensity factors can be directly computed [144]. The cohesive zone model based on Barenblatt [13] and Dugdale [42] can be conveniently applied to simulate crack growth. Nevertheless, the main disadvantage is that the separation can only takes place along a predefined line, a crack deflection is thus impossible. The extended finite element method (XFEM), developed in 1999 [17, 139], is popular in the simulation of crack propagation [10]. It is advantageous as the mesh in the initial state can be retained during the failure process and thus there is no need to adjust the elements.

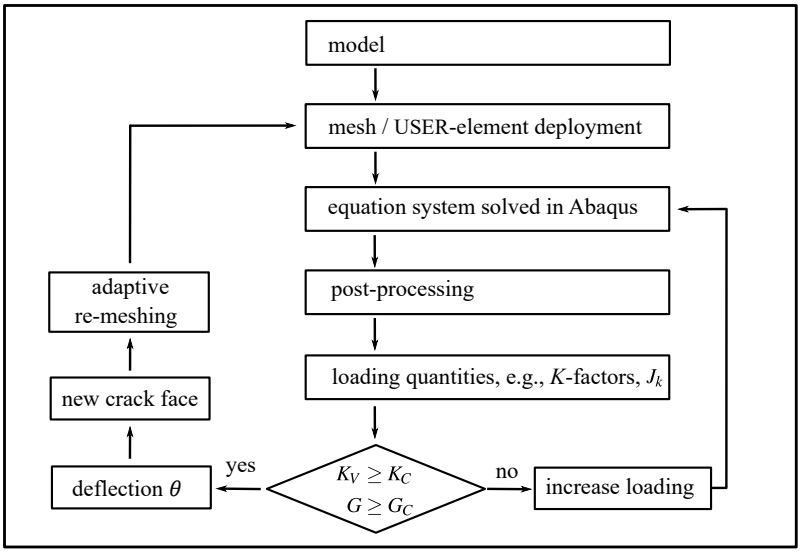

Figure 4.9.: Flow chart of the adaptive re-meshing algorithm for crack growth simulations.

The displacement discontinuity due to cracking is embedded in the element by discontinuous shape functions and selected near tip enrichment functions. Besides the FE methods, the boundary element method (BEM) is also a popular tool for simulating crack propagation [8]. The BEM reduces the problem dimensionality by one order by only discretizing the surface of a boundary value problem, thus, fewer discrete points are involved saving computational cost [133].

Amongst other methods, the smart adaptive re-meshing algorithm based on the FE method is an effective solution technique for crack propagation simulations, which was originally proposed in [136, 172] and later generalized for coupled materials [94, 204]. The simulation algorithm repeatedly constructs the mesh and refines it near the crack tip. Fig. 4.9 demonstrates the workflow of the re-meshing algorithm for crack growth simulations applied in this work. In order to ensure an optimized mesh structure without highly distorted elements near the crack tip, where the calculation is sensitive to numerical errors, an additional partition is inserted around the crack tip and the suitable nodes are allocated. Outside of this region, there is an irregular arrangement of elements. The post-processing tools according to Sections 4.2.1 and 4.2.2 have been implemented to provide the fracture mechanical loading quantities and the deflection angle, which is determined by the deflection criteria introduced in Section 3.5. In every crack growth increment, the new crack tip is shifted in the predicted deflection direction and the whole model is meshed again with refinement. The crack increment length is chosen sufficiently small to provide convergent crack paths and large enough to avoid unnecessary computational cost.

5. Crack path predictions

In this chapter, the introduced crack tip loading analysis, crack deflection criteria and the adaptive re-meshing algorithm in the FE environment are employed for the prediction of crack paths. Two special cases are considered first. By neglecting the electric properties or the phason field, crack growth is simulated in QCs and piezoelectrics, respectively. In QCs, only the classical mechanical loading of the phonon field is applied and the phason K-factor is thus induced by the coupling effect, affecting loading quantities and deflections. In piezoelectrics, both mechanical and electric loadings are possible on the boundary, while diverse loading combinations are taken into account. Then, the crack paths in a 1D piezoelectric QC are presented in the last part.

5.1. Crack paths in 1D QCs

As introduced in Chapter 3, different fracture problems in QCs have been analytically investigated. A lot of numerical works have also been carried out, dealing with cracks by using various approaches. A meshless local Petrov-Galerkin approach was proposed, solving boundary value problems in 2D QCs with cracks [179]. Dynamic crack propagation has been numerically investigated in a Griffith crack model by using an extended finite difference method [217]. The influence of the phonon–phason coupling effect on fracture loading quantities was assessed by an extended displacement discontinuity BEM [126]. Regarding the FEM, approaches for QCs including cracks have been established in [178, 206, 213] and the crack deflection affected by the coupling effect has been analytically and numerically investigated in [206]. Later, crack paths in 1D QCs subjected to mixed-mode loadings have been predicted [204]. Apart from the linear constitutive relations in QCs based on the model introduced in Section 2.3.3, a strain-gradient theory was developed and the J-integral of this model was implemented in a FE environment [180].

In this work, the near-tip field solutions and the deflection criteria are implemented in a plane of a 1D QC, which has only one quasiperiodic direction and is thus a special case among the subclasses of QCs. The QA can be perpendicular to the plane, leading to classic crystalline behavior in the plane. If the QA lies in the plane, different configurations are possible in regard to the initial crack. Two special configurations are taken into account in the simulations, i.e. the QA is parallel to the x_1- or x_2-axis. The relevant material constants of both cases are given in Appendix A.1. These configurations can also represent a planar problem of a 2D QC, which has two phason degrees of freedom, if one of the two QAs is in the plane and the other is not.

To eventually simulate a crack growth in QCs and predict crack paths, deflection criteria and the influence of the induced phason crack-tip loading are analytically investigated at first. Some computed results with different phonon–phason coupling constants and loading regimes are presented. Then, the numerical results of deflection angles based on different approaches and fracture quantities are compared, see Section 5.1.2. Applying the adaptive re-meshing algorithm, the crack paths in different numerical models under mixed-mode loading are presented.

5.1.1. Influence of the phason field on crack deflection

The selected crack deflection criteria are applied to a planar 1D QC with an initial crack for investigating the influence of the phason field on crack deflection. Since a directly applied phason loading is not possible, the phason field is induced by the phonon loading due to the coupling effect. The coupling coefficients are expected to have an impact on the crack tip loading by the induced phason stress. The most adopted coupling coefficients, however, are relatively small $(R_1/C_{1111} \approx 0.5\%)$ according to [45]. On the other hand, only a few quasicrystalline materials and their coupling constants have been investigated to date. The available constants are predominantly evolved from ab initio or molecular dynamics simulations [112], whereas an experimental confirmation is still lacking. Thus, the coupling coefficients have to be considered to be not quite reliable, whereupon a set of enlarged constants are additionally used to theoretically investigate the influence of the phason field.

Applying the criterion of maximum hoop stress first, the stresses in the near-tip field in the Cartesian coordinate system have to be transformed into the polar coordinate system, by using the transformation matrix Ω_{ij} according to Eq. (2.11). The hoop stress is then given as

$$\sigma_{\theta\theta} = \cos(\theta)\big(\sigma_{22}\cos(\theta) - \sigma_{12}\sin(\theta)\big) - \sin(\theta)\big(\sigma_{21}\cos(\theta) - \sigma_{11}\sin(\theta)\big), \quad (5.1)$$

where the stresses in the Cartesian coordinate system are inserted according to Eq. (3.36). The induced phason stress in the near-tip field is not considered in the criterion of maximum hoop stress, since only the phonon stress $\sigma_{\theta\theta}$ is assumed to determine the crack deflection. Nevertheless, the phonon–phason coupling effect has an impact on σ_{ij} in Eq. (5.1). The deflection angle $\bar{\theta}$ is determined by inserting the expression of $\sigma_{\theta\theta}$ into Eq. (3.88). Unfortunately, a closed-form solution, and thus, an explicit determination of $\bar{\theta}$ as a function of the K-factors is not available because of the complex quantities in the angular functions according to Eq. (3.38). The hoop stress and its first order derivative, however, can be plotted versus the angle if the K-factors are given, whereupon the deflection angle is determined by numerically identifying the root of the derivative. One example of a mixed-mode loading case is shown in Fig. 5.1, illustrating the hoop stress and its derivative around the crack tip. Since the absolute magnitude of hoop stress is not relevant for the deflection angle $\bar{\theta}$ according to Eq. (3.88), only the ratios of K-factors are given. The maximum of $\sigma_{\theta\theta}$ and the root of its derivative are found by using a numerical Newton-Raphson method from the starting point $\theta = 0$.

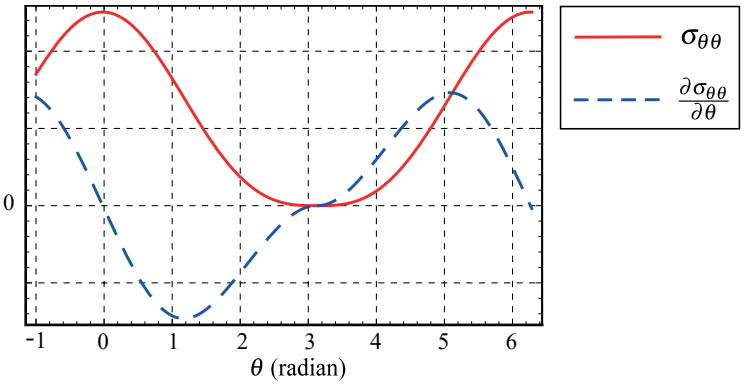

Figure 5.1.: The hoop stress and its first order derivative in the near-tip field of a crack in 1D QC under mixed-mode loading, where the QA is parallel to the crack face. The given K-factors have the relations $K_{II}^{\parallel} = 1\% K_I^{\parallel}$ and $K^{\perp} = K_I^{\parallel}$. The deflection angle in this loading case is -0.0197 rad $(-1.13°)$ [168].

Regarding the J-integral criterion of Eq. (3.90), the required magnitudes of J_1 and J_2 can be expressed by the K-factors according to Eqs. (3.55), (3.60), (3.76) and (3.77). For the selected 1D QC material, they are determined as

$$\begin{aligned} J_1 &= (5.1066\, K_I^{\parallel 2} + 5.1897\, K_{II}^{\parallel 2} - 0.08824\, K_{II}^{\parallel} K^{\perp} + 9.2413\, K^{\perp 2}) \times 10^{-12}, \\ J_2 &= -1.0213 \times 10^{-11}\, K_I^{\parallel} K_{II}^{\parallel} - 3.1194 \times 10^{-25}\, K_I^{\parallel} K^{\perp}, \end{aligned} \tag{5.2}$$

if the QA is parallel to the crack faces and

$$\begin{aligned} J_1 &= (5.1897\, K_I^{\parallel 2} + 5.1066\, K_{II}^{\parallel 2} - 0.08824\, K_I^{\parallel} K^{\perp} + 9.2413\, K^{\perp 2}) \times 10^{-12}, \\ J_2 &= -1.0379 \times 10^{-11}\, K_I^{\parallel} K_{II}^{\parallel} - 2.2198 \times 10^{-14}\, K_{II}^{\parallel} K^{\perp}, \end{aligned} \tag{5.3}$$

for the QA being perpendicular to the crack faces [206]. The material coefficients with the required characteristic matrices and eigenvalues are listed in Appendix A.1. The phason stress intensity factor $K^{\perp}$, as the only phason intensity factor in a 1D QC, is written without any subscript index.

Taking a look at the phonon–phason mixed terms in Eqs. (5.2) and (5.3), which include the phonon and phason stress intensity factors, it is obvious that the coefficients are significantly smaller in comparison with the other terms. For the first configuration in Eq. (5.2), the phason K-factor has scarcely an influence on J_2, whereas it might give some contribution to J_2 for the second configuration, where the coefficient related to $K^{\perp}$ is small but not negligible. However, it still essentially depends on the ratio of $K_I^{\parallel}$ and $K_{II}^{\parallel}$. For J_1, the impact of $K^{\perp}$ in both configurations is comparable to the one of the phonon K-factors and less by two orders in the mixed terms.

The calculated crack deflections $\bar{\theta}$ based on the introduced criteria are compared, see

loading		$K_I^{\parallel}$	$K_{II}^{\parallel}$	$K_{II}^{\parallel} = K^{\perp}$	$K_I^{\parallel} = K^{\perp}$	$K_{II}^{\parallel} = 1\% K_I^{\parallel}$	$K_{II}^{\parallel} = 1\% K_I^{\parallel}$ $K^{\perp} = 1\% K_I^{\parallel}$	$K_{II}^{\parallel} = 1\% K_I^{\parallel}$ $K^{\perp} = 10\% K_I^{\parallel}$	$K_{II}^{\parallel} = 1\% K_I^{\parallel}$ $K^{\perp} = 50\% K_I^{\parallel}$	$K_{II}^{\parallel} = 1\% K_I^{\parallel}$ $K^{\perp} = 100\% K_I^{\parallel}$
J-integral criterion	R^{ref}	0°	-	-	≈ 0°	−1.15°	−1.15°	−1.13°	−0.79°	−0.41°
	$50\times R^{ref}$	0°	-	-	≈ 0°	−1.15°	−1.15°	−1.12°	−0.72°	−0.34°
maximum hoop stress criterion	R^{ref}	0°	−71.03°	−71°	≈ 0°	−1.13°	−1.13°	−1.13°	−1.13°	−1.13°
	$50\times R^{ref}$	0°	−72.13°	−69.82°	≈ 0°	−1.19°	−1.18°	−1.18°	−1.18°	−1.17°

Table 5.1.: Comparison of crack deflection angles under different mixed-mode loadings where the QA is parallel to the crack faces [206].

loading		$K_I^{\parallel}$	$K_{II}^{\parallel}$	$K_{II}^{\parallel} = K^{\perp}$	$K_I^{\parallel} = K^{\perp}$	$K_{II}^{\parallel} = 1\% K_I^{\parallel}$	$K_{II}^{\parallel} = 1\% K_I^{\parallel}$ $K^{\perp} = 1\% K_I^{\parallel}$	$K_{II}^{\parallel} = 1\% K_I^{\parallel}$ $K^{\perp} = 10\% K_I^{\parallel}$	$K_{II}^{\parallel} = 1\% K_I^{\parallel}$ $K^{\perp} = 50\% K_I^{\parallel}$	$K_{II}^{\parallel} = 1\% K_I^{\parallel}$ $K^{\perp} = 100\% K_I^{\parallel}$
J-integral criterion	R^{ref}	0°	-	-	0°	−1.15°	−1.15°	−1.13°	−0.8°	−0.42°
	$50\times R^{ref}$	0°	-	-	0°	−0.96°	−0.97°	−1.07°	−1.02°	−0.53°
maximum hoop stress criterion	R^{ref}	0°	−71.32°	−71.33°	0°	−1.16°	−1.16°	−1.16°	−1.17°	−1.17°
	$50\times R^{ref}$	0°	−70.95°	−71.54°	0°	−1.07°	−1.07°	−1.09°	−1.15°	−1.24°

Table 5.2.: Comparison of crack deflection angles under different mixed-mode loadings where the QA is perpendicular to the crack face [206].

Tab. 5.1 for the QA being parallel to the crack faces and Tab. 5.2 for the QA being perpendicular. There are two rows for each deflection criterion, one showing the results based on the coupling constants according to Appendix A.1 denoted as $\mathrm{R}^{\mathrm{ref}}$ and the second row being based on 50 times enlarged coupling constants. The K-factors not explicitly given are zero, so the first two columns represent single mode loading conditions and the others are mixed-mode loadings. The J-integral criterion, basically being valid only if K_I is dominating K_{II} as shown in Fig. 3.10, was not applied in the loading cases $K_I^{\parallel} = 0$ and $K_{II}^{\parallel} = K^{\perp}$. The magnitude of $K^{\perp}$, whose influence on the validity of the J-integral criterion is still unknown, varies in a large range from 1% to 100% of $K_I^{\parallel}$. $K^{\perp}$ alone is not applied as the phason stress singularity at the crack tip is induced by the coupling effect under phonon loadings and a pure phason loading is not possible. Since the J-integral criterion demonstrates that a finite J_2 is indispensable for a crack deviating from its original direction, according to Eqs. (5.2) and (5.3) an additional mode-II loading is required. Thus, most of the considered loading cases in Tabs. 5.1 and 5.2 exhibit a phonon mixed-mode loading. The value of $K_{II}^{\parallel}$ was chosen two orders of magnitude minor compared to $K_I^{\parallel}$, being a typical loading condition along curved crack paths in an inhomogeneous stress field under constant external loading, e.g., for cracks near holes or inclusions [102]. In Tabs. 5.1 and 5.2 only ratios of K-factors are given, since their absolute magnitudes are not relevant for the deflection angles, which is demonstrated in Eqs. (5.2) and (5.3).

Just as in classical materials, there is no crack deflection under a pure mode-I loading regardless of the configuration and the coupling constant. A large phason loading, as shown in the fourth column, even with the same magnitude as $K_I^{\parallel}$, does not have any significant impact on the crack deflection. Considering the J-integral criterion at first, the predicted deflection angle under pure phonon mixed-mode loading is -1.15°. It is remarkable that an enlarged coupling constant, $50\times\mathrm{R}^{\mathrm{ref}}$, leads to a reduced deflection angle of 0.96° in the case of the QA being perpendicular to the crack. Although the influence of the coupling constant in Eq. (5.3) is not obvious, the material-dependent matrices in Eqs. (3.55) and (3.60) represent the relation of the J_k and the K-factors and thus the influence of the coupling coefficient is manifested in the coefficients in Eqs. (5.2) and (5.3). In Tabs. 5.1 and 5.2, the last four columns show the results of an increased $K^{\perp}$ superimposed by a phonon mixed-mode I/II loading, exhibiting a considerable reduction in the deflection angles. Eventually, the phason stress intensity factor shows a smaller influence on crack deflections than $K_{II}^{\parallel}$, since the coefficients associated with $K^{\perp}$ for J_2 in Eqs. (5.2) and (5.3) are much smaller and $K^{\perp}$ in the latter equation is multiplied by $K_{II}^{\parallel}$ instead of by the larger $K_I^{\parallel}$.

Compared to the J-integral criterion, the maximum hoop stress criterion allows the calculation of a crack deflection angle under pure mode-II loading. The predicted deflection angles $\bar{\theta}$ in this case are slightly larger than the value of isotropic materials ($\bar{\theta} = -70.5^{\circ}$ [48]), where no coupling effect is present. For the decoupled case of anisotropic elasticity (R=0, the phason field is thus irrelevant for the results), the deflection angles for the QA parallel and perpendicular to the crack are $\bar{\theta} = -71.03^{\circ}$ and $\bar{\theta} = -71.32^{\circ}$, respectively, being equal to the angles in the case of $\mathrm{R}^{\mathrm{ref}}$. If a phason stress intensity factor of the same magnitude is applied additionally, as shown in the

third column, no remarkable change of $\bar{\theta}$ is observed, only showing a deviation up to 3% by the enlarged coupling coefficients. In the mixed-mode I/II loading cases, the deflection angles of the maximum hoop stress criterion are very close to those predicted by the J-integral criterion, except for the last two columns, where $K^{\perp}$ approaches the magnitude of $K_I^{\parallel}$. In contrast to the J-integral criterion, a superimposed phason loading $K^{\perp}$ does not result in a notable change of $\bar{\theta}$ predicted by the maximum hoop stress criterion, unless the coupling constants are enlarged, in particular for a perpendicular QA.

From an energetic point of view, the J-integral criterion takes into account the energy contributed by the phason field and postulates the minimization of the total potential energy of QCs. It thus manifests a notable influence of the phason stress intensity factor when the enlarged coupling constants are employed. On the contrary, the maximum hoop stress criterion considers essentially the phonon field in the fracture process and thus predicts a minor impact of phonon–phason coupling on the crack deflection angle. Although deviations in deflection angles may be small in Tabs. 5.1 and 5.2, their accumulation at crack growth might lead to distinctly different crack paths. Numerical predictions and crack growth simulations are thus indispensable.

5.1.2. Numerical calculation of deflection angles

The deflection angle $\bar{\theta}$ in crack boundary value problems is calculated based on the selected crack deflection criteria by post processing of FE simulations. If the maximum hoop stress criterion according to Eq. (3.88) is applied, the deflection angle is determined inserting Eq. (5.1), employing the near tip solutions of generalized stresses σ_{Ij} based on the K-factors, see Eq. (3.27). To implement the J-integral criterion Eq. (3.90) in a crack growth simulation, the integrands of Eq. (4.32) have to be calculated along the outer contour Γ_a and the crack faces numerically, providing the J-integral and subsequently the deflection angle $\bar{\theta}$. Alternatively, the coordinates of J_1 and J_2 can be determined by the energy release rate G and the second energy term H as shown in Eq. (3.90). G and H are readily calculated by the crack closure integral according to Eqs. (3.55) and (3.60) with K-factors, which are provided from the CTE method, thus sparing the effort of implementing a contour integral.

If classical fracture behavior is considered, cracks will propagate straightforwardly under symmetric mode-I loading, where $H = -J_2 = 0$. An induced phason loading at the crack tip in QCs, where pure tensile load is applied, has only minor impact on J_2 due to the small coefficient in Eq. (5.2) or no influence at all according to Eq. (5.3). Hence, an inclined crack with remote tensile load is employed to investigate the numerical results from different approaches. The model is illustrated in Fig. 5.2, where the crack is inclined by 30° with respect to the x_1-axis and $K_{II}^{\parallel}$ is thus on the same level as $K_I^{\parallel}$. Three different sets of coupling constants, the reference value $\mathrm{R}^{\mathrm{ref}}$ and the enlarged values, are used in the calculations. Crack tip loading quantities, determined by both the CTE method in connection with the crack closure integral and the contour integral approach, are compared.

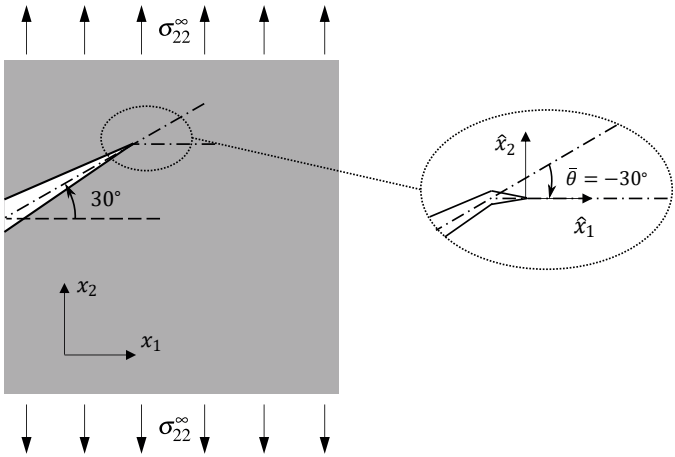

Figure 5.2.: Crack inclined by 30° with respect to the x_1-axis. A kink of $-30°$ is illustrated in detailed view.

The results are shown in Tab. 5.3. The deflection angles $\bar{\theta}$, stemming from (G,H) and (J_1,J_2), are listed in the second and fourth columns behind the related data. Both columns of the angles are determined by the J-integral criterion. Two cases with different QA directions are considered, one with the QA being parallel to the x_1-axis, the other being parallel to the x_2-axis. First of all, G and J_1 as well as H and $-J_2$ show almost equal values, which makes the calculation of (G,H) from the K-factors more attractive, avoiding the contour generation and the numerical integration, thus being advantageous in regard to computational cost. Comparing their magnitudes, the loading quantities are increased by the enlarged coupling constants due to the phason field and its influence on the free energy.

However, there is no remarkable change on the crack deflection angles in these three situations. All the values are in a small range around $-30°$, which indicates a crack extension almost perpendicular to the loading direction, see Fig. 5.2. The crack deflection angles in the case of a QA in the x_1-direction vary from $-30.7°$ to $-29.8°$, being slightly smaller in the other case, where a range of $-30.6°$ to $-29.5°$ is predicted. Although the deviation of the deflection angles is small, in fact, the differences may have a significant effect on the whole crack path according to the findings in conventional fracture mechanics, where a K_{II} being small compared to K_I prominently influences crack growth and leads to a curved crack path [102]. Therefore, a small induced phason stress intensity factor could also have a strong influence on the crack path at mixed-mode loading, where $K_I^{\parallel}$ is much larger than $K_{II}^{\parallel}$ and $K^{\perp}$.

	G/H	$\bar{\theta}(^\circ)$	J_1/J_2	$\bar{\theta}(^\circ)$
QA along x_1-axis				
$\mathrm{R}^{\mathrm{ref}}$	1.31/0.78	-30.7°	1.31/-0.77	-30.7°
$50 \times \mathrm{R}^{\mathrm{ref}}$	1.43/0.84	-30.5°	1.43/-0.84	-30.5°
$80 \times \mathrm{R}^{\mathrm{ref}}$	1.89/1.10	-30°	1.89/-1.09	-29.8°
QA along x_2-axis				
$\mathrm{R}^{\mathrm{ref}}$	1.33/0.78	-30.6°	1.36/-0.78	-29.8°
$50 \times \mathrm{R}^{\mathrm{ref}}$	1.52/0.89	-30.2°	1.50/-0.87	-30.1°
$80 \times \mathrm{R}^{\mathrm{ref}}$	4.34/2.48	-29.7°	4.15/-2.35	-29.5°

Table 5.3.: Results of the energy terms (G,H) [N/m] from the CTEM and (J_1,J_2) per unit thickness from the contour integral as well as the calculated crack deflections angles $\bar{\theta}$ corresponding to Fig. 5.2.

5.1.3. Crack growth simulations in QCs

The most interesting case, being characteristic for many crack growth problems, is a mode-I/II loading case with $K_{II}^{\parallel}$ being much smaller than $K_I^{\parallel}$. Hence, two models of numerical fracture mechanics are employed for obtaining the desired loading regime, see Fig. 5.3. The first model describes a double cantilever beam (DCB) specimen with asymmetric concentrated forces applied. The other model with external tensile loading has mixed-mode loadings at the crack tip due to the drilled hole located above the crack ligament. In both cases, $K_{II}^{\parallel}$ and $K^{\perp}$ are relatively small compared to $K_I^{\parallel}$. The specific ratios of the K-factors at the incipient crack position are given in Tab. 5.4 for the DCB model with the applied forces $F_2 = 0.99F_1$, illuminating the influence of the phonon–phason effect on the K-factors. The ratios $K^{\perp}/K_I^{\parallel}$ in the first configuration of QA along x_1-axis are close to zero, in fact, they are distinct from each other, being able to affect crack paths in the following. The crack growth is simulated using the adaptive re-meshing algorithm in the framework of the FEM. The crack paths are plotted in Figs. 5.4 and 5.5. Both CTEM and path-independent integral have been employed, see Section 5.1.2, providing the crack tip loading quantities for the J-integral criterion. Despite the slightly different deflection angles calculated for a single crack increment, as shown in Tab. 5.3, the results of the crack path prediction from both approaches do not visibly differ from each other. Therefore, the CTEM is used if no further indication is given.

In both Figs. 5.4 and 5.5, the solid red lines show the crack paths for R=$\mathrm{R}^{\mathrm{ref}}$. The results for $\mathrm{R} = 0$, representing crack paths in a classical crystalline material, are omitted because the crack paths almost coincide with the solid red lines. The dash-dotted green lines, representing the 50 times enlarged coupling coefficients, and the dotted blue lines for R=80×$\mathrm{R}^{\mathrm{ref}}$ are distinctly different from the red lines of $\mathrm{R}^{\mathrm{ref}}$.

Similar to crack paths in regular crystalline materials, a small $K_{II}^{\parallel}$ in mixed-mode loading conditions leads to a significantly curved crack path. For the QA being parallel to

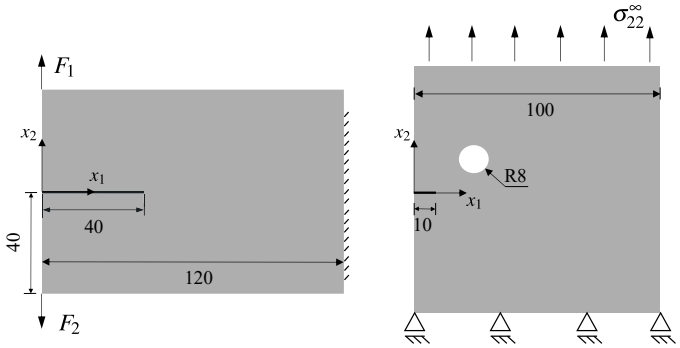

(a) (b)

Figure 5.3.: (a) Double cantilever beam (DCB) model with asymmetric loadings, (b) plate with a hole above the ligament under tensile loading. The QA is either in the x_1- or x_2-direction. The thick lines starting from the left edges are the incipient cracks.

	$K_{II}^{\parallel}/K_{I}^{\parallel}$	$K^{\perp}/K_{I}^{\parallel}$
QA along x_1-axis		
$\mathrm{R}^{\mathrm{ref}}$	0.3%	≈ 0
$50 \times \mathrm{R}^{\mathrm{ref}}$	0.3%	≈ 0
$80 \times \mathrm{R}^{\mathrm{ref}}$	0.3%	≈ 0
QA along x_2-axis		
$\mathrm{R}^{\mathrm{ref}}$	0.3%	0.3%
$50 \times \mathrm{R}^{\mathrm{ref}}$	0.3%	13.8%
$80 \times \mathrm{R}^{\mathrm{ref}}$	0.5%	20.6%

Table 5.4.: The ratios of the K-factors at the initial crack state of the DCB model.

the x_1-axis, the varied coupling effect does not lead to substantial changes in the crack paths. Only a slight enhancement of crack deflection by the increased coupling coefficients is exhibited in the DCB model, whereas the crack paths in the second model show a converse tendency. If the QA is the x_2-axis, the large coupling effect essentially compensates the influence of the shear effect, showing that the crack tends to grow along its ligament in both specimens. This effect, however, is strongly nonlinear with respect to the coupling constants. The similar nonlinearity in this configuration is also shown in Tab. 5.4, where the ratio $K_{II}^{\parallel}/K_{I}^{\parallel}$ for $80\times\mathrm{R}^{\mathrm{ref}}$ is much larger than the others.

The results based on the maximum hoop stress criterion show basically the same tendency, however, they differ quantitatively from the crack paths predicted by the J-integral criterion. For the sake of simplicity, only the crack path of $50 \times \mathrm{R}^{\mathrm{ref}}$ is illus-

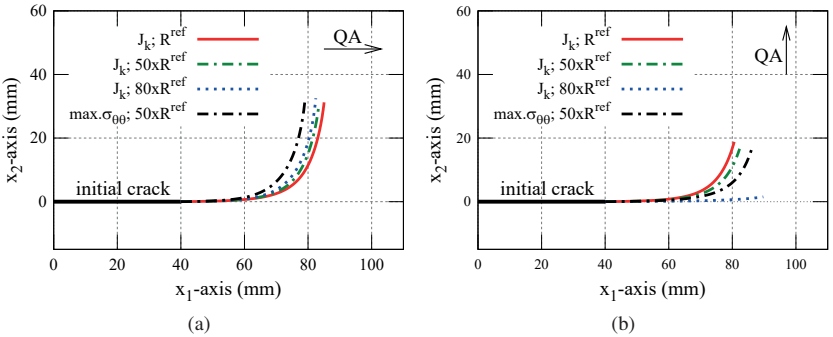

Figure 5.4.: Results of simulation for DCB model with the QA being (a) parallel to the x_1-axis and (b) parallel to the x_2-axis.

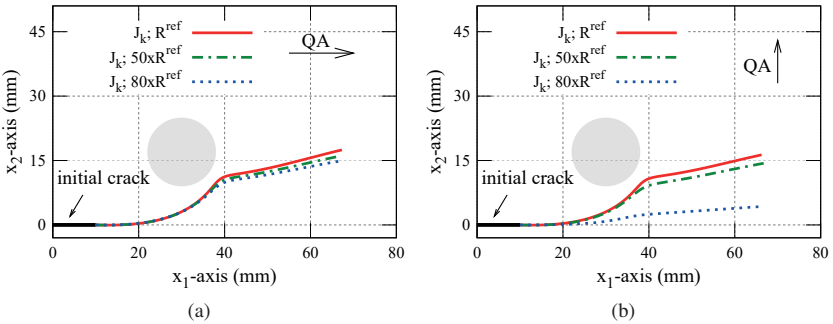

Figure 5.5.: Results of simulation for plate under tensile loading with a hole above the ligament and the QA being (a) parallel to the x_1-axis and (b) parallel to the x_2-axis. The gray circle indicates the hole.

trated in each graph in dash-dotted black line.

As reliable data of a coupling coefficient are still hard to get hold of, probably because of experimental limitations, different magnitudes of the phonon–phason coupling coefficients have been employed here to investigate in principle the effect of phonon–phason coupling. Being capable of accurately simulating crack paths in QCs gives rise to the idea of inversely determining coupling coefficients based on crack growth experiments in specimens akin to those presented here. Due to technical issues, still restricting specimen sizes to just a few millimeters, this approach, however, remains visionary.

5.2. Crack paths in piezoelectrics

The crack growth in piezoelectrics, in particular, under combined mechanical and electric loading has been simulated hitherto with different approaches, investigating e.g. the influence of the electric field. In [94] finite element simulations with linear piezoelectric constitutive behavior and an adaptive re-meshing algorithm provide crack paths in three-point bending specimens with different notch positions. The boundary element method and also a linear constitutive model in [121] yield similar results, which are just roughly accordant with the experimental crack paths in [153]. In both works, the anisotropic fracture toughness is taken into account in a simplified manner, assuming that there is a globally homogeneous polarization even in the fracture process zone. A saturation strip model considering a linear mechanical field and a nonlinear electric field in front of the crack tip is suggested in [128], whereupon the experimental crack path in [153] is well reproduced, however, only if a calibration parameter of this model is appropriately chosen. All these simulations employ the maximum hoop stress criterion to predict crack deflection angles, where electric fields scarcely show an influence on crack paths and the results thus only depend on the mechanical load. An energy density criterion, on the other hand, has been applied to crack growth simulation in an infinite piezoelectric plate under mixed-mode loading, showing the influence of electric fields [72]. In this thesis, a modified J-integral criterion accounting for the mechanical part of the configurational force, has been applied and compared with experimental results of the three-point bending specimens outlined in Chapter 6 and [205].

First of all, a DCB model with the same geometry as in Fig. 5.3(a) is constructed for crack growth simulations in the piezoelectric material $BaTiO_3$. The favored configuration for crack problems in piezoelectrics is a specimen with homogeneous polarization being perpendicular to the crack. A positive electric field indicates that the electric field has the same direction as the poling, while a negative electric field acts against the poling direction. Two loading conditions, pure mechanical loading and combined mechanical/electric loading, are incorporated in the crack growth simulations, where the applied electric field of 100 V/mm corresponds to $0.5E_c$ for $BaTiO_3$ [61]. The concentrated forces depicted in Fig. 5.3(a) are $F_1 = 40$ N and $F_2 = 95\%F_1$, inducing $K_I = 1.1\text{MPa}\sqrt{\text{m}}$ at the incipient crack tip, which is in the regular order of the fracture toughness of ceramic materials.

The predicted crack paths are plotted in Fig. 5.6. The simulations are based on the material constants given in Appendix A.2. The solid lines show the results under pure mechanical loading, where the crack path based on the J-integral criterion according to Eq. (3.90) exhibits a smaller deflection than the one calculated with the maximum hoop stress criterion. The modified J-integral criterion according to Eqs. (3.91) and (3.74), neglecting the electrical part of the configurational force and thus labeled J_k^m, shows the identical path of the J-integral criterion, since the electric energy part induced by the coupling effect is too small to have an impact on the crack path. If an electric field is superimposed, the crack paths show significant changes. The red-dashed line and the blue line, based on the maximum hoop stress and the modified J-integral criteria,

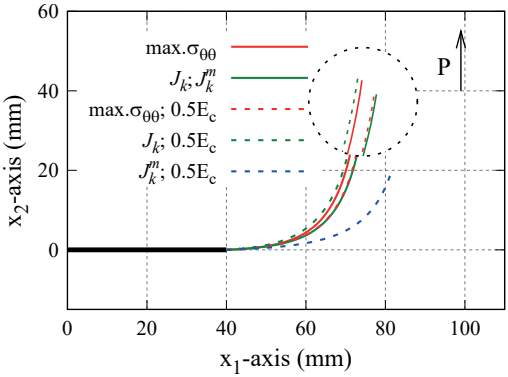

Figure 5.6.: Results of simulations in the $BaTiO_3$ DCB model with the poling in x_2-direction. A zoomed-in view is provided for the lines close to each other.

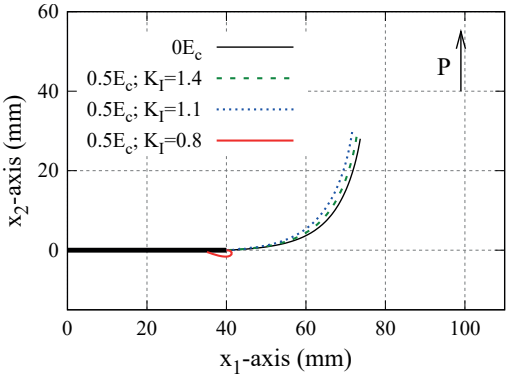

Figure 5.7.: Results of simulation based on the J-integral criterion in $BaTiO_3$ DCB model.

respectively, manifest a reduced shear effect, showing a smaller deflection, however, to distinctly different extents. On the contrary, the green-dashed line based on the classical J-integral criterion obviously predicts a larger deflection due to the superimposed electric loading.

The J-integral criterion, however, yield an unreasonable crack path, if other loading conditions are applied. Fig. 5.7 depicts crack paths determined by the J-integral criterion based on the total electromechanical energy according to Eq. (3.90) under different loading combinations, in particular, various mechanical loads. Without an applied electric load, the absolute magnitude of the concentrated force does not have an influence on the crack path, the black line thus represents the crack path of any mechanical load with the ratio $F_2 = 0.95F_1$. Under the combined loading conditions, a constant $0.5E_c$ is superimposed with three different mechanical loads. Two of them, $K_I = 1.4$

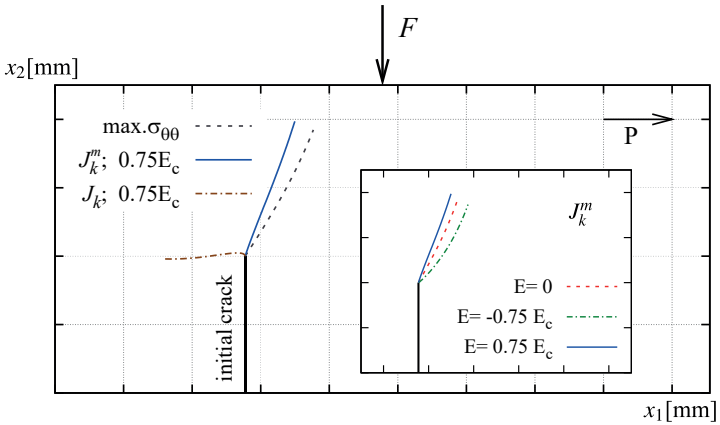

Figure 5.8.: Results of PZT-5H three-point bending test model calculated based on different deflection criteria. The magnitudes of loads are taken from Tab. 6.1. The floating figure illustrates the crack paths determined by the J_k^m-vector criterion with different electric loadings.

and 1.1MPa$\sqrt{\text{m}}$, provide similar crack paths. In contrast, if $K_I = 0.8\text{MPa}\sqrt{\text{m}}$ is applied, the crack turns around almost immediately after it starts to propagate, which is not a plausible crack growth. This result is due to the electric displacement intensity factor K_{IV}, which is mainly induced by the electric field and affects the energy release rate G and the second energy term H disproportionately, especially in the case of small K_I. Hence, the J-integral criterion causes an irrational deflection angle and is deemed invalid, if the electric loading is not negligible.

For the sake of comparison with experiments, see Chapter 6, the following simulations were carried out on a three-point bending test model with an off-center initial crack, see Fig. 5.8. The concentrated force is applied at the top middle position of the specimen, inducing a mode-I/II crack tip loading. At the bottom, the model is mechanically fixed in the x_2-direction. Different electric potentials are defined on the left and right edges of the model for applying an electric field. The homogeneous polarization in the x_1-direction is perpendicular to the initial crack. Three loading conditions are taken into account, i.e., pure mechanical loading without an electric field and mechanical loading with an electric field parallel or anti-parallel with respect to the direction of polarization. The applied mechanical and electric loading combinations are critical, taken from the experiments in Chapter 6. An anisotropy of crack resistance is neglected.

The crack paths based on three deflection criteria, the J_k- and J_k^m-vector criteria as well as the maximum hoop stress, are compared in Fig. 5.8. The gray-dashed line based on the maximum hoop stress criterion represents the crack paths under all three loading conditions, being independent of the electric load. The angular functions of the near tip solution under electromechanical loading, see Eqs. (3.38), do not depend on the electric field [164], whereas K_I, K_{II} vs. K_{IV} are the weights of the mechanical and

electrical contributions to $\sigma_{\theta\theta}$. K_{IV}, typically being in the order of 10^{-3} $\mathrm{Cm}^{-3/2}$ if the electric field is in the same order of E_c, thus gives rise to an electrical contribution not greater than $10^{-2} - 10^{-3}$ of mechanical contribution. In comparison with the crack path predicted by the J_k^m-vector criterion of Eq. (3.91), the crack path from the maximum hoop stress criterion shows a larger deflection for a positive electric field. The dash-dotted brown line, representing the crack path from the J-integral criterion based on the total electromechanical potential energy according to Eq. (3.90), reveals a non-physical crack path under the loading condition with $0.75E_c$.

A closer look at the crack paths of the J_k^m-vector criterion is given in the floating graph in Fig. 5.8, showing that positive electric loading results in a smaller crack deflection and negative electric loading in a larger one. These predictions are qualitatively confirmed by the simulations based on the energy density deflection criterion, where a crack model in an infinite piezoelectric plate under mode-I/II/IV loading is employed [72].

5.3. Crack paths in piezoelectric 1D QC

Accounting for different phonon–phason coupling coefficients and a superimposed electric loading, crack paths in a 1D QC with piezoelectric property are predicted. A DCB model with the same geometry of the foregoing simulations as depicted in Fig. 5.3(a) is employed. The QA is parallel to the polarization state of the model, i.e., in the x_2-direction. The asymmetric forces, $F_1 = 50$ N and $F_2 = 0.95F_1$, induce a phonon mode-I stress intensity factor in the order of $1\mathrm{MPa}\sqrt{\mathrm{m}}$, whereupon the $K_{II}^{\parallel}/K_I^{\parallel}$-ratio is about 1.5% for the initial crack.

Fig. 5.9 illustrates the crack paths for the reference phonon–phason coefficient $\mathrm{R}=\mathrm{R}^{\mathrm{ref}}$ as well as for the enlarged coefficients $\mathrm{R}=50\times\mathrm{R}^{\mathrm{ref}}$ and $\mathrm{R}=80\times\mathrm{R}^{\mathrm{ref}}$. The crack deflection angles are determined by the maximum hoop stress criterion and the $J_k^m(J_k)$-vector criterion, respectively. The J_k- and J_k^m-vector criteria yield identical crack paths because the electrical part of J_k is negligible if no electric loading is applied. Compared to the crack paths shown in Fig. 5.4(b) with the same QA, Fig. 5.9 demonstrates a similar outcome, in so far as a large coupling coefficient significantly reduces crack deflection. This reduction, however, is larger predicted by the maximum hoop stress criterion than by the J_k^m-vector criterion.

If a positive electric loading is superimposed, the predicted crack paths are generally less deflected, see Fig. 5.10. Along with that, the maximum hoop stress criterion seems to be less affected by the electric loading than the J_k^m-vector criterion, showing a comparatively smaller deviation between the crack paths. This agrees with the conclusions for piezoelectric materials according to Fig. 5.6. The classical J-integral criterion is not considered here, since the loading combination of the electric field of $0.5E_c$ with the mechanical loading of $K_I^{\parallel} = 1\mathrm{MPa}\sqrt{\mathrm{m}}$ may lead to a non-physical crack path as shown in Fig. 5.7.

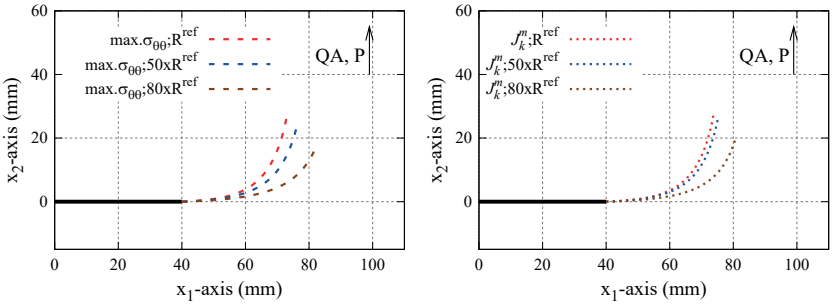

Figure 5.9.: Results of crack growth simulations in piezoelectric 1D QC with different phonon–phason coupling coefficients and deflection criteria.

	$\mathrm{R}^{\mathrm{ref}}$	$50 \times \mathrm{R}^{\mathrm{ref}}$	$80 \times \mathrm{R}^{\mathrm{ref}}$
$E = 0$	0.27%	14%	22%
$E = 0.5E_c$	0.24%	12%	8%

Table 5.5.: $K^{\perp}/K_I^{\parallel}$-ratios of the initial crack in the DCB model.

Although there is no direct coupling relation between the phason and electric fields, whereupon the coupling terms are zero in Eq. (4.11), these two fields are interconnected via the phonon field similar to the magnetoelectric coupling phenomenon shown in a ferroelectric–ferromagnetic composite [11]. Tab. 5.5 shows the $K^{\perp}/K_I^{\parallel}$-ratio for the initial crack tip in the DCB model influenced by the electric loading. A deviation of about 10% arises due to the additional $0.5E_c$ for $\mathrm{R}^{\mathrm{ref}}$ and for $50 \times \mathrm{R}^{\mathrm{ref}}$. In the case of $80 \times \mathrm{R}^{\mathrm{ref}}$, the electric field results in a drop of more than 50%.

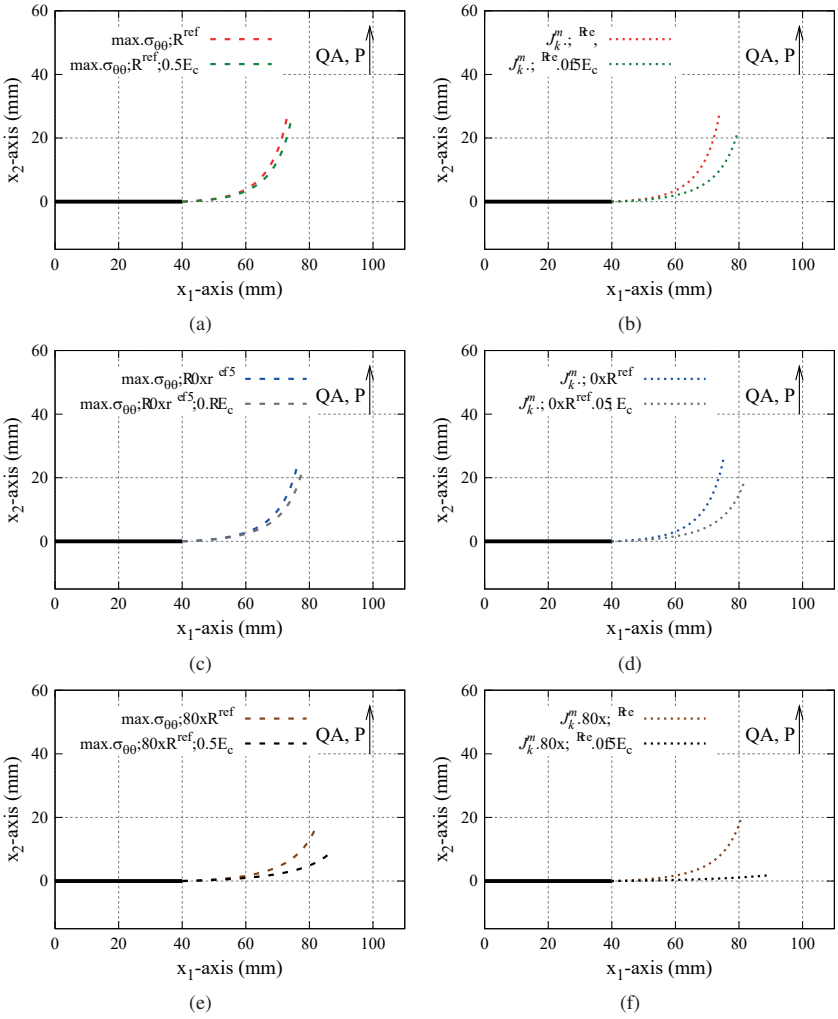

Figure 5.10.: Results of simulations in piezoelectric 1D QC. Each figure illustrates a comparison of the crack paths with and without electric loading. The dashed and dotted lines represent the results of the maximum hoop stress and the J_k^m-vector criterion, respectively.

6. Mixed-mode crack growth experiment

A host of fracture testing procedures have been developed for providing fracture parameters of classical structural materials and other experimental conclusions to improve and validate analytical methods, which facilitates the understanding of fracture behavior. Unfortunately, there are not many fracture testings and findings in QCs due to the current development of specimen production. One indentation test for the measurement of the fracture toughness of a 2D decagonal QC ($Al_{65}Cu_{20}Co_{15}$) has been reported, whereas the measurement was based on an empirical formula and thus might be deficient [50]. No further experiment is conducted hitherto in QCs with respect to fracture mechanics. Concerning ferroelectrics, an enormous amount of experiments has been carried out to explore the impact of the ferroelectric properties on fracture behavior, e.g., the influence of electric loading and the ferroelectric domain switching effect. Most of the experiments measure the fracture loading quantities and determine the critical values with associated crack growth criteria. Crack deflections and crack paths affected by electric fields, however, can only be found in a few references, e.g., [36, 153, 205].

In this chapter, the focus is on experiments in ferroelectric materials, in particular, the influence of electric fields on crack deflections. A review of experimental works is provided at first, rendering some major conclusions and the state of the art. A series of three-point bending tests employing the ferroelectric material PZT-5H is presented to provide statistically evaluated results of experimental crack paths, investigating the influence of both positive and negative electric fields below E_c on the crack deflection. Different specimens and loading configurations were critically reflected prior to the experiments with the aim to obtain curved crack paths under pure mixed-mode mechanical loading on the one hand side and to efficiently impose an influential electric field below the coercive field on the other. In this context, the three-point bending test set-up turned out to be the most appropriate one. The results of the experimental findings are discussed and compared to the numerical outcomes from the simulations in Section 5.2. This experimental work has been published in [205].

6.1. A short review of experimental works

The experiments in ferroelectrics focus basically on two essential classes of materials, lead zirconate titanate (PZT) and the lead-free barium titanate (BT), the latter

class becoming more popular due to the environmental compatibility. The fracture toughness has been measured by Vickers indentation tests in [30, 63, 134], manifesting isotropic fracture behavior in the unpoled ferroelectrics and anisotropy in the poled ferroelectrics. A crack in the poled ferroelectrics, being perpendicular to the poling direction, is longer than the crack in the unpoled ferroelectrics, while a crack in the parallel direction to the poling is shorter. This anisotropic fracture toughness is due to the tensile or compressive stresses, which are primarily induced by the domain switching effect in the fracture process zone [56, 74, 171]. These lead to a reduced macroscopic toughness for perpendicular cracks with respect to the poling direction and an enhanced fracture toughness for parallel cracks. The influence and mechanism of the domain switching at crack tips induced by external loadings has been investigated by using scanning electron microscopy and X-ray technique in [57, 80]. Based on a series of Vickers indentation tests [196] and compact tension tests [153], an additional electric loading changes the anisotropic ratio of the fracture toughness in the poled ferroelectrics, leading to a longer crack in the perpendicular direction under positive electric field and shorter under negative electric field, however, having very little influence on the crack length in the parallel direction. The same effect of electric loading on the crack growth in the perpendicular direction was observed from central cracked specimens in [55]. Nevertheless, a completely reverse conclusion has been reported in [202], which was again based on Vickers indentations. Some other tests, however, revealed that both positive and negative electric fields reduce the fracture toughness by applying a large indentation load, no matter if applied parallel or perpendicular to the crack [64, 65, 171, 191]. According to a series of three-point bending tests [205], the similar conclusion was drawn from the measured critical loadings for pure mechanical and combined electromechanical loadings with positive or negative electric fields. Crack growth driven only by pure cyclic electric loading of different magnitudes in PZT and lead lanthanum zirconate titanate (PLZT) was experimentally and theoretically investigated [23, 131]. In a further test [210], a mechanical loading was superimposed and an exponential crack growth law based on the electric displacement intensity factor was suggested.

Many other ferroelectric-related properties and factors have also been investigated to reveal their influences on fracture behavior. The impact of the permittivity of the crack interior on crack propagation has been studied in [64, 98] and in an indentation test [170] the relative electric permittivity $\kappa_r = 40$ was determined as an equivalent dielectric constant of the crack-filling medium. Some works focus on the influences of grain size and poling direction, in particular, on the crack resistance curve (R-curve), whereupon the toughing effect increases with the grain size and a poling parallel to the crack front exhibits the largest fracture toughness all along the R-curve [37, 111]. In the tests on DCB specimens in [116, 165], the crack resistance has been measured under pure mechanical and combined electromechanical loading along the poling direction, which is perpendicular to the crack. The R-curves were thereby presented and the results reveal that a positive electric field above the coercive field shifts the R-curve to larger values of the fracture toughness. Some environmental factors, e.g., temperature and humidity, can also affect the fracture behavior in ferroelectrics and have thus been investigated [145, 175]. A further experiment indicates that an unstable crack propaga-

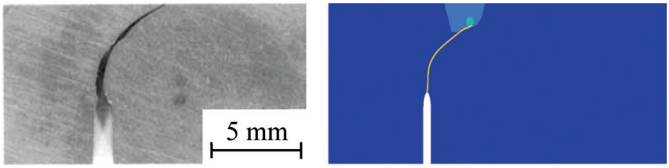

Figure 6.1.: (a) The crack path of a three-point bending specimen cracked under mode-I/II/IV loading [153] and (b) a crack growth simulation result [128].

tion can be triggered by a temperature rise, which promotes domain switching and vice versa, particularly in the vicinity of the crack tip [26]. A more comprehensive overview on experiments in ferroelectrics can be found in diverse review papers [6, 169, 208].

Crack deflection and crack path prediction in ferroelectrics, however, have been rarely studied. In [36] crack paths in PZT ceramics, driven by a continuously increased electric field, induced by a pair of electrodes only partly covering the specimen, are investigated both experimentally and numerically, primarily studying the influence of the width of the electrodes. A three-point bending test presented in [153] is probably one of the most essential experiments on the topic of crack paths, where a PZT-4 specimen with an eccentric notch position was employed for attaining a curved crack path under mechanical mixed-mode loading and an electric field, see Fig. 6.1(a). Unfortunately, a comparison with crack paths under other electric loading conditions and repeated experiments providing data for a statistical analysis are missing, whereas the crack paths of just one single specimen per notch position under the same electric loading are included in [153]. A solid conclusion about the influence of electric fields on crack deflection can thus not be provided. Nevertheless, the crack path shown in Fig. 6.1(a) has still served as a reference for the few numerical simulations available to date, e.g., the simulations on the bending test specimen with linear piezoelectric behavior using the FE method [94] or the boundary element method [121], providing just a rough accordance. The experimental crack path in [153] is well reproduced by an electric displacement saturation model presented in [128], where a nonlinearity in front of the crack tip is considered, however, a calibration parameter of the model must be appropriately chosen, see Fig. 6.1(b).

The experimental work presented in the following subsections uses a similar bending test set-up and provides statistically evaluated results of experimental crack paths, illuminating the influence of positive and negative electric loading below E_c on the crack deflection [205]. Moreover, a high-speed camera recording reveals unexpected details of crack initiation and propagation.

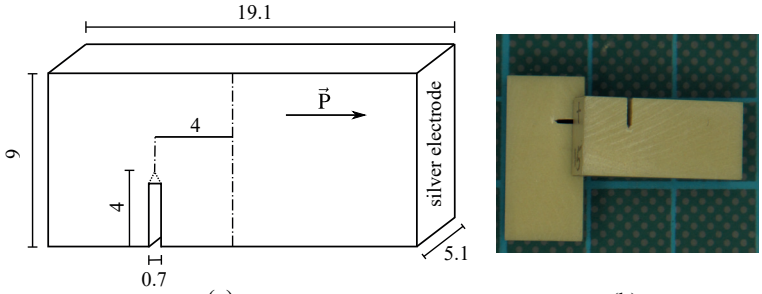

Figure 6.2.: (a) Specimen for the electric–mechanical mixed-mode fracture test (units in mm). The thin dotted lines at the root of the primary notch indicate the sharpened notch tip. (b) Two prepared specimens with notches [205].

6.2. Experimental set-up and testing procedure

The non-symmetric three-point bending test set-up according to [153] is employed in the present experiments, where the initial crack is not aligned with the mechanical loading axis. This configuration provides the favorable mixed-mode loading condition conveniently induced by only one loading degree of freedom, leading to a curved crack path. Fig. 6.2(a) shows the geometry of the three-point bending specimens. In contrast to [153], PZT-5H was used instead of PZT-4 and the material constants are listed in Appendix A.3. The plates (provided by the Institute of Acoustics, Chinese Academy of Sciences) of dimensions $19.1 \times 9 \times 5.1$ mm with an average grain size of 4 μm were poled in silicon oil in order to avoid an electric arc. An electric field of 3000 V/mm, which is much larger than the coercive electric field, was applied along the longest edge of the specimens to obtain a homogeneous polarization state. The left and right surfaces of the specimens are coated with silver electrodes (melting point at 961.78°C), which were sintered at 700°C. From the viewpoint of Fig. 6.2(a), the poling direction is from left to right, as $\vec{\mathrm{P}}$ shows. The eccentric notch, with a width of about 0.7 mm and an approximate depth of 3.7 mm, is perpendicular to the poling direction and was cut by a wheel cutter and polished. A common procedure to introduce a crack from a notch is subjecting a cyclic subcritical load. However, it is unfeasible for the present specimens due to the eccentric notch position. Thus, at the root of the primary notch, a thin slit was subsequently made by a surgical scalpel of 0.1 mm thickness to facilitate crack initiation. The total final length of the sharpened notch is 4 mm. A photograph of two prepared specimens is shown in Fig. 6.2(b).

The specimens for the tests with electric loading need extra preparation. Two wires were separately glued on the silver electrode surfaces with an electrically conducting polyurethane adhesive (PU 1000, Polytec PT, hardening at room temperature). The wires are connected with the output of a Trek Model 10/40A-HS amplifier, which generates a constant voltage of 10 kV, corresponding to $E = \pm 0.75 E_c$ for the PZT-5H specimens. During the experiments involving an electric loading, the specimens were

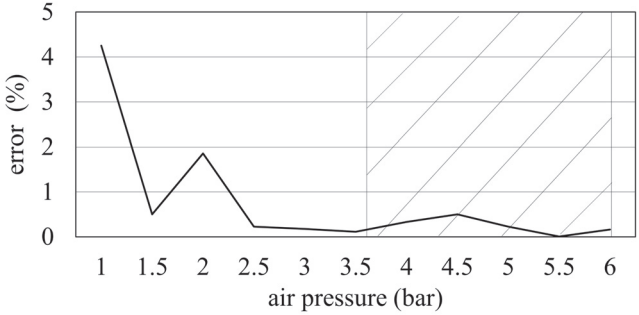

Figure 6.3.: Calibration of the applied force. The error of the applied force from the piston rod measured with a pressure gauge is given and the hatched area indicates the range of operation [205].

submerged in silicon oil in an acrylic glass container for insulation.

A double-acting pneumatic cylinder, fixedly installed on a stable test platform, generates the force-controlled mechanical loading in vertical direction. The piston rod of the cylinder is powered by compressed air pumped into the cylinder from the upper port, thus moving downwards. Comparing to a single-acting pneumatic cylinder, the double-acting pneumatic cylinder does not have a restoring spring, whereupon the piston rod transfers constant force for any position if the air pressure remains constant and the bottom port is unimpeded. The circular effective area of the cylinder has a diameter of 25 mm, indicating a force increment of 49.1 N per 1 bar. The mapping between the pressure gauge and the force has been calibrated, see Fig. 6.3. The error is smaller than 1% if the air pressure is larger than 2.5 bar, which corresponds to approximately 123 N. Based on the mechanical energy release rate criterion, the critical fracture loads have been estimated, which are much larger than 123 N. The schematic arrangement of the experimental set-up under combined electromechanical loading and a photograph of the mechanical loading unit are shown in Fig. 6.4. Fig. 6.5(a) illustrates the mechanical loading procedure without applied electric field and Fig. 6.5(b) shows the broken specimen at the end of the experiment.

A displacement-controlled loading unit for a stable crack growth is challenging for this test. The required displacement at the loading point demands extremely precise control due to the small displacement increment according to the geometry of the specimens. Based on the fracture criterion of the mechanical energy release rate introduced in [153], the increment of the applied displacement should be in the order of 1 μm for obtaining a controllable crack growth process.

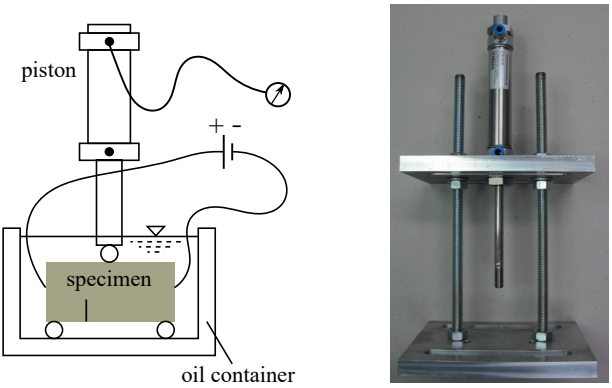

(a) (b)

Figure 6.4.: (a) Working principle of three-point bending test, (b) loading frame for the mechanical force [205].

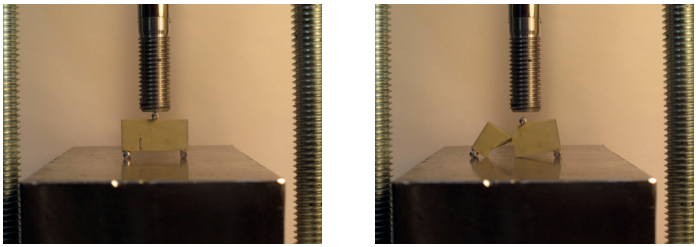

(a) (b)

Figure 6.5.: Specimen without electric loading and (a) piston rod with a remaining 1 mm stroke length, (b) spontaneously broken specimen after critical load has been attained [205].

6.3. Crack paths of three-point bending specimens

6.3.1. Comparison of the crack paths under different loading configurations

Three different loadings were implemented, i.e., pure mechanical load and mechanical load with an additional electric field parallel or anti-parallel with respect to the poling direction. For each loading condition, five specimens have been prepared and tested. The specimens were subsequently scanned by a high-resolution scanner and the crack paths were extracted from the pictures. All the crack paths of the 15 tested specimens, scanned from the front and back sides, are illustrated in Fig. 6.6 and the averaged crack paths based on five tests of each case with error bars are shown in Fig. 6.7.

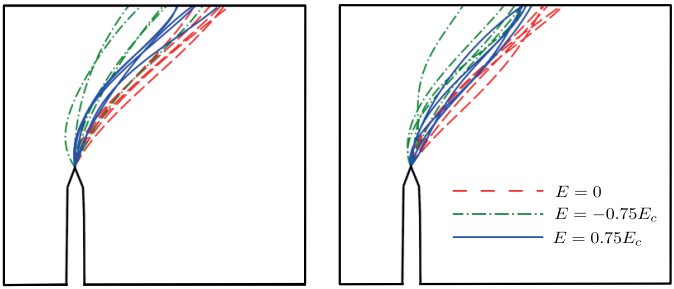

Figure 6.6.: Crack paths of three-point bending tests under different electric loading conditions, (a) view from the front sides and (b) view from the back sides of the specimens.

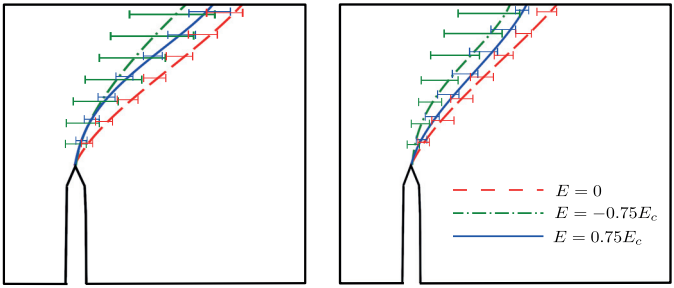

Figure 6.7.: The crack paths averaged from five tests for each electric loading condition and the associated error bars: (a) view from the front side, (b) view from the back side of the specimen.

The cracks under pure mechanical loading, in general, propagate with a larger deflection angle, see Fig. 6.6. Electric fields, in both parallel and anti-parallel directions, reduce the deflection, however to different extents. The crack paths of specimens under the additional negative electric field, compared to those under the positive electric field, have a smaller deflection. This tendency is also confirmed by the critical mechanical loads of crack initiation, where averaged values 272.4 N, 249 N and 200.6 N correspond to $E = 0$, $E = 0.75E_c$ and $E = -0.75E_c$, respectively. The critical mechanical loads for the individual specimens are listed in Tab. 6.1. The electric field in anti-parallel direction ($E = -0.75E_c$), which leads to the least deflection, is coming up with the largest scattering and is thus manifested in the longest error bars. The large scattering is probably due to the domain switching near the crack tip induced by the negative electric field. The electric load of $\pm 0.75E_c$ is expected to be large enough to show influence on the fracture behavior, however will not exceed the coercive field, retaining the general polarization state of the specimens. Nevertheless, the electric field

	$E = 0$	$E = 0.75E_c$	$E = -0.75E_c$
specimen 1	282	270	187
specimen 2	266	251	216
specimen 3	282	241	177
specimen 4	266	266	197
specimen 5	266	216	226
average	272.4	249	200.6

Table 6.1.: Critical mechanical loading force (unit in N).

near the crack tip is definitely beyond the switching barrier due to the singularity at the crack tip, thus inducing domain switching. The domain switching arises predominantly in the negative electric loading cases, where the domains initially are arranged against the electric field. Hence, the negative electric field makes the fracture process more unstable and promotes the diversity of the crack paths.

The experiment in [153] provided a crack path of a three-point bending specimen with the same geometry of the present tests. However, only one single result for the chosen notch position is available, which was subjected to a positive electric field. Although not all the details of the tests are identical, e.g., the employed material and the applied electric field, PZT-5H and $0.75E_c$ in this work, PZT-4 and about $0.33E_c$ in [153], a qualitative comparison is at least allowed after all. Fig. 6.8(a) shows the crack path from [153], which first deflects to the left side of the notch and continues with a curved path towards to the loading position. In contrast, the averaged crack paths from the front and back sides of the current experiments under the positive electric field are distinctly less curved, having similar deflection angles at the onset stage and being close to each other during crack growth.

The crack path of the simulation applying the J_k^m-vector criterion, taken from Fig. 5.8, is compared with the experimental crack paths of $E = 0.75E_c$ in Fig. 6.8(b). The three paths show very similar initial kinking angles and continue propagating in the similar direction. The curvatures of the experimental results, however, are larger than the one from the simulation, thus the divergence increases at further growth.

The discrepancy of simulation and experiment in Fig. 6.8(b), although fundamentally smaller than from comparison with the experimental result of [153], is supposed to be mainly due to two aspects, which have been disregarded so far in the model. Nonlinear ferroelectric and ferroelastic phenomena, leading to inelastic stress and polarization switching in a crack tip process zone, may substantially affect the stress state at the crack tip. In particular, the shear stress induced by the nonlinear phenomena might effectuate a non-negligible contribution to crack deflection. Another important factor related to this issue is, the fracture toughness anisotropy of ferroelectrics. Many experimental works confirmed that a considerable anisotropy of crack resistance prevails in ferroelectrics, e.g., as shown in the Vickers indentation tests [171, 196]. The impact of anisotropic fracture behavior on the curvature of cracks and even qualitative features of crack paths was shown to be crucial in [105, 106], where crack paths in a

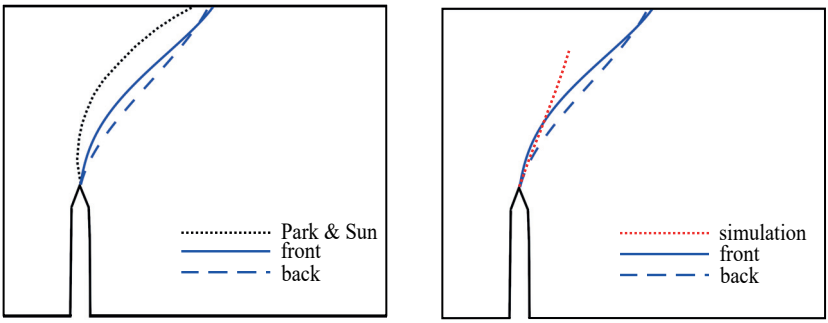

(a) (b)

Figure 6.8.: Comparison of the averaged crack paths for $E = 0.75E_c$ on both sides of PZT-5H specimens from the current experiments and (a) the crack paths (designated as Park & Sun) from [153] and (b) the crack path from simulation applying the J_k^m-vector criterion.

rolled aluminum alloy with smaller anisotropy ratio and short fiber reinforced polymer matrix composites with larger ratios, respectively, have been investigated. In principle, anisotropy of crack resistance has been considered in some numerical works [94, 121], however, assuming a constant polarization state and axis of anisotropy in the whole specimen. Local polarization reorientation induced by the crack tip loading and the resulting modification of anisotropy have been neglected.

6.3.2. High-speed recording of a crack growth process

Since crack growth in the three-point bending test is unstable under the force-controlled loading regime, the crack length is not controllable and a critical loading instantaneously leads to spontaneous failure. In order to observe the crack growth, a high-speed camera system was used for recording the crack propagation of one of the tests under pure mechanical loading, where the optically obstructive acrylic glass with silicon oil was removed. The high-speed camera recorded 65100 frames per second, focusing on a small area of approximately 1 cm^2, including the crack tip and the loading position. Six of the recorded frames are selected and shown in Fig. 6.9.

A notable feature revealed by the recording is that before the crack starts to initiate and propagate from the sharpened notch tip, which is supposed to take place as soon as the mechanical load is sufficiently large, a white line is formed and denoted as pre-fracture line in Fig. 6.9(b). After its appearance the white line is arrested for a short time, about 0.3 s, then it rapidly grows further towards the upper boundary of the specimen, see Fig. 6.9(c). Immediately after the white line reaches the boundary, the actual crack initiates and the subsequent crack path exactly follows the white line, see 6.9(d)-(f). The crack takes about 1.5×10^{-4} s from initiation at the notch tip to grow to the upper boundary, whereupon an average propagation speed of 42 m/s is identified.

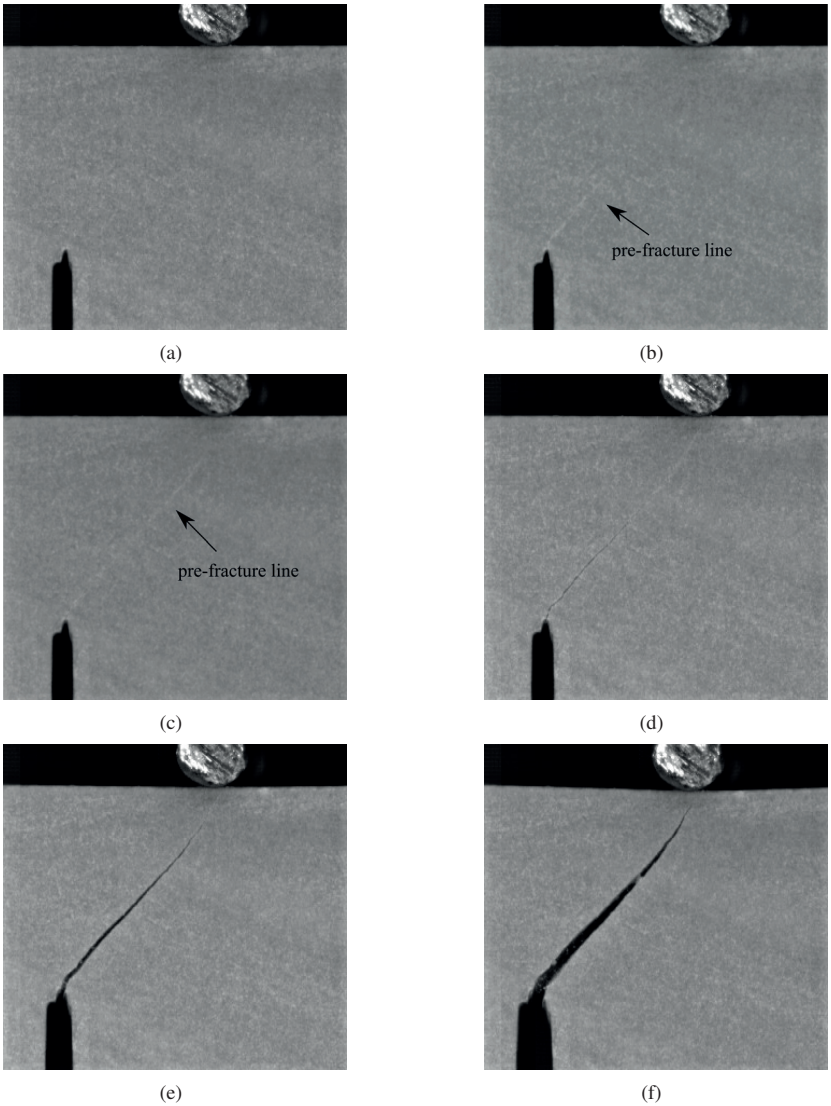

Figure 6.9.: Six stages of the high-speed recording of a specimen subjected to pure mechanical loading: (a) loaded specimen prior to cracking, (b) increasing the applied force, a white line appears in front of the notch tip (indicated as pre-fracture line), (c) after a 0.3 s arrest the white line continues propagating, (d)-(f) a crack initiates from the notch tip and propagates along the white line [205].

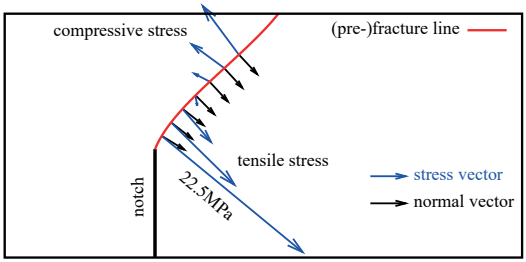

Figure 6.10.: Normal vectors (thin black arrows) and calculated stress vectors (thick blue arrows, compressive stress if underneath the pre-fracture line and tensile stress if above the line) at selected points on the pre-fracture line, which has been extracted and averaged from the crack paths of specimens under the pure mechanical loading condition. The averaged critical load of 272.4 N was applied as a single force in the simulation, where the notch was modeled as a crack [205].

This velocity, however, is much lower than typical velocities of surface waves in elastic ceramic materials.

Regarding the white line, it is not clear what causes this phenomenon and what it essentially is. It is provisionally interpreted as a pre-fracture line, which might be driven by the stress field in the specimen prior to cracking. This assumption reminds of a localization band which, however, is in fact only known for ductile materials [159], exhibiting intense shear strain in a narrow zone and pronounced strain softening behavior before failure. The deformation in the narrow zone leads to damage and cracking just after the localization band emerges. The appearance of localization bands is akin to what is observed in Fig. 6.9. In order to further illuminate this feature, the stress vectors on the pre-fracture line were computed with linear piezoelectric finite elements and illustrated in Fig. 6.10. The pre-fracture line in Fig. 6.10 has been extracted and averaged from five crack paths under identical boundary and loading conditions. The longer stress vectors (in blue, the length indicates the magnitude) on the pre-fracture line are almost either parallel or anti-parallel to the normal directions (unit length, small arrows in black). Normal stresses are tensile near the notch tip, while they are compressive at the last three sampling points. Along the pre-fracture line, the directions of the stress vectors change continuously, turning around gradually. The magnitude of the stress vector varies accompanied by the change of the direction, being reduced at first and increased again after the change from tensile to compressive. The stress near the notch tip, which has been modeled as a crack tip, is much larger than elsewhere due to the stress singularity. Near the upper boundary, the stress vectors, still being compressive and not included in the figure, will rotate further towards the opposite loading direction. Nevertheless, the pre-fracture line according to Fig. 6.10 is essentially oriented perpendicular to the directions of the large stress vectors, thus it is exposed to principal tensile or compressive stress rather than to shear stress as is known for classical localization bands in ductile materials.

A promising approach to further examine the nature of the pre-fracture line in Fig. 6.10 could be a numerical simulation of the three-point bending test based on nonlinear ferroelectric constitutive behavior. The applied electric load is lower than E_c, however, the crack gives rise to a much larger electric field in front of the crack tip, where the ferroelectric/-elastic domain switching takes place, incorporating a pronounced nonlinearity just as plasticity in ductile materials. Furthermore, the mechanical load may locally lead to domain switching apart from the crack tip. The nonlinear behavior of ferroelectrics has been implemented in a FE environment via subroutines and USER-elements [11,75,211], investigating damage, multiferroic and caloric phenomena. The application of the re-meshing algorithm for crack path predictions, however, is still missing here.

Digital Image Correlation (DIC) measurements on the surface of a loaded specimen could possibly provide further insight into the nature of the pre-fracture line. In-situ measurements, however, appear to be a challenging task, since the resolution of the images and the frame rate of high speed recording, whereupon 65100 frames per second turned out to be prerequisite, are competing requirements. A further problem to overcome in this regard is the application of a sufficiently fine stochastic speckle pattern on the comparatively small test surface. The DIC device in connection with the high-speed camera is basically suitable for the measurement of displacements on the surface of the specimen. However, the current camera system offers for the given frame rate a field of 320×304 pixels per cm^2, whereupon each speckle covers 2-3 pixels. Thus, the available resolution is too coarse to show the emergence of the white line and to provide additional information.

A recording of tests with electric loads is, unfortunately, elusive due to the limitation of the illumination system. The required power density of the illumination system is linearly dependent on the recording frame rate. The extraordinarily powerful spotlight used for the images of Fig. 6.9 does not provide enough light if the specimen has to be submerged into oil in an acrylic glass box, since the oil environment and reflections of the acrylic glass drastically reduce the light intensity on the specimen's surface.

7. Summary

The focus of this thesis is on crack paths in materials with coupled properties, in particular, the influence of the coupling effect and the electric field on crack deflections. The topics of crack deflection and crack paths in classical materials have been comprehensively studied and the obtained analysis methods basically provide reliable assessments and crack path prediction. However, the issues addressed in multi-field materials are still not sufficiently clarified, e.g., QCs with the coupled phonon–phason fields and piezoelectrics with the mechanical–electric fields.

Along this purpose, an all-around framework in the sense of continuum mechanics is developed in Chapter 2, including the phonon, phason and electric fields in piezoelectric QCs. The governing equations are derived assuming linear material behavior, thus the ferroelectric domain switching effect and the relaxation of the phason displacement are disregarded.

In Chapter 3, the closed-form solutions for planar crack problems in piezoelectric QCs and the solutions confined in the near-tip field are obtained considering an impermeable crack. The fundamental crack tip loading quantities, associated with classical crack growth criteria, are extended into the multi-field coupled materials. The crack deflection criteria proposed for classical materials are generalized for the coupled materials. Accounting for the change of potential mechanical energy with virtual displacement of the crack tip, a modified J_k^m-vector criterion is suggested for materials with piezoelectric property.

Subsequently in Chapter 4, the governing equations of 1D piezoelectric QC with one degree of freedom in the phason field are implemented in a FE environment. Via a USER-element type in connection with a subroutine, the solutions of boundary value problems in 1D piezoelectric QCs and the generalized fracture loading quantities are provided in the commercial FE software Abaqus. An adaptive re-meshing algorithm is introduced to simulate crack growth by repeatedly creating new crack faces and refined mesh at the crack tip in every increment, whereupon the deflection angle is determined by different numerical approaches in the post-processing.

The results of crack growth simulation, according to the introduced numerical tools, are shown in Chapter 5. Two special cases, the 1D QC and the piezoelectrics, are considered first by neglecting the electric property and the phason field, respectively, investigating the influence of the phonon–phason coupling and the electric loading on crack paths. Under mechanical mixed-mode loading conditions with an initially small K_{II}/K_I-ratio, where K_{II} nevertheless gives rise to a noticeable crack deflection, the phonon–phason coupling and the electric field show significant impact on the crack paths. With regard to the deflection criteria, the simulation results demonstrate that the

crack paths predicted by the maximum hoop stress criterion are likely to be affected by enlarger coupling coefficients of the QCs compared to the other criteria, however, show less impact of the electric loading in piezoelectrics. The J_k-vector criterion, as an appropriate deflection criterion in classical structural materials if K_{II} is much smaller than K_I, nonetheless proves to be invalid for the multi-field materials with piezoelectric property, at least if an electric loading is applied. The modified one, the J_k^m-vector criterion, incorporating only the mechanical part of the configurational driving force, seems to be reliable according to the crack paths in the simulation results. Moreover, the experimental crack paths presented in Chapter 6 are in some aspects well reproduced by the J_k^m-vector criterion. The crack growth in piezoelectric 1D QC are also simulated, showing the interrelation of the phason and the electric field, although there is no direct coupling between the two fields.

A series of three-point bending tests is carried out in Chapter 6, presenting statistically evaluated results of crack paths in PZT-5H specimens. Different electric loading conditions have been implemented in addition to a mechanical load to illuminate their influences on crack paths. The experimental findings could be qualitatively confirmed by simulations under positive electric loading. While negative electric loading shows converse influence compared to the simulation. Additionally, the negative electric field leads to the most distinctive scattering of crack paths, being manifested in the longest error bars, which is probably due to the domain switching induced by the large electric field at the crack tip. High-speed recordings of the crack propagation, taken for one of the tests under pure mechanical loading, reveals unexpected details of crack initiation and growth, where a white line is formed and precedes the actual crack growth. The line is denoted as pre-fracture line and has to be further investigated.

A. Material constants and characteristic matrices of the Stroh formalism

The material constants of diverse materials, employed in the analytical solutions and the numerical models in this thesis, are given in the following. The characteristic matrices and eigenvalues for the general solutions in the Stroh formalism according to Eqs. (3.9), (3.12) and (3.18) were calculated by the engineering computing software Mathematica and verified by using the orthogonal relations.

A.1. 1D QC

In compressed notation the constitutive equations of a 1D QC with the QA being parallel to the x_1-axis are

$$\begin{pmatrix} \sigma_{11} \\ \sigma_{22} \\ \sigma_{12} \\ H_{11} \\ H_{12} \end{pmatrix} = \begin{pmatrix} C_{1111} & C_{1122} & 0 & R_2 & 0 \\ C_{1122} & C_{2222} & 0 & R_1 & 0 \\ 0 & 0 & C_{1212} & 0 & R_3 \\ R_2 & R_1 & 0 & K_1 & 0 \\ 0 & 0 & R_3 & 0 & K_2 \end{pmatrix} \begin{pmatrix} \varepsilon_{11} \\ \varepsilon_{22} \\ 2\varepsilon_{12} \\ w_{11} \\ w_{12} \end{pmatrix} \tag{A.1}$$

in the state of plane strain.

Since the properties of 1D QC based on experiments are, to date, still unknown due to the absence of a measurement, the following material constants, adopted from the measured and evaluated results of 2D decagonal QCs [27, 45, 99], have been used for the calculations:

$$\begin{aligned} &C_{1111} = 232.22, \quad C_{1122} = 66.63, \quad C_{2222} = 234.33 \\ &C_{1133} = 66.63, \quad C_{2233} = 57.41, \quad C_{3333} = 234.33, \\ &C_{1212} = 70.19, \quad C_{1313} = 70.19, \quad C_{2323} = 88.46, \\ &R_1 = -1.1, \quad R_2 = 0.2, \quad R_3 = 0.5 \\ &K_1 = 122, \quad K_2 = 24. \end{aligned} \tag{A.2}$$

The units in A.2 are GPa and the values of the coupling coefficients are the reference values $\mathrm{R}^{\mathrm{ref}}$. However, R_3 is not provided by literature and thus is assumed in the same order of R_2. The stiffness matrix in Eq. (A.1) comes out to be positive definite for $\mathrm{R}^{\mathrm{ref}}$ and also for the 50 and 80 time enlarged coupling coefficients, which have been used for some of the calculations. For plane stress conditions, the following transformations are required:

$$\begin{aligned}
&C^s_{1111} = C_{1111} - \frac{C_{1133}C_{1133}}{C_{3333}}, \quad C^s_{2222} = C_{2222} - \frac{C_{2233}C_{2233}}{C_{3333}},\\
&C^s_{1122} = C_{1122} - \frac{C_{2233}C_{1133}}{C_{3333}}, \quad C^s_{2211} = C^s_{1122}, \quad C^s_{1212} = C_{1212},\\
&R^s_1 = R_1 - \frac{C_{2233}R_1}{C_{3333}}, \quad R^s_2 = R_2 - \frac{C_{1133}R_1}{C_{3333}}, \quad R^s_3 = R_3,\\
&K^s_1 = K_1 - \frac{R_1R_1}{C_{3333}}, \quad K^s_2 = K_2.
\end{aligned} \tag{A.3}$$

In a general 3D QC case, the characteristic matrices are 6×6, where three rows/columns are from the phonon field and the other three from the phason field. For a planar 1D QC, only two of the phonon dimensions and one of the phason fields are required. Thus, for the quasiperiodic direction along the x_1-direction and the material data according to (A.2), the following complex 3×3 matrices and eigenvalues are calculated by applying the methods introduced in [71]:

$$\begin{aligned}
A_{MN} &= \begin{pmatrix} -0.008585 & 1.136 & 0.551i \\ -0.002932i & 0.5395i & -1.142 \\ 0.9999 & 0.003374 & -0.003747i \end{pmatrix},\\
B_{MN} &= \begin{pmatrix} -0.4371i & 148.1i & -107.7 \\ 0.1939 & -107.2 & -151.3i \\ 54.10i & 1.167i & -0.7029 \end{pmatrix} \times 10^9,\\
p_N &= \begin{pmatrix} 2.255i \\ 1.383i \\ 0.7117i \end{pmatrix}.
\end{aligned} \tag{A.4}$$

For the quasiperiodic direction along the x_2-axis they are

$$
\begin{aligned}
A_{MN} &= \begin{pmatrix} -1.142 & 0.5395i & -0.002932i \\ -0.551i & -1.136 & 0.008585 \\ 0.003747i & -0.003374 & -0.99996 \end{pmatrix}, \\
B_{MN} &= \begin{pmatrix} -151.3i & -107.1 & 0.1939 \\ 107.7 & -148.1i & 0.4371i \\ 0.7029 & -1.167i & -54.10i \end{pmatrix} \times 10^9, \\
p_N &= \begin{pmatrix} 1.405i \\ 0.7233i \\ 0.4435i \end{pmatrix}.
\end{aligned}
\tag{A.5}
$$

The crack growth simulations for 1D QC in Section 5.1 are based on the plane stress state, since the QCs are so far applied as thin films, e.g., coating materials. Nonetheless, the state of plane stress or plane strain, in fact, has no essential influence on crack paths.

A.2. $BaTiO_3$

According to the measurements in [83,92], the material constants of polarized $BaTiO_3$ are

$$
\begin{aligned}
&C_{1111} = 166, \quad C_{1122} = 77.5, \quad C_{2222} = 162, \quad C_{1212} = 42.9, \\
&e_{211} = -4.4, \quad e_{222} = 18.6, \quad e_{121} = 11.6, \\
&\kappa_{11} = 14.34, \quad \kappa_{22} = 16.82,
\end{aligned}
\tag{A.6}
$$

where the poling direction is in the x_2-axis and the units are GPa, C/m^2 and C/(GVm), respectively. The corresponding constitutive equation is thus expressed as

$$
\begin{pmatrix} \sigma_{11} \\ \sigma_{22} \\ \sigma_{12} \\ D_1 \\ D_2 \end{pmatrix} = \begin{pmatrix} C_{1111} & C_{1122} & 0 & 0 & -e_{211} \\ C_{1122} & C_{2222} & 0 & 0 & -e_{222} \\ 0 & 0 & C_{1212} & -e_{121} & 0 \\ 0 & 0 & e_{121} & \kappa_{11} & 0 \\ e_{211} & e_{222} & 0 & 0 & \kappa_{22} \end{pmatrix} \begin{pmatrix} \varepsilon_{11} \\ \varepsilon_{22} \\ 2\varepsilon_{12} \\ E_1 \\ E_2 \end{pmatrix}. \tag{A.7}
$$

The matrices and the eigenvalues, being required for the solutions in the Stroh formal-

ism, are given as follows

$$
\begin{aligned}
A_{MN} &= \begin{pmatrix} 4.069-4.069i & -2.908-2.227i & -2.227-2.908i \\ 3.476+3.476i & 2.133-3.566i & 3.62.133i \\ 0.8925+0.8925i & 2.936+2.204i & -2.204-2.936i \end{pmatrix} \times 10^{-6}, \\
B_{MN} &= \begin{pmatrix} 35.08+35.08i & 22-24.13i & 24.13-22i \\ -32.01+32.01i & 26.51+22.36i & 22.36+26.51i \\ -7.231+7.231i & 11.04+0.442i & 0.442+11.04i \end{pmatrix} \times 10^{4}, \\
p_N &= \begin{pmatrix} 1.096i \\ -0.03635+0.941i \\ 0.03635+0.941i \end{pmatrix}.
\end{aligned}
\tag{A.8}
$$

A.3. PZT-5H

The material constants of PZT-5H with the poling direction in the x_2-axis, according to [147], are given as follows

$$
\begin{aligned}
&C_{1111} = 126, \quad C_{1122} = 53, \quad C_{2222} = 117, \quad C_{1212} = 35.3, \\
&e_{211} = -6.5, \quad e_{222} = 23.3, \quad e_{121} = 17, \\
&\kappa_{11} = 15.1, \quad \kappa_{22} = 13
\end{aligned}
\tag{A.9}
$$

with the same units of $BaTiO_3$. The matrices and the eigenvalues in the Stroh formalism based on the constants in (A.9) are

$$
\begin{aligned}
A_{MN} &= \begin{pmatrix} -11.89+11.89i & -4.268+35.61i & 35.61-4.268i \\ -14.329-14.329i & -31.17+8.521i & -8.521+31.17i \\ 30.06+30.06i & -23.52-7.223i & 7.223+23.52i \end{pmatrix} \times 10^{-7}, \\
B_{MN} &= \begin{pmatrix} -4.444-4.444i & -27.75-2.211i & 2.211+27.75i \\ 4.149-4.149i & -2.755-26.24i & -26.24-2.755i \\ 8.535-8.535i & -1.944-7.242i & -7.242-1.944i \end{pmatrix} \times 10^{4}, \\
p_N &= \begin{pmatrix} 1.071i \\ -0.1932+1.037i \\ 0.1932+1.037i \end{pmatrix}.
\end{aligned}
\tag{A.10}
$$

A.4. Piezoelectric 1D QC

Since the material constants reported for the properties of 1D piezoelectric QC are not fully reliable due to the absence of experimental measurements, different material

constants have been suggested, e.g., in [215], [199] and [212]. Considering that the quasicrystallized $BaTiO_3$ has been reported [62], the electric properties of the piezoelectric 1D QC in this work are taken from $BaTiO_3$ according to (A.6). The rest of material constants is adopted from the 1D QC given in (A.2). For the quasiperiodic direction and the poling direction along the x_2-axis, the matrices and the eigenvalues are

$$A_{MN} = \begin{pmatrix} 17.01-17.01i & -2.118+2.118i & -8.707-8.707i & 0.0751+0.0751i \\ 8.255+8.255i & -0.8429-0.8429i & 16.33-16.33i & -0.1711+0.1711i \\ -0.06196-0.06196i & -0.01129+0.01129i & 0.06167-0.06167i & 21.5-21.5i \\ 1.93+1.93i & -40.44-40.44i & 13.6-13.6i & -0.1449+0.1449i \end{pmatrix} \times 10^{-7},$$

$$B_{MN} = \begin{pmatrix} 22.85+22.85i & -6.642-6.642i & 17.52-17.52i & -0.5279+0.5279i \\ -16.2+16.2i & 7.261-7.261i & 23.88+23.88i & -1.19-1.19i \\ -1.038+1.038i & 0.1223-0.1223i & 1.75+1.75i & 11.63+11.63i \\ -2.456+2.456i & -5.986+5.986i & 0.9325+0.9325i & -0.0066-0.0066i \end{pmatrix} \times 10^{4},$$

$$p_N = \begin{pmatrix} 1.4099i \\ 0.91486i \\ 0.73383i \\ 0.44351i \end{pmatrix}, \tag{A.11}$$

with the same units as in the previous subsections.

B. Transformation of p, A_{IJ} and B_{IJ} of the Stroh formalism

In this section, the transformation of p, A_{IJ} and B_{IJ} into the local coordinate systems is introduced to obtain the solutions of a deflected crack during crack growth process. According to Eq. (3.13), an ansatz for the generalized displacements reads

$$\hat{u}_I = \hat{a}_I \hat{f}(\hat{z}) \qquad \hat{z} = \hat{x}_1 + \hat{p}\hat{x}_2, \tag{B.1}$$

where the hat indicates a variable in the local coordinate system. Similar to the derivation of Eq. (3.9) from Eq. (3.5) in the global coordinate system, the eigenvalue equation in the local coordinates $\hat{x}_i$ is found as

$$\{\hat{C}_{I1K1} + (\hat{C}_{I1K2} + \hat{C}_{I2K1})\hat{p} + \hat{C}_{I2K2}\hat{p}^2\}\hat{a}_K = 0, \tag{B.2}$$

and the corresponding elastic tensors are obtained by using Eqs. (3.29) and (3.31)

$$\begin{aligned}
\hat{C}_{I1K1} &= \Omega_{IM}\Omega_{KP}(\cos^2\varphi\, C_{M1P1} + \sin\varphi\cos\varphi\, C_{M2P1} + \sin\varphi\cos\varphi\, C_{M1P2} + \sin^2\varphi\, C_{M2P2}),\\
\hat{C}_{I1K2} &= \Omega_{IM}\Omega_{KP}(-\sin\varphi\cos\varphi\, C_{M1P1} - \sin^2\varphi\, C_{M2P1} + \cos^2\varphi\, C_{M1P2} + \sin\varphi\cos\varphi\, C_{M2P2}),\\
\hat{C}_{I2K1} &= \Omega_{IM}\Omega_{KP}(-\sin\varphi\cos\varphi\, C_{M1P1} - \sin^2\varphi\, C_{M1P2} + \cos^2\varphi\, C_{M2P1} + \sin\varphi\cos\varphi\, C_{M2P2}),\\
\hat{C}_{I2K2} &= \Omega_{IM}\Omega_{KP}(\sin^2\varphi\, C_{M1P1} - \sin\varphi\cos\varphi\, C_{M2P1} - \sin\varphi\cos\varphi\, C_{M1P2} + \cos^2\varphi\, C_{M2P2}),
\end{aligned} \tag{B.3}$$

where φ is the angle between the two coordinate systems, see Fig. 3.3. Inserting Eq. (B.3) into Eq. (B.2), the eigenvalue equation is expressed as

$$\left(C_{M1P1} + (C_{M2P1} + C_{M1P2})\frac{\sin\varphi + \hat{p}\cos\varphi}{\cos\varphi - \hat{p}\sin\varphi} + C_{M2P2}\left(\frac{\sin\varphi + \hat{p}\cos\varphi}{\cos\varphi - \hat{p}\sin\varphi}\right)^2\right)\Omega_{IM}\Omega_{KP}\hat{a}_K = 0. \tag{B.4}$$

Comparing the identical eigenvalue problems Eqs. (B.4) and (3.9), the relation of p and $\hat{p}$ is readily found:

$$p = \frac{\sin\varphi + \hat{p}\cos\varphi}{\cos\varphi - \hat{p}\sin\varphi} \qquad \text{or} \qquad \hat{p} = \frac{p\cos\varphi - \sin\varphi}{p\sin\varphi + \cos\varphi}. \tag{B.5}$$

It is noted that outside the braces, Ω_{IM} does not have any associated index with $\Omega_{KP}\hat{a}_K$. As a non-singular matrix, Ω_{IM} thus can be eliminated providing the relations

$$a_P = \Omega_{KP}\hat{a}_K \quad \text{or} \quad \hat{a}_K = \Omega_{KP}a_P, \tag{B.6}$$

and

$$A_{IK} = \Omega_{JI}\hat{A}_{JK} \quad \text{or} \quad \hat{A}_{IK} = \Omega_{IJ}A_{JK}. \tag{B.7}$$

This relation can also be derived from the formulation of $\hat{z}$. Replacing $\hat{x}_i$ in Eq. (B.1) by the transformed x_i, $\hat{z}$ is expressed as

$$\hat{z} = (\cos\varphi - \hat{p}\sin\varphi)(x_1 + \frac{\sin\varphi + \hat{p}\cos\varphi}{\cos\varphi - \hat{p}\sin\varphi}x_2), \tag{B.8}$$

where the displacement vector $\hat{u}_I$ depends on $\hat{z}$. Meanwhile, $\hat{u}_I$ is also related to z:

$$\hat{u}_I = \Omega_{IJ}u_J = \Omega_{IJ}a_J f(z). \tag{B.9}$$

Comparing Eq. (B.9) to Eq. (B.1) and without loss in generality, $\hat{z}$ has to be a function of z, i.e.

$$\hat{z} = g(z) = g(x_1 + px_2). \tag{B.10}$$

Apparently, the expression of p can be extracted from Eq. (B.8).

Substituting stresses according to Eq. (3.17) into the constitutive equations Eq. (3.4), the relation of u_K and ϕ_K is given as

$$\begin{pmatrix} C_{I1K1} & 0 \\ C_{I2K1} & -\delta_{IK} \end{pmatrix}\begin{pmatrix} u_{K,1} \\ \phi_{K,1} \end{pmatrix} + \begin{pmatrix} C_{I1K2} & \delta_{IK} \\ C_{I2K2} & 0 \end{pmatrix}\begin{pmatrix} u_{K,2} \\ \phi_{K,2} \end{pmatrix} = 0 \tag{B.11}$$

Based on Eqs. (3.6), (3.7) and (3.19), the following relations can be derived

$$u_{I,2} = p\,u_{I,1} \quad \text{and} \quad \phi_{I,2} = p\,\phi_{I,1}, \tag{B.12}$$

which allows transforming Eq. (B.11) into a 8-dimensional eigenvalue problem

$$\begin{pmatrix} N^1_{IJ} & N^2_{IJ} \\ N^3_{IJ} & N^1_{JI} \end{pmatrix}\begin{pmatrix} a_J \\ b_J \end{pmatrix} = p\begin{pmatrix} a_J \\ b_J \end{pmatrix}, \tag{B.13}$$

where

$$\begin{aligned} N^1_{IJ} &= -C^{-1}_{I2K2}\,C_{K2J1}, \\ N^2_{IJ} &= C^{-1}_{I2J2}, \\ N^3_{IJ} &= C_{I1K2}\,C^{-1}_{K2L2}\,C_{L2J1} - C_{I1J1}. \end{aligned} \tag{B.14}$$

Taking a look at Eq. (B.13), the mathematical rules governing a_I and A_{IJ} are also valid for b_I and B_{IJ}, i.e.,

$$\hat{b}_I = \Omega_{IJ}b_J \quad \text{and} \quad \hat{B}_{IK} = \Omega_{IJ}B_{JK}. \tag{B.15}$$

Eqs. (B.5), (B.7) and (B.15) enable the transformation of the near-tip solutions of an anisotropic material according to Eq. (3.27) into any direction without repeated calculation.

C. Equivalence of $-H$ and J_2 in isotropic LEFM

The equivalence of G and J_1 in linear elastic fracture mechanics (LEFM) provides a practical way for obtaining J_1 from the K-factors without a cumbersome path integral, in particular, if an appropriate integral contour is not available. In classical materials the proof of this relation has been given in an isotropically linear elastic case [157], selecting a circular integral contour surrounding the crack tip with radius $r \to 0$. Since G and J_1 are both motivated energetically, their equivalence is easily understood. Although the second energy term in the crack closure integral H is obtained in a similar way as G by formally replacing σ_{i2} by σ_{i1} [132], it does not describe a virtual crack closing process. Thus, H doesn't have any physical interpretation and a relation with J_2 needs to be proved.

Assuming a planar problem in isotropic materials with a crack under mixed mode-I/II loading, the second energy term H is obtained as

$$H = \lim_{\Delta a \to 0} \frac{1}{2\Delta a} \int_0^{\Delta a} \sigma_{i1}(r,0)\, \Delta u_i(\Delta a - r, \pi) \mathrm{d}r = \frac{1+\kappa}{4\mu} K_I K_{II}, \tag{C.1}$$

where the asymptotic near-tip fields are employed. The stresses and displacements of a crack under mixed mode-I/II loading in isotropic materials are given as follows [115]

$$\begin{aligned} \sigma_{ij} &= \frac{1}{\sqrt{2\pi r}} \left(K_I f_{ij}^I(\theta) + K_{II} f_{ij}^{II}(\theta) \right), \\ u_i &= \frac{1}{2\mu} \sqrt{\frac{r}{2\pi}} \left(K_I d_i^I(\theta) + K_{II} d_i^{II}(\theta) \right), \end{aligned} \tag{C.2}$$

where the angular functions for stresses and displacements are given as

$$\begin{aligned} f_{11}^I &= \cos\frac{\theta}{2}\left(1 - \sin\frac{\theta}{2}\sin\frac{3\theta}{2}\right), & f_{11}^{II} &= -\sin\frac{\theta}{2}\left(2 + \cos\frac{\theta}{2}\cos\frac{3\theta}{2}\right), \\ f_{22}^I &= \cos\frac{\theta}{2}\left(1 + \sin\frac{\theta}{2}\sin\frac{3\theta}{2}\right), & f_{22}^{II} &= \sin\frac{\theta}{2}\cos\frac{\theta}{2}\cos\frac{3\theta}{2}, \\ f_{12}^I &= \cos\frac{\theta}{2}\sin\frac{\theta}{2}\cos\frac{3\theta}{2}, & f_{12}^{II} &= -\cos\frac{\theta}{2}\left(1 - \sin\frac{\theta}{2}\sin\frac{3\theta}{2}\right), \end{aligned} \tag{C.3}$$

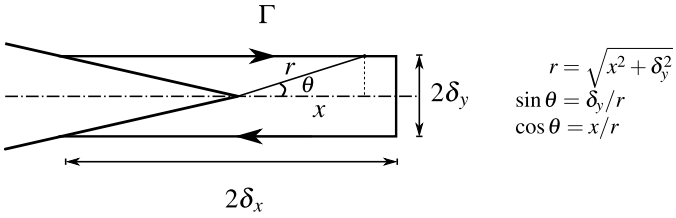

Figure C.1.: Infinitesimal contour Γ with the length $2\delta_x$ and height $2\delta_y$ surrounding the crack tip.

and

$$\begin{aligned} d_1^I &= \cos\frac{\theta}{2}(\kappa - \cos\theta), \qquad g_1^{II} = \sin\frac{\theta}{2}(\kappa + 2 + \cos\theta), \\ d_2^I &= \sin\frac{\theta}{2}(\kappa - \cos\theta), \qquad g_2^{II} = \cos\frac{\theta}{2}(\kappa - 2 + \cos\theta), \end{aligned} \tag{C.4}$$

respectively.

On the other side, J_2 can be calculated using the integral along an infinitesimal contour at the crack tip

$$J_2 = \lim_{\delta_x \to 0} \lim_{\delta_y \to 0} \int_\Gamma \left(\frac{1}{2}\sigma_{ij}\varepsilon_{ij} n_2 - \sigma_{ij} u_{i,2} n_j \right) \mathrm{d}\Gamma, \tag{C.5}$$

where the contour is illustrated in Fig. C.1. Due to the limit of the contour edges, taking $\delta_y \to 0$ prior to $\delta_x \to 0$, only the top and bottom contours have to be considered in the integral

$$J_2 = 2 \lim_{\delta_x \to 0} \int_{-\delta_x}^{\delta_x} \left(\frac{1}{2}\sigma_{ij}\varepsilon_{ij} - \sigma_{i2} u_{i,2} \right) \mathrm{d}x = 2 \lim_{\delta_x \to 0} \int_{-\delta_x}^{\delta_x} f(x) \mathrm{d}x, \tag{C.6}$$

where n_1 vanishes and $n_2 = 1$ represents the top contour. The bottom contour provides the same result as the top contour due to the symmetric property of the stresses and the asymmetry of the displacement gradients.

Let $f(x)$ represents the integrand in Eq. (C.6), it can be expanded as

$$f(x) = \frac{1}{2}\sigma_{11}u_{1,1} - \frac{1}{2}\sigma_{12}u_{1,2} + \frac{1}{2}\sigma_{12}u_{2,1} - \frac{1}{2}\sigma_{22}u_{2,2}. \tag{C.7}$$

Inserting the angular functions f_{ij} and d_i into the stresses and displacements in Eq. (C.7) and differentiating the displacements with respect to x_1 and x_2 accounting for Eq. (2.15), leads to the simple expression

$$f(x) = \frac{-1}{8\mu\pi r}(1+\kappa)\cos\theta \left(K_I \sin\theta + K_{II}\cos\theta \right)^2. \tag{C.8}$$

In order to integrate $f(x)$ according to Eqs. (C.6) and (C.7), the variable r and functions of θ have to be converted applying the relations in Fig. C.1, yielding

$$\begin{aligned} J_2 &= 2 \lim_{\delta_x \to 0} \left(\lim_{\delta_y \to 0} \int_{-\delta_x}^{\delta_x} \frac{-(1+\kappa)}{8\mu\pi} \left(K_I^2 \frac{x\delta_y^2}{(x^2+\delta_y^2)^2} + K_{II}^2 \frac{x^3}{(x^2+\delta_y^2)^2} + 2K_I K_{II} \frac{x^2\delta_y}{(x^2+\delta_y^2)^2} \right) \mathrm{d}x \right) \\ &= \frac{-(1+\kappa)}{4\mu\pi} \lim_{\delta_x \to 0} \left(\left(K_I^2 \left[-\frac{\delta_y^2}{2(x^2+\delta_y^2)} \right]_{-\delta_x}^{\delta_x} \right) + \left(\frac{K_{II}^2}{2} \left[\frac{\delta_y^2}{x^2+\delta_y^2} + \ln(x^2+\delta_y^2) \right]_{-\delta_x}^{\delta_x} \right) \right. \\ &\quad \left. + \left(K_I K_{II} \left[\arctan \frac{x}{\delta_y} - \frac{x\delta_y}{x^2+\delta_y^2} \right]_{-\delta_x}^{\delta_x} \right) \right). \end{aligned} \tag{C.9}$$

Finally, J_2 is derived by taking the limit $\delta_y \to 0$:

$$J_2 = \frac{-(1+\kappa)}{4\mu} K_I K_{II}, \tag{C.10}$$

Eqs. (C.10) and (C.1) are identical, except for the factor -1. This relation is given in [19], however, the derivation is not presented.

A mathematical proof of the relation of J_2 and $-H$ in anisotropic functional materials is challenging due to the complexity of the stress and displacement solutions, see Eqs. (3.27), where the angular functions include complex numbers. Nevertheless, a numerical validation has been done in both classical and coupled materials [132, 168, 206].

Bibliography

[1] https://en.wikipedia.org/wiki/File:Penrose_Tiling_(Rhombi).svg. [Online; accessed 14-November-2019].

[2] https://www.dvorsons.com/Sitram/Cybernox/Cybernox.html. [Online; accessed 18-November-2019].

[3] Report of the executive committee for 1991. *Acta Crystallographica A 48*, 6 (1992), 922–946.

[4] ABE, E., SATO, T. J., AND TSAI, A. P. Structure of a quasicrystal without atomic clusters. *Physical Review Letters 82*, 26 (1999), 5269–5272.

[5] ABENDROTH, M., GROH, U., KUNA, M., AND RICOEUR, A. Finite element-computation of the electromechanical *J*-Integral for 2-D and 3-D crack analysis. *International Journal of Fracture 114*, 4 (2002), 359–378.

[6] ACOSTA, M., NOVAK, N., ROJAS, V., PATEL, S., VAISH, R., KORUZA, J., ROSSETTI, G. A., AND RÖDEL, J. $BaTiO_3$-based piezoelectrics: Fundamentals, current status, and perspectives. *Applied Physics Reviews 4*, 4 (2017), 041305.

[7] AGIASOFITOU, E., AND LAZAR, M. The elastodynamic model of wave-telegraph type for quasicrystals. *International Journal of Solids and Structures 51*, 5 (2014), 923–929.

[8] ALIABADI, M. H. Boundary element formulations in fracture mechanics. *Applied Mechanics Reviews 50*, 2 (1997), 83–96.

[9] ALTENBACH, H. *Kontinuumsmechanik*. Springer Berlin Heidelberg, 2012.

[10] AREIAS, P. M. A., AND BELYTSCHKO, T. Analysis of three-dimensional crack initiation and propagation using the extended finite element method. *International Journal for Numerical Methods in Engineering 63*, 5 (2005), 760–788.

[11] AVAKIAN, A., AND RICOEUR, A. Numerical simulation of multiferroic composites: prediction of magnetoelectric coupling and damage. *Continuum Mechanics and Thermodynamics 32*, 5 (2019), 1455–1472.

[12] BAK, P. Icosahedral crystals: Where are the atoms? *Physical Review Letters 56*, 8 (1986), 861–864.

[13] BARENBLATT, G. The mathematical theory of equilibrium cracks in brittle fracture. In *Advances in Applied Mechanics*. Elsevier, 1962, pp. 55–129.

[14] Barnett, D. M., and Lothe, J. Dislocations and line charges in anisotropic piezoelectric insulators. *physica status solidi (b) 67*, 1 (1975), 105–111.

[15] Barsoum, R. S. On the use of isoparametric finite elements in linear fracture mechanics. *International Journal for Numerical Methods in Engineering 10*, 1 (1976), 25–37.

[16] Bathe, K.-J. Finite Element Method. In *Wiley Encyclopedia of Computer Science and Engineering*. John Wiley & Sons, Inc, 2007.

[17] Belytschko, T., and Black, T. Elastic crack growth in finite elements with minimal remeshing. *International Journal for Numerical Methods in Engineering 45*, 5 (1999), 601–620.

[18] Bendersky, L. A., and Burton, B. A warm welcome to quasicrystals. *Journal of Phase Equilibria and Diffusion 33*, 2 (2012), 83–84.

[19] Bergez, D. Determination of stress intensity factors by use of path-independent integrals. *Mechanics Research Communications 1*, 3 (1974), 179–180.

[20] Borchardt-Ott, W., and Sowa, H. *Kristallographie*. Springer Berlin Heidelberg, 2013.

[21] Brock, C. P., Hahn, T., Wondratschek, H., Müller, U., Shmueli, U., Prince, E., Authier, A., Kopský, V., Litvin, D. B., Arnold, E., Himmel, D. M., Rossmann, M. G., Hall, S., McMahon, B., and Aroyo, M. I. vol. A. International Union of Crystallography, Chester, England, 2016.

[22] Burdekin, F. M., and Stone, D. E. W. The crack opening displacement approach to fracture mechanics in yielding materials. *Journal of Strain Analysis 1*, 2 (1966), 145–153.

[23] Cao, H., and Evans, A. G. Electric-field-induced fatigue crack growth in piezoelectrics. *Journal of the American Ceramic Society 77*, 7 (1994), 1783–1786.

[24] Cardona, M., Fulde, P., Klitzing, K. v., Merlin, R., Queisser, H.-J., Störmer, H., and Stadnik, Z. M., Eds. *Physical Properties of Quasicrystals*. Springer Series in Solid-State Sciences. Springer Berlin Heidelberg, Berlin, Heidelberg, 1999.

[25] Carpenter, M. A., Salje, E. K., and Graeme-Barber, A. Spontaneous strain as a determinant of thermodynamic properties for phase transitions in minerals. *European Journal of Mineralogy 10*, 4 (1998), 621–691.

[26] Chen, H.-S., Wang, H.-L., Pei, Y.-M., Wei, Y.-J., Liu, B., and Fang, D.-N. Crack instability of ferroelectric solids under alternative electric loading. *Journal of the Mechanics and Physics of Solids 81* (2015), 75–90.

[27] CHERNIKOV, M. A., OTT, H. R., BIANCHI, A., MIGLIORI, A., AND DARLING, T. W. Elastic Moduli of a Single Quasicrystal of Decagonal Al-Ni-Co: Evidence for Transverse Elastic Isotropy. *Physical Review Letters 80*, 2 (1998), 321–324.

[28] COCKAYNE, E., MIHALKOVIČ, M., AND HENLEY, C. L. Structure of periodic crystals and quasicrystals in ultrathin films of Ba-Ti-O. *Physical Review B 93*, 2 (2016), 0201011–201014.

[29] CONRAD, M., KRUMEICH, F., AND HARBRECHT, B. A dodecagonal quasicrystalline chalcogenide. *Angewandte Chemie International Edition 37*, 10 (1998), 1383–1386.

[30] COOK, R. F., FREIMAN, S. W., LAWN, B. R., AND POHANKA, R. C. Fracture of ferroelectric ceramics. *Ferroelectrics 50*, 1 (1983), 267–272.

[31] D. DING, W. YANG, C. HU, R. WANG. Linear elasticity theory of quasicrystals and defects in quasicrystals. *Materials Science Forum 150-151* (1994), 345–354.

[32] DE BOISSIEU, M. Phonons, phasons and atomic dynamics in quasicrystals. *Chemical Society Reviews 41*, 20 (2012), 6778–6786.

[33] DEEG, W. F. *The analysis of dislocation, crack, and inclusion problems in piezoelectric solids*. Dissertation, Stanford University, CA, 1980.

[34] DHONDT, G. Cutting of a 3-D finite element mesh for automatic mode I crack propagation calculations. *International Journal for Numerical Methods in Engineering 42*, 4 (1998), 749–772.

[35] DING, D., YANG, W., HU, C., AND WANG, R. Generalized elasticity theory of quasicrystals. *Physical Review B 48*, 10 (1993), 7003–7010.

[36] DOS SANTOS E LUCATO, S. L., BAHR, H.-A., PHAM, V.-B., LUPASCU, D. C., BALKE, H., RÖDEL, J., AND BAHR, U. Electrically driven cracks in piezoelectric ceramics: experiments and fracture mechanics analysis. *Journal of the Mechanics and Physics of Solids 50*, 11 (2002), 2333–2353.

[37] DOS SANTOS E LUCATO, S. L., LUPASCU, D. C., AND RÖDEL, J. Effect of poling direction on R-Curve behavior in lead zirconate titanate. *Journal of the American Ceramic Society 83*, 2 (2000), 424–426.

[38] DUBOIS, J.-M. *Useful Quasicrystals*. World Scientific, 2005.

[39] DUBOIS, J.-M. So useful, those quasicrystals. *Israel Journal of Chemistry 51*, 11-12 (2011), 1168–1175.

[40] DUBOIS, J.-M., AND BELIN-FERRÉ, E. Friction and solid-solid adhesion on complex metallic alloys. *Science and Technology of Advanced Materials 15*, 3 (2014), 034804.

[41] DUBOST, B., LANG, J. M., TANAKA, M., SAINFORT, P., AND AUDIER, M. Large AlCuLi single quasicrystals with triacontahedral solidification morphology. *Nature 324*, 6092 (1986), 48–50.

[42] DUGDALE, D. Yielding of steel sheets containing slits. *Journal of the Mechanics and Physics of Solids 8*, 2 (1960), 100–104.

[43] DUNEAU, M., AND KATZ, A. Quasiperiodic patterns. *Physical Review Letters 54*, 25 (1985), 2688–2691.

[44] DUQUESNE, J.-Y., AND PERRIN, B. Elastic wave interaction in icosahedral AlPdMn. *Physica B: Condensed Matter 316-317* (2002), 317–320.

[45] EDAGAWA, K. Phonon–phason coupling in decagonal quasicrystals. *Philosophical Magazine 87*, 18-21 (2007), 2789–2798.

[46] EDAGAWA, K., SUZUKI, K., AND TAKEUCHI, S. High Resolution Transmission Electron Microscopy observation of thermally fluctuating phasons in decagonal Al-Cu-Co. *Physical Review Letters 85*, 8 (2000), 1674–1677.

[47] EISCHEN, J. An improved method for computing the integral. *Engineering Fracture Mechanics 26*, 5 (1987), 691–700.

[48] ERDOGAN, F., AND SIH, G. C. On the crack extension in plates under plane loading and transverse shear. *Journal of Basic Engineering 85*, 4 (1963), 519–525.

[49] ESHELBY, J. D. The force on an elastic singularity. *Philosophical Transactions of the Royal Society A 244*, 877 (1951), 87–112.

[50] FAN, T.-Y. *Mathematical Theory of Elasticity of Quasicrystals and Its Applications*. Springer Singapore, 2016.

[51] FAN, T.-Y., AND FAN, L. Relation between Eshelby integral and generalized BCS and generalized DB models for some one-and two-dimensional quasicrystals. *Chinese Physics B 20*, 4 (2011), 036102.

[52] FAN, T.-Y., TANG, Z.-Y., AND CHEN, W.-Q. Theory of linear, nonlinear and dynamic fracture for quasicrystals. *Engineering Fracture Mechanics 82* (2012), 185–194.

[53] FAN, T. Y., WANG, X. F., LI, W., AND ZHU, A. Y. Elasto-hydrodynamics of quasicrystals. *Philosophical Magazine 89*, 6 (2009), 501–512.

[54] FANG, D., AND LIU, J. *Fracture Mechanics of Piezoelectric and Ferroelectric Solids*. Springer Berlin Heidelberg, Berlin, Heidelberg, 2013.

[55] FANG, D., ZHANG, Z.-K., SOH, A. K., AND LEE, K. L. Fracture criteria of piezoelectric ceramics with defects. *Mechanics of Materials 36*, 10 (2004), 917–928.

[56] FANG, F., AND YANG, W. Poling-enhanced fracture resistance of lead zirconate titanate ferroelectric ceramics. *Materials Letters 46*, 2-3 (2000), 131–135.

[57] FANG, F., AND YANG, W. Indentation-induced cracking and 90° domain switching pattern in barium titanate ferroelectric single crystals under different poling. *Materials Letters 57*, 1 (2002), 198–202.

[58] FISHER, I. R., CHEON, K. O., PANCHULA, A. F., CANFIELD, P. C., CHERNIKOV, M., OTT, H. R., AND DENNIS, K. Magnetic and transport properties of single-grain R-Mg-Zn icosahedral quasicrystals [R=Y,($Y_{1-x}Gd_x$),($Y_{1-x}Tb_x$), Tb, Dy, Ho, and Er] . *Physical Review B 59*, 1 (1999), 308–321.

[59] FISHER, I. R., ISLAM, Z., PANCHULA, A. F., CHEON, K. O., KRAMER, M. J., CANFIELD, P. C., AND GOLDMAN, A. I. Growth of large-grain R-Mg-Zn quasicrystals from the ternary melt (R = Y, Er, Ho, Dy and Tb). *Philosophical Magazine B 77*, 6 (1998), 1601–1615.

[60] FISHER, I. R., KRAMER, M. J., ISLAM, Z., ROSS, A. R., KRACHER, A., WIENER, T., SAILER, M. J., GOLDMAN, A. I., AND CANFIELD, P. C. On the growth of decagonal Al-Ni-Co quasicrystals from the ternary melt. *Philosophical Magazine B 79*, 3 (1999), 425–434.

[61] FÖRDERREUTHER, A. *Mechanische Eigenschaften von $BaTiO_3$-Keramiken unter mechanischer und elektrischer Belastung*. Dissertation, Univ. Stuttgart, Stuttgart, 2003.

[62] FÖRSTER, S., MEINEL, K., HAMMER, R., TRAUTMANN, M., AND WIDDRA, W. Quasicrystalline structure formation in a classical crystalline thin-film system. *Nature 502*, 7470 (2013), 215–218.

[63] FREIMAN, S. W. Mechanical behavior of ferroelectric ceramics. In *Sixth IEEE International Symposium on Applications of Ferroelectrics* (1986), pp. 367–373.

[64] FU, R., QIAN, C.-F., AND ZHANG, T.-Y. Electrical fracture toughness for conductive cracks driven by electric fields in piezoelectric materials. *Applied Physics Letters 76*, 1 (2000), 126–128.

[65] FU, R., AND ZHANG, T. Y. Effects of an electric field on the fracture toughness of poled lead zirconate titanate ceramics. *Journal of the American Ceramic Society 83*, 5 (2000), 1215–1218.

[66] GACHOT, C., ROSENKRANZ, A., BUCHHEIT, R., SOUZA, N., AND MÜCKLICH, F. Tailored frictional properties by penrose inspired surfaces produced by direct laser interference patterning. *Applied Surface Science 367* (2016), 174–180.

[67] GAO, H., ZHANG, T.-Y., AND TONG, P. Local and global energy release rates for an electrically yielded crack in a piezoelectric ceramic. *Journal of the Mechanics and Physics of Solids 45*, 4 (1997), 491–510.

[68] GAO, Y., AND RICOEUR, A. Three-dimensional Green's functions for two-dimensional quasi-crystal bimaterials. *Proceedings of the Royal Society A 467*, 2133 (2011), 2622–2642.

[69] GAO, Y., AND RICOEUR, A. Three-dimensional analysis of a spheroidal inclusion in a two-dimensional quasicrystal body. *Philosophical Magazine 92*, 34 (2012), 4334–4353.

[70] GAO, Y., RICOEUR, A., AND ZHANG, L. Plane problems of cubic quasicrystal media with an elliptic hole or a crack. *Physics Letters A 375*, 28-29 (2011), 2775–2781.

[71] GAO, Y., RICOEUR, A., ZHANG, L., AND YANG, L. Crack solutions and weight functions for plane problems in three-dimensional quasicrystals. *Archive of Applied Mechanics 84*, 8 (2014), 1103–1115.

[72] G.C SIH, AND J.Z ZUO. Multiscale behavior of crack initiation and growth in piezoelectric ceramics. *Theoretical and Applied Fracture Mechanics 34*, 2 (2000), 123–141.

[73] GELLMANN, R., AND RICOEUR, A. Some new aspects of boundary conditions at cracks in piezoelectrics. *Archive of Applied Mechanics 82*, 6 (2011), 841–852.

[74] GELLMANN, R., AND RICOEUR, A. Extended semi-analytical investigations of crack growth resistance behavior in ferroelectric materials. *Acta Mechanica 223*, 11 (2012), 2357–2368.

[75] GELLMANN, R., AND RICOEUR, A. Continuum damage model for ferroelectric materials and its application to multilayer actuators. *Smart Materials and Structures 25*, 5 (2016), 055045.

[76] GILLE, P., BAUER, B., HAHNE, M., SMONTARA, A., AND DOLINŠEK, J. Single crystal growth of Al-based intermetallic phases being approximants to quasicrystals. *Journal of Crystal Growth 318*, 1 (2011), 1016–1020.

[77] GRIFFITH, A. A. The phenomena of rupture and flow in solids. *Philosophical Transactions of the Royal Society A: Mathematical, Physical and Engineering Sciences 221*, 582-593 (1921), 163–198.

[78] GRIMMER, H. A simple method of determining the form of the phonon part of tensors describing quasicrystal properties. *Acta Crystallographica A 63*, 3 (2007), 266–272.

[79] GROSS, D., WRIGGERS, P., AND HAUGER, W. *Technische Mechanik. Band 4: Hydromechanik, Elemente der Höheren Mechanik, Numerische Methoden*. Springer Berlin Heidelberg, 2009.

[80] HACKEMANN, S., AND PFEIFFER, W. Domain switching in process zones of PZT. *Journal of the European Ceramic Society 23*, 1 (2003), 141–151.

[81] HAO, T. H., AND SHEN, Z. Y. A new electric boundary condition of electric fracture mechanics and its applications. *Engineering Fracture Mechanics 47*, 6 (1994), 793–802.

[82] HE, L. X., WU, Y. K., AND KUO, K. H. Decagonal quasicrystals with different periodicities along the tenfold axis in rapidly solidified $Al_{65}Cu_{20}M_{15}$ (M=Mn, Fe, Co or Ni). *Journal of Materials Science Letters 7*, 12 (1988), 1284–1286.

[83] HE, M.-Y., SUO, Z., MCMEEKING, R. M., EVANS, A. G., AND LYNCH, C. S. Mechanics of some degradation mechanisms in ferroelectric ceramic actuators. In *Proc. SPIE 2189, Smart Structures and Materials 1994: Smart Materials* (1994), V. K. Varadan, Ed., SPIE.

[84] HELLEN, T. K., AND BLACKBURN, W. S. The calculation of stress intensity factors for combined tensile and shear loading. *International Journal of Fracture 11*, 4 (1975), 605–617.

[85] HENSHELL, R. D., AND SHAW, K. G. Crack tip finite elements are unnecessary. *International Journal for Numerical Methods in Engineering 9*, 3 (1975), 495–507.

[86] HIRAGA, K., SUN, W., LINCOLN, F. J., KANEKO, M., AND MATSUO, Y. Formation of decagonal quasicrystal in the Al-Pd-Mn system and its structure. *Japanese Journal of Applied Physics 30*, Part 1, No. 9A (1991), 2028–2034.

[87] HU, C., WANG, R., AND DING, D. Symmetry groups, physical property tensors, elasticity and dislocations in quasicrystals. *Reports on Progress in Physics 63*, 1 (2000), 1–39.

[88] HUSSAIN, M., PU, S., AND UNDERWOOD, J. Strain energy release rate for a crack under combined mode I and mode II. In *Fracture Analysis: Proceedings of the 1973 National Symposium on Fracture Mechanics, Part II*, G. Irwin, Ed. ASTM International, pp. 2–28.

[89] HWU, C., AND TING, T. C. T. Two-dimensional problems of the anisotropic elastic solid with an elliptic inclusion. *The Quarterly Journal of Mechanics and Applied Mathematics 42*, 4 (1989), 553–572.

[90] IRWIN, G. R. Onset of fast crack propagation in high strength steel and aluminum alloys. Tech. rep., Naval Research Lab., Washington, D.C., 1956.

[91] IRWIN, G. R. Analysis of stresses and strains near the end of a crack transversing a plate. *Journal of Applied Mechanics, Transactions ASME 24* (1957), 361–364.

[92] JAFFE, B., COOK, W. R., AND JAFFE, H. *Piezoelectric ceramics*, vol. 3. Academic Press, London and New York, 1971.

[93] JANOT, C. *Quasicrystals: A primer*, 2nd ed. ed., vol. 50 of *Monographs on the physics and chemistry of materials*. Clarendon Press and Oxford University Press, Oxford and New York, 1994.

[94] JANSKI, L., AND KUNA, M. Adaptive finite element modeling of stationary and propagating cracks in piezoelectric structures. *Archives of Mechanics 63*, 5-6 (2011), 599–619.

[95] JANSSEN, M., ZUIDEMA, J., AND WANHILL, R. *Fracture Mechanics, Second Edition: Fundamentals and Applications*. Taylor & Francis, 2004.

[96] JANSSEN, T. Aperiodic crystals: A contradictio in terminis? *Physics Reports 168*, 2 (1988), 55–113.

[97] JANSSEN, T. International Tables for Crystallography, Vol. D. Kluwer Academic Publishers, 2003, pp. 243–264.

[98] JELITTO, H., KESSLER, H., SCHNEIDER, G. A., AND BALKE, H. Fracture behavior of poled piezoelectric PZT under mechanical and electrical loads. *Journal of the European Ceramic Society 25*, 5 (2005), 749–757.

[99] JEONG, H.-C., AND STEINHARDT, P. J. Finite-temperature elasticity phase transition in decagonal quasicrystals. *Physical Review B 48*, 13 (1993), 9394–9403.

[100] JEONG, H.-C., AND STEINHARDT, P. J. Constructing Penrose-like tilings from a single prototile and the implications for quasicrystals. *Physical Review B 55*, 6 (1997), 3520–3532.

[101] JUDT, P. *Numerische Beanspruchungsanalyse von Rissen und Berechnung von Risspfaden mittels wegunabhängiger Erhaltungsintegrale*. Dissertation, Kassel University Press GmbH, Kassel, 2001.

[102] JUDT, P. O., AND RICOEUR, A. Accurate loading analyses of curved cracks under mixed-mode conditions applying the *J*-integral. *International Journal of Fracture 182*, 1 (2013), 53–66.

[103] JUDT, P. O., AND RICOEUR, A. Crack growth simulation of multiple cracks systems applying remote contour interaction integrals. *Theoretical and Applied Fracture Mechanics 75* (2015), 78–88.

[104] JUDT, P. O., AND RICOEUR, A. A new application of M- and L-integrals for the numerical loading analysis of two interacting cracks. *ZAMM - Journal of Applied Mathematics and Mechanics / Zeitschrift für Angewandte Mathematik und Mechanik 96*, 1 (2015), 24–36.

[105] JUDT, P. O., RICOEUR, A., AND LINEK, G. Crack path prediction in rolled aluminum plates with fracture toughness orthotropy and experimental validation. *Engineering Fracture Mechanics 138* (2015), 33–48.

[106] JUDT, P. O., ZARGES, J.-C., FELDMANN, M., RICOEUR, A., AND HEIM, H.-P. Deflecting mode-I cracks in anisotropic materials. *Mechanics of Materials 136* (2019), 103060.

[107] KALNING, M., KEK, S., KRANE, H. G., DORNA, V., PRESS, W., AND STEURER, W. Phason-strain analysis of the twinned approximant to the decagonal quasicrystal $Al_{70}Co_{15}Ni_{15}$: Evidence for a one-dimensional quasicrystal. *Physical review. B, Condensed matter 55*, 1 (1997), 187–192.

[108] KANG, S. S., DUBOIS, J. M., AND VON STEBUT, J. Tribological properties of quasicrystalline coatings. *Journal of Materials Research 8*, 10 (1993), 2471–2481.

[109] KELTON, K. F., HARTZELL, J. J., HENNIG, R. G., HUETT, V. T., AND TAKASAKI, A. Hydrogen storage in Ti–Zr and Ti–Hf-based quasicrystals. *Philosophical Magazine 86*, 6-8 (2006), 957–964.

[110] KENZARI, S., BONINA, D., DUBOIS, J. M., AND FOURNÉE, V. Quasicrystal–polymer composites for selective laser sintering technology. *Materials & Design 35* (2012), 691–695.

[111] KOLLECK, A., SCHNEIDER, G. A., AND MESCHKE, F. A. R-curve behavior of $BaTiO_3$ and PZT ceramics under the influence of an electric field applied parallel to the crack front. *Acta Materialia 48*, 16 (2000), 4099–4113.

[112] KOSCHELLA, U., GÄHLER, F., ROTH, J., AND TREBIN, H.-R. Phason elastic constants of a binary tiling quasicrystal. *Journal of Alloys and Compounds 342*, 1-2 (2002), 287–290.

[113] KOZINOV, S., KUNA, M., AND ROTH, S. A cohesive zone model for the electromechanical damage of piezoelectric/ferroelectric materials. *Smart Materials and Structures 23*, 5 (2014), 055024.

[114] KUNA, M. Fracture mechanics of piezoelectric materials – Where are we right now? *Engineering Fracture Mechanics 77*, 2 (2010), 309–326.

[115] KUNA, M. *Finite Elements in Fracture Mechanics*, vol. 201 of *Solid Mechanics and Its Applications*. Springer Netherlands, 2013.

[116] KUNA, M., AND RICOEUR, A. Theoretical investigation of fracture behaviour in ferroelectric ceramics. In *Fracture Mechanics of Ceramics*, R. C. Bradt, D. Munz, M. Sakai, V. Y. Shevchenko, and K. White, Eds., vol. 13. Springer US, Boston, 2002, pp. 63–82.

[117] LANDAU, L. D., AND LIFSHITZ, E. M. *Statistical Physics: Volume 5*, 3rd ed. Course of theoretical physics. Elsevier Science, Burlington, 1996.

[118] LANGE, S. *Untersuchung des konstitutiven Verhaltens ferroelektrischer, ferromagnetischer und multiferroischer Festkörper bei mehrachsiger multiphysikalischer Beanspruchung auf Basis kondensierter Modelle*. Dissertation, Kassel University Press GmbH, Kassel, 2001.

[119] LANGE, S., AND RICOEUR, A. High cycle fatigue damage and life time prediction for tetragonal ferroelectrics under electromechanical loading. *International Journal of Solids and Structures 80* (2016), 181–192.

[120] LEE, T., AND AKSAY, I. A. Hierarchical structure–ferroelectricity relationships of barium titanate particles. *Crystal Growth and Design 1*, 5 (2001), 401–419.

[121] LEI, J., YUN, L., AND BUI, T. Q. Numerical simulation of crack growth in piezoelectric structures by BEM. *Engineering Analysis with Boundary Elements 85* (2017), 30–42.

[122] LEKHNITSKII, S. G. *Theory of elasticity of an anisotropic body*. Mir Publisher, Moscow, 1981.

[123] LEVINE, D., LUBENSKY, T., OSTLUND, S., RAMASWAMY, S., STEINHARDT, P., AND TONER, J. Elasticity and dislocations in pentagonal and icosahedral quasicrystals. *Physical Review Letters 54*, 14 (1985), 1520–1523.

[124] LEVINE, D., AND STEINHARDT, P. J. Quasicrystals: A new class of ordered structures. *Physical Review Letters 53*, 26 (1984), 2477–2480.

[125] LI, X. F., FAN, T.-Y., AND SUN, Y. F. A decagonal quasicrystal with a Griffith crack. *Philosophical Magazine A 79*, 8 (1999), 1943–1952.

[126] LI, Y., ZHAO, M., QIN, Q.-H., AND FAN, C. Analysis solution method for 3D planar crack problems of two-dimensional hexagonal quasicrystals with thermal effects. *Applied Mathematical Modelling 69* (2019), 648–664.

[127] LIFSHITZ, R. The square fibonacci tiling. *Journal of Alloys and Compounds 342*, 1-2 (2002), 186–190.

[128] LINDER, C., AND MIEHE, C. Effect of electric displacement saturation on the hysteretic behavior of ferroelectric ceramics and the initiation and propagation of cracks in piezoelectric ceramics. *Journal of the Mechanics and Physics of Solids 60*, 5 (2012), 882–903.

[129] LIU, P., STIGENBERG, A. H., AND NILSSON, J.-O. Isothermally formed quasicrystalline precipitates used for strengthening in a new maraging stainless steel. *Scripta Metallurgica et Materialia 31*, 3 (1994), 249–254.

[130] LUBENSKY, T. C., RAMASWAMY, S., AND TONER, J. Hydrodynamics of icosahedral quasicrystals. *Physical Review B 32*, 11 (1985), 7444–7452.

[131] LYNCH, C. S., CHEN, L., SUO, Z., MCMEEKING, R. M., AND YANG, W. Crack growth in ferroelectric ceramics driven by cyclic polarization switching. *Journal of Intelligent Material Systems and Structures 6*, 2 (1995), 191–198.

[132] MA, H., AND CHEN, Y. H. The explicit formulations for the J_k vector in both isotropic and anisotropic cases. *International Journal of Fracture 75*, 2 (1996), R25–R28.

[133] MASCHKE, H.-G., AND KUNA, M. A review of boundary and finite element methods in fracture mechanics. *Theoretical and Applied Fracture Mechanics 4*, 3 (1985), 181–189.

[134] MEHTA, K., AND VIRKAR, A. V. Fracture mechanisms in ferroelectric-ferroelastic lead zirconate titanate (Zr: Ti=0.54:0.46) ceramics. *Journal of the American Ceramic Society 73*, 3 (1990), 567–574.

[135] MEISTERERNST, G., BAUER, B., AND GILLE, P. Czochralski growth of decagonal AlCoNi quasicrystals from Al-rich solution. *Acta Physica Polonica A 124*, 2 (2013), 344–349.

[136] MEYER, A., RABOLD, F., AND SCHERZER, M. Efficient finite element simulation of crack propagation using adaptive iterative solvers. *Communications in Numerical Methods in Engineering 22*, 2 (2005), 93–108.

[137] MIKULLA, R., STADLER, J., KRUL, F., TREBIN, H.-R., AND GUMBSCH, P. Crack propagation in quasicrystals. *Physical Review Letters 81*, 15 (1998), 3163–3166.

[138] MISHNAEVSKY, L. J., WEBER, U., AND SCHMAUDER, S. Numerical analysis of the effect of microstructures of particle-reinforced metallic materials on the crack growth and fracture resistance. *International Journal of Fracture 125*, 1 (2004), 33–50.

[139] MOËS, N., DOLBOW, J., AND BELYTSCHKO, T. A finite element method for crack growth without remeshing. *International Journal for Numerical Methods in Engineering 46*, 1 (1999), 131–150.

[140] MOHR, P. J., TAYLOR, B. N., AND NEWELL, D. B. CODATA recommended values of the fundamental physical constants: 2006. *Reviews of Modern Physics 80*, 2 (2008), 633–730.

[141] MOULSON, A. J., AND HERBERT, J. M. *Electroceramics*. John Wiley & Sons, Ltd, Chichester, UK, 2003.

[142] NAGAO, K., INUZUKA, T., NISHIMOTO, K., AND EDAGAWA, K. Experimental observation of quasicrystal growth. *Physical Review Letters 115*, 7 (2015).

[143] NGO, D., AND SCORDELIS, A. Finite element analysis of reinforced concrete beams. In *ACI Journal Proceedings* (1967), vol. 64, ACI.

[144] NISHIOKA, T., AND ATLURI, S. N. Numerical modeling of dynamic crack propagation in finite bodies, by moving singular elements—part 1: Formulation. *Journal of Applied Mechanics 47*, 3 (1980), 570–576.

[145] OATES, W. S., LYNCH, C. S., LUPASCU, D. C., NJIWA, A. B. K., AULBACH, E., AND RÖDEL, J. Subcritical crack growth in lead zirconate titanate. *Journal of the American Ceramic Society 87*, 7 (2004), 1362–1364.

[146] PAK, Y. E. Crack extension force in a piezoelectric material. *Journal of Applied Mechanics 57*, 3 (1990), 647–653.

[147] PAK, Y. E. Linear electro-elastic fracture mechanics of piezoelectric materials. *International Journal of Fracture 54*, 1 (1992), 79–100.

[148] PAK, Y. E., AND HERRMANN, G. Conservation laws and the material momentum tensor for the elastic dielectric. *International Journal of Engineering Science 24*, 8 (1986), 1365–1374.

[149] PAN, E. Some new three-dimensional Green's functions in anisotropic piezoelectric bimaterials. *Electronic Journal of Boundary Elements 1*, 2 (2003), 236–269.

[150] PANASYUK, V. V. Limiting equilibrium of brittle solids with fractures.

[151] PARK, K., AND PAULINO, G. H. Cohesive zone models: A critical review of traction-separation relationships across fracture surfaces. *Applied Mechanics Reviews 64*, 6 (2011).

[152] PARK, S. B., AND SUN, C. T. Effect of electric field on fracture of piezoelectric ceramics. *International Journal of Fracture 70*, 3 (1993), 203–216.

[153] PARK, S. B., AND SUN, C. T. Fracture criteria for piezoelectric ceramics. *Journal of the American Ceramic Society 78*, 6 (1995), 1475–1480.

[154] PARTON, V. Z. Fracture mechanics of piezoelectric materials. *Acta Astronautica 3*, 9-10 (1976), 671–683.

[155] PENROSE, R. The role of aesthetics in pure and applied mathematical research. *Bulletin of the Institute of Mathematics and Its Applications 10* (1974), 266–271.

[156] QIAN, J., AND FATEMI, A. Mixed mode fatigue crack growth: A literature survey. *Engineering Fracture Mechanics 55*, 6 (1996), 969–990.

[157] RICE, J. R. Mathematical analysis in the mechanics of fracture. *Fracture: an advanced treatise 2* (1968), 191–311.

[158] RICE, J. R. A path independent integral and the approximate analysis of strain concentration by notches and cracks. *Journal of Applied Mechanics 35* (1968), 379–386.

[159] RICE, J. R. The localization of plastic deformation. In *Theoretical and Applied Mechanics* (1976), W. Koiter, Ed., North-Holland Publishing Co, pp. 207–220.

[160] RICHARD, H. A. Bruchvorhersagen bei überlagerter normal- und schubbeanspruchung von rissen. In *VDI-Forschungsheft*, vol. 631. VDI-Verl., Düsseldorf, 1985.

[161] RICHARD, H. A., FULLAND, M., AND SANDER, M. Theoretical crack path prediction. *Fatigue & Fracture of Engineering Materials & Structures 28*, 1-2 (2005), 3–12.

[162] RICOEUR, A. Theoretische untersuchungen zum bruchverhalten ferroelektrischer keramiken bei elektromechanischer beanspruchung. In *Freiberger Forschungshefte Reihe B, Werkstoffwissenschaft*, vol. 340. TU Bergakademie, Freiberg, 2007.

[163] RICOEUR, A., GELLMANN, R., AND WANG, Z. Influence of inclined electric fields on the effective fracture toughness of piezoelectric ceramics. *Acta Mechanica 226*, 2 (2015), 491–503.

[164] RICOEUR, A., AND KUNA, M. Influence of electric fields on the fracture of ferroelectric ceramics. *Journal of the European Ceramic Society 23*, 8 (2003), 1313–1328.

[165] RICOEUR, A., AND KUNA, M. A micromechanical model for the fracture process zone in ferroelectrics. *Computational Materials Science 27*, 3 (2003), 235–249.

[166] RICOEUR, A., AND KUNA, M. Electrostatic tractions at dielectric interfaces and their implication for crack boundary conditions. *Mechanics Research Communications 36*, 3 (2009), 330–335.

[167] SADD, M. *Elasticity: Theory, Applications, and Numerics*, 2nd ed. Elsevier, 2009.

[168] SCHEEL, J. *Theoretische Untersuchung zum Einfluss von Phason-Feldern auf Risspfade in quasikristallinen Körpern*. Bachelor's thesis, University of Kassel, 2015.

[169] SCHNEIDER, G. A. Influence of electric field and mechanical stresses on the fracture of ferroelectrics. *Annual Review of Materials Research 37*, 1 (2007), 491–538.

[170] SCHNEIDER, G. A., FELTEN, F., AND MCMEEKING, R. M. The electrical potential difference across cracks in PZT measured by Kelvin Probe Microscopy and the implications for fracture. *Acta Materialia 51*, 8 (2003), 2235–2241.

[171] SCHNEIDER, G. A., AND HEYER, V. Influence of the electric field on Vickers indentation crack growth in $BaTiO_3$. *Journal of the European Ceramic Society 19*, 6-7 (1999), 1299–1306.

[172] SCHÖLLMANN, M., FULLAND, M., AND RICHARD, H. Development of a new software for adaptive crack growth simulations in 3d structures. *Engineering Fracture Mechanics 70*, 2 (2003), 249–268.

[173] SCHREUER, J., STEURER, W., LOGRASSO, T. A., AND WU, D. Elastic properties of icosahedral i-$Cd_{84}Yb_{16}$ and hexagonal h-$Cd_{51}Yb_{14}$. *Philosophical Magazine Letters 84*, 10 (2004), 643–653.

[174] SCHWABL, F. *Advanced quantum mechanics*. Springer, Berlin, 2008.

[175] SEO, Y.-H., VÖGLER, M., ISAIA, D., AULBACH, E., RÖDEL, J., AND WEBBER, K. G. Temperature-dependent R-curve behavior of $Pb(Zr_{(1-x)}Ti_x)O_3$. *Acta Materialia 61*, 17 (2013), 6418–6427.

[176] SHECHTMAN, D., BLECH, I., GRATIAS, D., AND CAHN, J. W. Metallic phase with long-range orientational order and no translational symmetry. *Physical Review Letters 53*, 20 (1984), 1951–1953.

[177] SHI, W. Collinear periodic cracks and/or rigid line inclusions of antiplane sliding mode in one-dimensional hexagonal quasicrystal. *Applied Mathematics and Computation 215*, 3 (2009), 1062–1067.

[178] SLADEK, J., SLADEK, V., AND ATLURI, S. N. Path-independent integral in fracture mechanics of quasicrystals. *Engineering Fracture Mechanics 140* (2015), 61–71.

[179] SLADEK, J., SLADEK, V., KRAHULEC, S., ZHANG, C., AND WÜNSCHE, M. Crack analysis in decagonal quasicrystals by the MLPG. *International Journal of Fracture 181* (2013), 115–126.

[180] SLADEK, J., SLADEK, V., REPKA, M., AND SCHMAUDER, S. Gradient theory for crack problems in quasicrystals. *European Journal of Mechanics-A/Solids 77* (2019), 103813.

[181] SLADEK, J., SLADEK, V., STANAK, P., ZHANG, C., AND TAN, C.-L. Fracture mechanics analysis of size-dependent piezoelectric solids. *International Journal of Solids and Structures 113-114* (2017), 1–9.

[182] SOCOLAR, J., LUBENSKY, T., AND STEINHARDT, P. Phonons, phasons, and dislocations in quasicrystals. *Physical Review B 34*, 5 (1986), 3345–3360.

[183] SOSA, H. Plane problems in piezoelectric media with defects. *International Journal of Solids and Structures 28*, 4 (1991), 491–505.

[184] SOSA, H. A., AND PAK, Y. Three-dimensional eigenfunction analysis of a crack in a piezoelectric material. *International Journal of Solids and Structures 26*, 1 (1990), 1–15.

[185] STEURER, W. The structure of quasicrystals. *Zeitschrift für Kristallographie - Crystalline Materials 190*, 1-4 (1990).

[186] STEURER, W. Quasicrystals: What do we know? What do we want to know? What can we know? *Acta Crystallographica A 74*, 1 (2018), 1–11.

[187] STEURER, W., AND DELOUDI, S. *Crystallography of Quasicrystals: Concepts, Methods and Structures*, vol. 126 of *Springer series in materials science*. Springer-Verlag Berlin Heidelberg, Berlin, Heidelberg, 2009.

[188] STROH, A. N. Dislocations and cracks in anisotropic elasticity. *Philosophical Magazine 3*, 30 (1958), 625–646.

[189] STROH, A. N. Steady state problems in anisotropic elasticity. *Journal of Mathematical Physics 41*, 1-4 (1962), 77–103.

[190] SUCK, J.-B., SCHREIBER, M., AND HÄUSSLER, P. *Quasicrystals: An Introduction to Structure, Physical Properties and Applications*, vol. 55 of *Springer series in materials science*. Springer, Berlin, Heidelberg, 2002.

[191] SUN, C. T., AND PARK, S. B. Measuring fracture toughness of piezoceramics by Vickers indentation under the influence of electric fields. *Ferroelectrics 248* (2000), 79–95.

[192] SUO, Z., KUO, C.-M., BARNETT, D. M., AND WILLIS, J. R. Fracture mechanics for piezoelectric ceramics. *Journal of the Mechanics and Physics of Solids 40*, 4 (1992), 739–765.

[193] TADA, H., PARIS, P. C., AND IRWIN, G. R. *The Stress Analysis of Cracks Handbook, Third Edition*. ASME Press, 2000.

[194] TADMOR, E. B., AND MILLER, R. E. *Modeling materials: Continuum, atomistic and multiscale techniques*. Cambridge Univ. Press, Cambridge, 2014.

[195] TING, T. C. T. *Anisotropic elasticity theory and applications*, 1 ed., vol. 45 of *The Oxford engineering science series*. Oxford Univ. Press, 1996.

[196] TOBIN, A. G., AND PAK, E. Effect of electric fields on fracture behavior of PZT ceramics. In *Smart Structures and Materials 1993: Smart Materials* (1993), V. K. Varadan, Ed., SPIE Proceedings, SPIE, pp. 78–86.

[197] TSAI, A.-P. "back to the future"–an account discovery of stable quasicrystals. *Accounts of chemical research 36*, 1 (2003), 31–38.

[198] TSAI, A.-P., MASUMOTO, T., AND YAMAMOTO, A. Stable one-dimensional quasicrystals in Al-Pd-Fe alloys. *Philosophical Magazine Letters 66*, 4 (1992), 203–208.

[199] TUPHOLME, G. E. A non-uniformly loaded anti-plane crack embedded in a half-space of a one-dimensional piezoelectric quasicrystal. *Meccanica 53*, 4-5 (2018), 973–983.

[200] VAN SMAALEN, S. Incommensurate crystal structures. *Crystallography Reviews 4*, 2 (1995), 79–202.

[201] WAGNER, M. *Lineare und nichtlineare FEM*. Springer Fachmedien Wiesbaden, 2019.

[202] WANG, H., AND SINGH, R. N. Crack propagation in piezoelectric ceramics: Effects of applied electric fields. *Journal of Applied Physics 81*, 11 (1997), 7471–7479.

[203] WANG, X., AND SCHIAVONE, P. Dislocations, imperfect interfaces and interface cracks in anisotropic elasticity for quasicrystals. *Mathematics and Mechanics of Complex Systems 1*, 1 (2013), 1–17.

[204] WANG, Z., AND RICOEUR, A. Numerical crack path prediction under mixed-mode loading in 1D quasicrystals. *Theoretical and Applied Fracture Mechanics 90* (2017), 122–132.

[205] WANG, Z., AND RICOEUR, A. The influence of electric loading on crack paths in ferroelectrics. *Journal of the Mechanics and Physics of Solids 142* (2020), 104043.

[206] WANG, Z., SCHEEL, J., AND RICOEUR, A. Mixed-mode crack tip loading and crack deflection in 1D quasicrystals. *Applied Physics A 122* (2016), 1041.

[207] WATSON, T. J., GORDILLO, M. A., CERNATESCU, I., AND AINDOW, M. Structure and mechanical properties in a powder-processed icosahedral-phase-strengthened aluminum alloy. *Scripta Materialia 123* (2016), 51–54.

[208] WEBBER, K. G., VÖGLER, M., KHANSUR, N. H., KAESWURM, B., DANIELS, J. E., AND SCHADER, F. H. Review of the mechanical and fracture behavior of Perovskite lead-free ferroelectrics for actuator applications. *Smart Materials and Structures 26*, 6 (2017), 063001.

[209] WELLS, A. A. Unstable crack propagation in metals: cleavage and fast fracture. In *Proceedings of the crack propagation symposium, vol. 1* (1961), Cranfield, UK, p. 84.

[210] WESTRAM, I., RICOEUR, A., EMRICH, A., RÖDEL, J., AND KUNA, M. Fatigue crack growth law for ferroelectrics under cyclic electrical and combined electromechanical loading. *Journal of the European Ceramic Society 27*, 6 (2007), 2485–2494.

[211] WINGEN, M., AND RICOEUR, A. Caloric aspects of nonlinear ferroelectric constitutive behavior: modeling and simulation. *Continuum Mechanics and Thermodynamics 31*, 2 (2018), 549–568.

[212] YANG, J., AND LI, X. Analytic solutions of problem about a circular hole with a straight crack in one-dimensional hexagonal quasicrystals with piezoelectric effects. *Theoretical and Applied Fracture Mechanics* (2015).

[213] YANG, L.-Z., RICOEUR, A., HE, F.-M., AND GAO, Y. Finite size specimens with cracks of icosahedral Al–Pd–Mn quasicrystals. *Chinese Physics B 23*, 5 (2014), 056102.

[214] YANG, W. Some new stable one-dimensional quasicrystals in an $Al_{65}Cu_{20}Fe_{10}Mn_5$ alloy. *Philosophical Magazine Letters 74*, 5 (1996), 357–366.

[215] ZHANG, L., ZHANG, Y., AND GAO, Y. General solutions of plane elasticity of one-dimensional orthorhombic quasicrystals with piezoelectric effect. *Physics Letters A 378*, 37 (2014), 2768–2776.

[216] ZHANG, T. Y., AND GAO, C. F. Fracture behaviors of piezoelectric materials. *Theoretical and Applied Fracture Mechanics 41*, 1-3 (2004), 339–379.

[217] ZHU, A.-Y., AND FAN, T.-Y. Dynamic crack propagation in decagonal Al–Ni–Co quasicrystal. *Journal of Physics: Condensed Matter 20*, 29 (2008), 295217.

[218] ZHU, A.-Y., AND FAN, T.-Y. Elastic analysis of a Griffith crack in icosahedral quasicrystal Al-Pd-Mn quasicrystal. *International Journal of Modern Physics B 23*, 16 (2009), 3429–3444.

[219] ZOLLNER, E. M., SCHENK, S., SETVIN, M., AND FÖRSTER, S. Perfect monolayers of the $BaTiO_3$ – derived 2D oxide quasicrystals investigated by scanning tunneling microscopy and noncontact atomic force microscopy. *physica status solidi (b) 502* (2019), 1900620.

ISBN 978-3-7376-0989-0